

Photoionized Herbig-Haro objects in the Orion Nebula through deep high-spectral resolution spectroscopy I: HH529 II-III

J. E. Méndez-Delgado^{1,2} , C. Esteban^{1,2}, J. García-Rojas^{1,2}, W. J. Henney³
A. Mesa-Delgado⁴ and K. Z. Arellano-Córdova¹

¹ Instituto de Astrofísica de Canarias (IAC), E-38205 La Laguna, Spain

² Departamento de Astrofísica, Universidad de La Laguna, E-38206 La Laguna, Spain

³ Instituto de Radioastronomía y Astrofísica, Universidad Nacional Autónoma de México, Apartado Postal 3-72, 58090 Morelia, Michoacán, México

⁴ Domicilio Particular, Tenerife, Spain

Accepted XXX. Received YYY; in original form ZZZ

ABSTRACT

This is the abstract.

Key words: ISM:Abundances – ISM: Herbig–Haro objects – ISM: individual: Orion Nebula – ISM: individual: HH 529III.

1 INTRODUCTION

Herbig-Haro (HH) objects are small emission nebulae associated with outflows from young stars interacting with the surrounding environment (Schwartz 1983). Since their discovery by George Herbig and Guillermo Haro (Herbig 1950, 1951, 1952; Haro 1952, 1953) a multitude of them have been discovered and studied. Through the *Hubble Space Telescope* (*HST*), multiple velocity features associated to HHs have been observed in the Orion Nebula with unprecedented detail. There are several works dedicated to determine the nature and physical properties of many outflows from stars in the Orion Nebula (see Bally et al. 2000; Bally & Reipurth 2001; O’Dell & Henney 2008; O’Dell et al. 2015, and references therein). These have revealed that the Orion Nebula is a complex environment with multiple gas interactions. These high velocity systems cover a wide range of velocities with noticeable differences in the conditions of their emitting gas.

Through the radiation field of the massive stars of the Orion Nebula, HHs can be photoionized, and therefore we can determine their physical conditions and chemical abundances using the standard methods developed to study ionized nebulae (Reipurth & Bally 2001). However, there are few works in the literature dedicated to analyze the chemical composition of photoionized HHs isolating their emission from that of the nebula in which they are immersed. Using high-spectral resolution spectroscopy, Blagrave et al. (2006) and Mesa-Delgado et al. (2009) were able to separate the emission of HH529III+II and HH202S, respectively, from the main emission of the Orion Nebula. This permitted to analyze the chemical composition of the ionized gas under the peculiar physical conditions of the HHs and the effects of their interaction with the surrounding nebular gas as, for example, the chemical effects of dust destruction.

As Mesa-Delgado et al. (2008) showed through long slit spec-

tra, there are important spatial variations in the physical conditions of the Orion Nebula due to the presence of HHs. These variations also affect some chemical properties of the gas. For example, Mesa-Delgado et al. (2008) found an increase in the discrepancy between the abundances obtained from Recombination Lines (RLs) and Collisionally Excited Lines (CELs) for the same heavy element at the locations of HHs. Therefore, it is important to investigate the physical and chemical influence that HH objects exert on the gas of ionized nebula and test our knowledge of photoionized regions analyzing objects with complex conditions.

This work aims to be the first in a series devoted to the analysis of photoionized HHs in the Orion Nebula using very high resolution spectroscopy from the Ultraviolet Visual Echelle Spectrograph (UVES) (D’Odorico et al. 2000) in the UT2 (Kueyen) of the Very Large Telescope (VLT). This paper is dedicated to HH529 in two associated bow shocks: HH529II and HH529III. HH529 consists of a series of shocks flowing toward the east in the central region of the Orion Nebula. It is break down into three main shocks designed as HH529I, HH529II and HH529III, numbered from west to east (O’Dell & Henney 2008). We spatially separate the emission from HH529II and HH529III and isolate the blueshifted high-velocity emission of the gas of shock from the nebular one. We analyze our high-spectral resolution observations that cover a wide spectral range (3100–10400Å) through 4 spatial cuts, obtaining 7 1D spectra: 4 corresponding to the main emission of the Orion Nebula, one for HH529II, another one for HH529III and one additional 1D spectrum corresponding to the sum of all the rest of 1D spectra. This last spectrum simulates a single low-spectral resolution longslit observation, including the mixing of the HH emission with that of the nebular gas, summing up the emission of all the velocity components for each emission line. In this paper we analyze the physical conditions, chemical composition and kinematic properties of HH529II, HH529III and some particular zones of the Orion Nebula.

* E-mail: jemd@iac.es

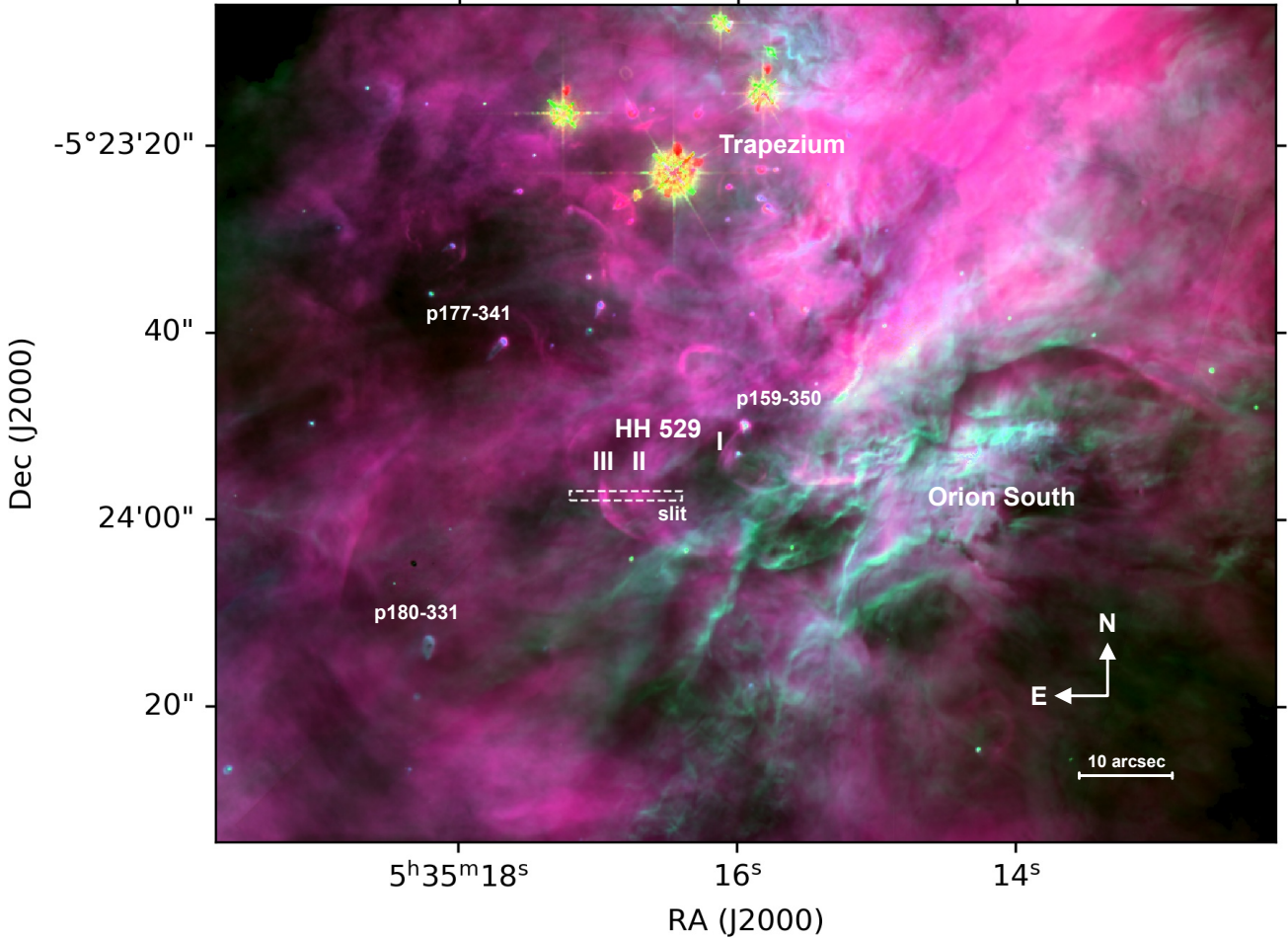


Figure 1. Composite WFPC2 *HST* image of the central Orion Nebula. Three narrow filters were used for the color scale: F502N, F658N and F656N for red, green and blue, respectively (images obtained by [Bally et al. 1998](#)). The slit position of our observations is indicated. It covers the bow shocks HH529III and HH529II of the Herbig-Haro object HH529.

The paper is divided as follows: in Section 2 we describe the observations and the reduction process for the spectroscopic data, as well as the *HST* imaging used to calculate the proper motions of HH529 in the plane of the sky. In Section 3 we describe the emission line measurements, identifications and the reddening correction as well a comparison between our observations and those from [Blagrave et al. \(2006\)](#) in the common spectral range (3500–7500Å). In Section 4 we derive the physical conditions of the gas throughout different methods, using CELs, RLs and continuum emission. In Section 5 we derive ionic abundances using both RLs and CELs. In Section 6 we describe the temperature fluctuations paradigm and estimate values of t^2 , based on the different temperature diagnostics. In Section 7 we discuss the Abundance Discrepancy (AD) between ionic abundances derived with CELs and RLs. In Section 8 we analyze the total abundances obtained from RLs and CELs, these last case with and without the assumption of the existence of temperature fluctuations ($t^2 > 0$ and $t^2 = 0$, respectively). We also discuss the increase in the gaseous Fe abundance due to dust destruction in HH529II and HH529III. In Section 9 we describe the

radial velocity structure of each component, both the nebular and the high-velocity ones. We also derive the electron temperature from the thermal broadening of the line profiles. In Section 10 we calculate the proper motions of HH529 and discuss some physical properties of the shock, as the pre-shock density. Finally, in Section 11 we summarize our main conclusions. In the appendix, some tables and figures are attached as supporting material.

2 OBSERVATIONS AND DATA REDUCTION

The observations were made under photometric conditions during the November 28 and 29, 2013 nights using UVES in the UT2 of the Very large Telescope (VLT) in Cerro Paranal, Chile. The slit position was centred at the coordinates RA(J2000)= $05^h35^m16^s.80$, DEC(J2000)= $-05^\circ23'57.48''$, having a length of 10 arcsec in the blue arm and 12 arcsec in the red arm looking for an adequate interorder separation. Table 1 shows the main parameters of UVES observations. The slit width was set to 1 arcsec, which provides an effective spectral resolution $\lambda/\Delta\lambda \approx 40000$ (6.5 km s^{-1}). To

Table 1. Main parameters of UVES spectroscopical observations.

Date	$\Delta\lambda$ (Å)	Exp. time (s)	Seeing (arcsec)	Airmass
2013-11-29	3100-3885	5, 3×180	0.79	1.20
2013-11-29	3750-4995	5, 3×600	0.65	1.14
2013-11-29	4785-6805	5, 3×180	0.79	1.20
2013-11-29	6700-10420	5, 3×600	0.65	1.14

Table 2. HST observations used in proper motion study.

Date	Program	Camera, CCD, Filter	Reference
1995-03	5469	WFPC2, PC, F656N	Bally et al. (1998)
2005-04	10246	ACS, WFC, F658N	Roberto et al. (2013)
2015-01	13419	WFC3, UVIS, F656N	Bally & Reipurth (2018)

perform the flux calibration of the data, three exposures of 150s of the standard star GD71 (Moehler et al. 2014a,b) were taken under similar conditions of seeing and airmass than the science observations during the same night. The spatial coverage of the slit is shown in Fig. 1.

Our observations cover the spectral range between 3100–10420 Å, using two standard dichroic settings of UVES. Dichroic#1 setting split the light in two wavelengths ranges: from 3100 to 3885 Å in the blue arm and from 4785 to 6805 Å in the red one, while the dichroic#2 setting covers from 3750 to 4995 Å in the blue arm and from 6700 to 10420 Å in the red one. However, in our high resolution and wide spectral range observations, there are some observational gaps. The red arm use two CCDs, and due to their physical separation, spectral ranges 5773–5833 Å and 8540–8650 Å could not be observed. Additionally there are some narrow gaps that could not be observed in the redmost part of the red arm in the dichroic#2 setting because the spectral orders could not fit entirely within the CCD. These range are ∼8911–8913 Å, 9042–9046 Å, 9178–9182 Å, 9317–9323 Å, 9460–9469 Å, 9608–9619 Å, 9760–9774 Å, 9918–9935 Å, 10080–10100 Å and 10248–10271 Å.

We reduced the spectra using a combination of tasks from the public ESO UVES pipeline (Ballester et al. 2000) under the GASGANO graphic user interface, and tasks built by ourselves based on IRAF¹ (Tody 1993) and several python packages. Firstly, we used IRAF tasks FIXPIX and IMCOMBINE to mask known bad pixels in our images and to combine all the images with the same exposure time. Then, we used the ESO UVES pipeline for bias subtraction, background subtraction, aperture extraction, flat-fielding and wavelength calibration. As a product, we obtained a 2D spectrum of science for each arm in each dichroic setting without flux calibration. We followed the same procedure for GD 71 but extracting both a 2D and a 1D spectrum. The 2D spectrum of the calibration star helps us to note the presence of faint sky lines which are also present in the science spectra.

One crucial step of the data reduction is to perform adequate cuts in the spatial direction of the slit to extract 1D spectra. We chose these spatial cuts in order to study in detail each observed velocity component and trying to maximise the shock/nebular emission ratio. We relied on the [Fe III] λ4658 line, which is relatively bright in the high-velocity components to delimit the cuts. The seeing conditions permit us to separate HH529II from HH529III (see Fig. 2). HH529II

has a “ball shape” while HH529III presents an elongated distribution along the spectral axis. This is related with the morphology of the outflow system of HH529 (firstly identified by Bally et al. 2000). This system shows three notorious bright arcs, identified by the numbers I, II and III, being numbered by their position from west to east (O’Dell & Henney 2008). However, the system is more complex than just three homogeneous arcs as we will analyze in Section 10. The length covered by each cut in the spatial direction is 1.23 arcsec, 4.43 arcsec, 2.46 arcsec and 1.23 arcsec for cuts 1, 2, 3 and 4, respectively. This numbering has been defined from west to east in the spatial direction (see Fig. 1). Cut 1 is at the bottom and cut 4 at the top of Fig. 2. In the context of the nomenclature given by O’Dell & Henney (2008), the high-velocity component of cut 3 corresponds to HH529III, while that of cut 2 is HH529II. We have also defined an additional 1D spectrum, labelled as “combined cuts”. This was created by adding the flux of the lines measured in all the components of all cuts. The lines included in this spectrum were those detected and identified in the nebular component of all cuts. The spectrum of the combined cuts is useful to analyze the effect that a non-resolved shock component would have in the properties of a low-resolution spectrum. We used the Python-based Astropy package (Astropy Collaboration et al. 2013; Price-Whelan et al. 2018) to obtain 1D spectra for each cut, doing the conversion between the different pixel scale of the CCDs in the blue and the red arm. Each spatial cut covers an area larger than the seeing size during the observations, as it is shown in Table 1. We used the IRAF tasks STANDARD, SENSFUNC and CALIBRATE to perform the flux calibration of each 1D spectra of all cuts. The radial velocity correction was made using Astropy.

For the determination of the proper motion of HH529, we take advantage of the 20 years of archival HST imaging that is now available. We employ three epochs of observations, as detailed in Table 2. All data was downloaded from the Barbara A. Mikulski Archive for Space Telescopes².

3 LINE INTENSITIES AND REDDENING

We used the SPLOT task from IRAF to measure line intensities and estimate their uncertainties. We applied a double Gaussian profile fit for the nebular and the high-velocity component, delimiting the continuum by eye. For each measured line, we estimate the value of the continuum and its *rms* on each side to propagate uncertainties associated to the flux measurement. In case of evident line blending, we applied as many Gaussians as necessary to properly reproduce the line profile. As it was mentioned in Section 2, the observed wavelength range (3100–10420 Å) was covered in 4 sections (two dichroic settings splitting the light into two spectrograph arms). Between each section, there is an overlapping zone from where we used the most intense lines to normalize the entire spectrum with respect to H β . The measured flux of H I λ3835, [O III] λ4959 and [S II] λ6731 lines were used to normalize the spectra from the blue arm of dichroic#1, the red arm of dichroic#1 and the red arm of dichroic#2 settings respectively (H β is in the blue arm of dichroic#2 setting). This normalization eliminates the differences in flux between each part of the spectrum due to the different pixel scale between the blue and the red arms.

The emission lines were corrected for reddening using Eq. (1), where $f(\lambda)$ is the adopted extinction curve from Blagrave et al.

¹ IRAF is distributed by National Optical Astronomy Observatory, which is operated by Association of Universities for Research in Astronomy, under cooperative agreement with the National Science Foundation

² MAST, <https://archive.stsci.edu/>

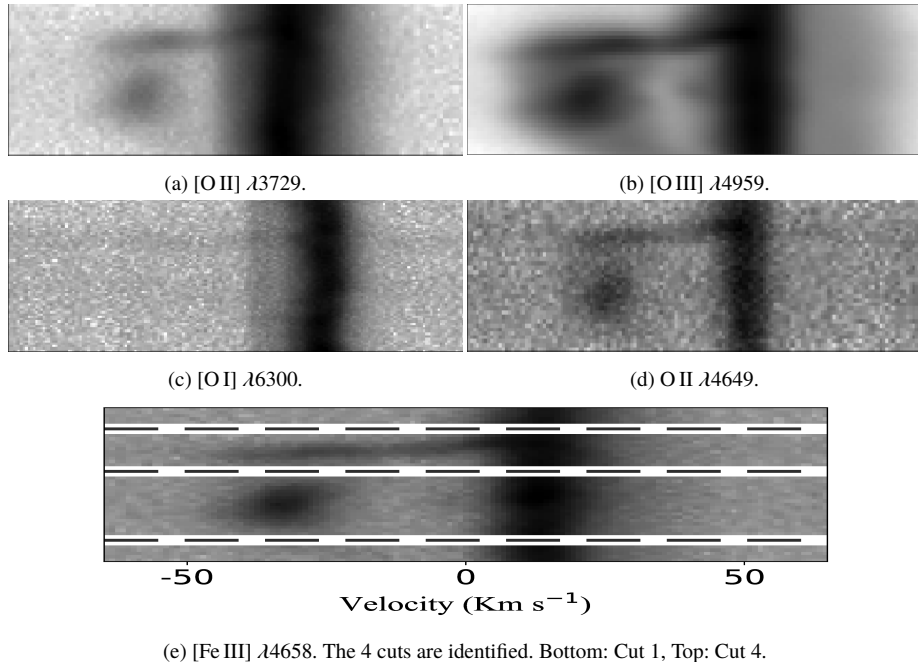


Figure 2. *Upper panels:* Sample of representative lines in the bi-dimensional spectrum. The Y axis corresponds to the spatial direction (up east, down west, see Fig. 1 for the spatial location of the slit) while the X axis is the spectral axis. All figures are centered at λ_0 , the rest-frame reference wavelength of each line. The ‘‘ball-shaped’’ emission corresponds to HH529II while the elongated one to HH529III. The blueshifted high-velocity components do not present emission from neutral elements as [O I] and rather faint emission from low ionization ions such as [O II]. *Bottom panel:* Emission of the [Fe III] $\lambda 4658.17$ line as well as the limits and extension of the different spatial cuts selected to analyze each velocity component. Cut 1 is at the bottom, which corresponds to the westernmost one. The spatial coverage is 1.23 arcsec, 4.43 arcsec, 2.46 arcsec and 1.23 arcsec for cuts 1, 2, 3 and 4, respectively.

Table 3. Reddening coefficients for each component.

	$c(H\beta)$	
	High-velocity	Nebula
Cut 1	-	0.82 ± 0.02
Cut 2	0.90 ± 0.03	0.83 ± 0.02
Cut 3	0.89 ± 0.05	0.84 ± 0.03
Cut 4	-	0.83 ± 0.02
Combined cuts	-	0.85 ± 0.02

(2007), normalized to $H\beta$. We calculate the reddening coefficient, $c(H\beta)$, by using the ratios of $H\varepsilon$, $H\delta$, $H\gamma$ and $H\alpha$ Balmer lines and the P12, P11, P10, P9 Paschen lines with respect to $H\beta$ and the emissivity coefficients of [Storey & Hummer \(1995\)](#).

$$\frac{I(\lambda)}{I(H\beta)} = \frac{F(\lambda)}{F(H\beta)} \times 10^{c(H\beta)f(\lambda)}. \quad (1)$$

The final adopted $c(H\beta)$ value is the weighted average value obtained from the aforementioned Balmer and Paschen lines and is shown in Table 3 for each component. The selected H I lines are free of line-blending or telluric absorptions that may affect the determination of $c(H\beta)$. Despite there are more isolated and bright Balmer and Paschen lines available in the spectra, we did not use them since their emission depart from the case B values. This behaviour was reported previously in the Orion Nebula ([Mesa-Delgado et al. 2009](#)), the Magellanic Clouds ([Domínguez-Guzmán et al. 2019](#)) and in several planetary nebulae (PNe [Rodríguez 2020](#)).

[Blagrove et al. \(2006\)](#) (hereinafter BMB06) observed a zone of the Orion Nebula that includes HH529II+III using the 4m Blanco telescope at the Cerro Tololo Inter-American Observatory, covering the 3500-7500Å spectral region. A comparison between

their reddening corrected nebular spectrum and ours (from cut 2) is shown in Fig. 3. For the comparison, we have excluded lines flagged with notes of ‘‘Avg’’, ‘‘blend’’ or ‘‘small FWHM’’ in Table 1 of BMB06, due to their uncertain fluxes. For example, [Ne III] $\lambda 3967.46$ line, marked with an ‘‘Avg’’, is inconsistent with the measured intensity of [Ne III] $\lambda 3868.75$, since their observed ratio is 2.02, quite far from the theoretical one of 3.29. A least squares linear fit of the data represented in Fig. 3 yields the relationship $y = 1.00 (\pm 0.01) x + 0.05 (\pm 0.02)$, indicating that the BMB06’s spectrum (y values) presents systematically larger intensity line ratios (relative to $H\beta$) than ours (x values). This is very noticeable in the spectral region of the high-level Balmer lines (3660-3720Å), where this difference can reach up to 50%. This may be due to the relative weakness of these lines, coupled with the abrupt change in the continuum due to the closeness to the Balmer discontinuity. For other lines, the slight discrepant tendency disappears considering an increase of about 10% in the intensity of $I(H\beta)$. This possible underestimation of $I(H\beta)$ in the spectrum of the nebular component of BMB06 is the most likely explanation considering that the intensity ratios between other bright H I lines are consistent with the theoretical ones and not those with respect to $H\beta$. We did not compare their high-velocity component with ours because their slit position is slightly different than ours, and their seeing of 2-2.5 arcsec does not permit to adequately separate spatially HH529II from HH529III.

Fig. 4 shows the $H\beta$ line profile in the different cuts. As it can be seen, the reddest component of each profile (corresponding to the nebular component) shows practically the same shape in all cuts except in cut 3, where the line is broadened by the presence of a larger velocity dispersion in the high-velocity component. The

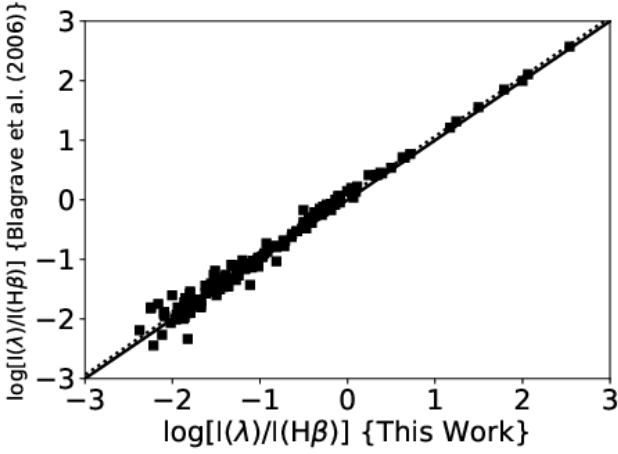


Figure 3. Comparison between the reddening corrected nebular spectra (from cut 2) and the one from Blagrade et al. (2006) observations. The dotted line represents the linear fit $y = 1.00x + 0.05$, while the solid line represents $y = x$.

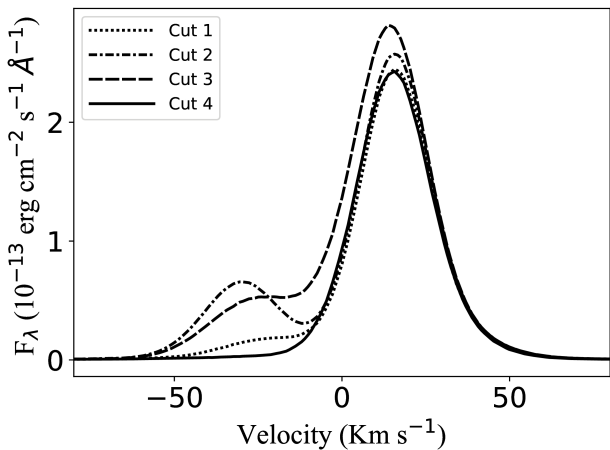


Figure 4. Profile of $H\beta$ line in each of the analyzed spatial cuts.

complexity of the velocity components of HH529 is discussed in more detail in section 10.

Line identifications were consistently made by adopting the theoretical wavelengths of Peter Van Hoof's latest Atomic Line List v2.05b21³ (Van Hoof 2018) for all ions except for Cl III, Cl IV and Ne III due to some inconsistencies found (see Section 9 for a detailed discussion). Our spectra are very extensive and are attached in the online annexes to this article. In the nebular components, 514, 633, 579 and 522 lines were measured in cuts 1, 2, 3 and 4, respectively. For HH529II and HH529III, 376 and 245 lines were detected, respectively. Multi-line blends were counted as single detections.

4 PHYSICAL CONDITIONS

4.1 Physical conditions based on CELs

We use PyNeb (version 1.1.10) (Luridiana et al. 2015) and the updated atomic dataset listed in Table 4 to calculate physical conditions based on the intensity ratios of CELs from different ions.

The first step was to test all the intensity ratios of CELs that can serve as a temperature or density diagnostic using the PyNeb's task *getCrossTemDen*. This task uses two line ratios at the same time: one as density diagnostic and the other one for temperature, giving their convergence to a pair n_e, T_e as a result. We tried all possible permutations for all the available diagnostics in all components from all cuts. We only discarded the use of lines strongly affected by blends, telluric emissions and/or absorptions or reflections in the optical system of the spectrograph. We did not consider the n_e diagnostic based on $[N\text{ I}] \lambda\lambda 5198/5200$ owing to its unphysical meaning in the Orion Nebula (Ferland et al. 2012).

Diagnostics based on $[Ni\text{ III}] \lambda_1/\lambda_2$, where $\lambda_1, \lambda_2 \in [6000, 6534, 6682, 6797, 6946, 7890]$ do not give any useful physical information since they either did not converge or showed convergences at values highly discordant with the other diagnostics. This will be commented in more detail in Section 5.1.2. Another interesting case are the diagnostics based on $[Fe\text{ III}] \lambda_1/\lambda_2$, where $\lambda_1, \lambda_2 \in [4658, 4702, 4734, 4881, 5011, 4925, 4987, 5271]$. With the exception of $[Fe\text{ III}] 4658/4702$, all the diagnostics converge in a fairly wide range of physical conditions. This is due to the ambivalence and/or high dependence of these ratios on both density and temperature. This will be discussed in Section 4.2.

After the initial exploration, we define the ratios we consider good indicators of electron density and temperature. Then we use Monte Carlo simulations with 1000 points to estimate uncertainties in the physical conditions given by the *getCrossTemDen* task of PyNeb. For example, using $[O\text{ III}] \lambda 4363/\lambda 4959+5007$ as a temperature indicator and the following density diagnostics: $[Cl\text{ III}] \lambda 5538/\lambda 5518$, $[Fe\text{ III}] \lambda 4658/\lambda 4702$, $[O\text{ II}] \lambda 3726/\lambda 3729$, $[S\text{ II}] \lambda 6731/\lambda 6716$ and $[Ar\text{ IV}] \lambda 4740/\lambda 4711$, we estimate the convergence in T_e and n_e and their uncertainties in every case. The central value of T_e or n_e corresponds to the median of the Monte Carlo distribution and the errors are represented by the deviations to 84th and 16th percentiles. After this procedure, all diagnostics (either T_e or n_e), will have a result for each cross-comparison.

For the nebular components on each cut, we define the representative n_e as the weighted mean⁴ in each cross-comparison with all the the temperature indicators. In the case of high-velocity components, the treatment is more complex since all the density diagnostics based on CELs reveal considerably higher densities than in the nebular components, reaching values at or above the critical densities of the atomic levels involved in some diagnostics as it is shown in Table 6. At densities of $10^4 - 10^6 \text{ cm}^{-3}$, diagnostics based on $[Fe\text{ III}]$ lines are more reliable than other classic ones such as $[O\text{ II}] \lambda 3726/\lambda 3729$ or $[S\text{ II}] \lambda 6731/\lambda 6716$. In addition, dust destruction processes release gaseous Fe in the shock front that should favor the larger contribution of the emission of $[Fe\text{ III}]$ lines of the post-shock gas and, therefore, the derived physical conditions would be biased to those of the post-shock zones. We adopted a maximum-likelihood method to determine the density from $[Fe\text{ III}]$ lines for

³ <http://www.pa.uky.edu/peter/newpage/>

⁴ The weights were defined as the inverse of the square of the error associated to each density diagnostic.

Table 4. Atomic data set used for collisionally excited lines.

Ion	Transition Probabilities	Collision Strengths
O ⁺	Froese Fischer & Tachiev (2004)	Kisielius et al. (2009)
O ²⁺	Wiese et al. (1996), Storey & Zeippen (2000)	Storey et al. (2014)
N ⁺	Froese Fischer & Tachiev (2004)	Tayal (2011)
Ne ²⁺	McLaughlin et al. (2011)	McLaughlin et al. (2011)
S ⁺	Podobedova et al. (2009)	Tayal & Zatsarinny (2010)
S ²⁺	Podobedova et al. (2009)	Grieve et al. (2014)
Cl ⁺	Mendoza & Zeippen (1983)	Tayal (2004)
Cl ²⁺	Fritzsche et al. (1999)	Butler & Zeippen (1989)
Cl ³⁺	Kaufman & Sugar (1986), Mendoza & Zeippen (1982b), Ellis & Martinson (1984)	Galavis et al. (1995)
Ar ²⁺	Mendoza (1983), Kaufman & Sugar (1986)	Galavis, Mendoza & Zeippen (1995)
Ar ³⁺	Mendoza & Zeippen (1982a)	Ramsbottom & Bell (1997)
Fe ²⁺	Quinet (1996), Johansson et al. (2000)	Zhang, Hong Lin (1996)
Fe ³⁺	Froese Fischer et al. (2008)	Zhang & Pradhan (1997)
Ni ²⁺	Bautista (2001)	Bautista (2001)

Table 5. Effective recombination coefficients used for recombination lines.

Ion	Reference
H ⁺	Storey & Hummer (1995)
He ⁺	Porter et al. (2012, 2013)
O ⁺	Pequignot et al. (1991)
O ²⁺	Storey et al. (2017)
C ²⁺	Davey et al. (2000)
Ne ²⁺	Kisielius et al. (1998)

Table 6. Critical densities of density diagnostics for $T_e = 10000$ K.

Ion	$\lambda(\text{\AA})$	$n_{\text{crit}}(\text{cm}^{-3})$
[O II]	3729, 3726	$1.30 \times 10^3, 4.06 \times 10^3$
[S II]	6731, 6716	$3.06 \times 10^3, 1.16 \times 10^3$
[Cl III]	5538, 5518	$3.57 \times 10^4, 7.23 \times 10^3$
[Fe III]	4658, 4701	$5.17 \times 10^6, 3.09 \times 10^6$
[Ar IV]	4740, 4711	$1.26 \times 10^5, 1.39 \times 10^4$

the high-velocity components. This procedure and its interpretation is described in detail in Section 4.2.

Finally, using the adopted representative n_e , we calculate T_e with the available diagnostics using the *getTemDen* task of PyNeb. Assuming the scheme of two ionization zones, we define $T_e(\text{high})$ as the weighted mean T_e obtained from $[\text{Ar III}]\lambda 5192/\lambda 7136+7751$, $[\text{O III}]\lambda 4363/\lambda 4959+5007$ and $[\text{S III}]\lambda 6312/\lambda 9069+9531$ line ratios. Similarly, we define $T_e(\text{low})$ based on the resulting T_e obtained from $[\text{S II}]\lambda 4069+76/\lambda 6716+31$, $[\text{N II}]\lambda 5755/\lambda 6584$ and $[\text{O II}]\lambda 3726+29/\lambda 7319+20+30+31$ line ratios.

It is remarkable that in the nebular component of all cuts the observed $[\text{S III}]\lambda 9531/\lambda 9069$ line intensity ratio does not agree with the theoretical value. This is owing to strong telluric absorptions that affect the $[\text{S III}]\lambda 9069$ line that, on the other hand, do not affect the blueshifted lines of the high velocity components. After an inspection in the 2D spectra of the calibration star and in the science object, we concluded that $[\text{S III}]\lambda 9531$ is not affected by telluric absorptions or emissions at the earth velocities at which the observations were taken. In the nebular component of all cuts, we assumed the theoretical ratio $I([\text{S III}]\lambda 9531)/I([\text{S III}]\lambda 9069) = 2.47$ obtained from the atomic data given in Table 4 to estimate $T_e([\text{S III}])$.

Plasma diagnostic plots shown in Fig. A1, indicate that the

resulting values of each diagnostic are consistent with each other. The numerical values in each case are presented in Table 7.

4.2 Physical conditions based on [Fe III] lines.

As it was mentioned in Section 4, density diagnostics based on different [Fe III] line intensity ratios give apparently discordant results. This is mainly due to the ambivalence in the density dependence of some observed intensity ratios and/or due to their high dependence on T_e as well as on n_e . These two scenarios are exemplified in Fig. 5 for [Fe III] $\lambda 4881/\lambda 4658$ and $\lambda 5271/\lambda 4658$ line ratios. For the expected densities in the different components observed in this work (n_e between $\sim 10^3 \text{ cm}^{-3}$ and $\sim 10^5 \text{ cm}^{-3}$), these diagnostics are not very enlightening on their own. On the other hand, [Fe III] $\lambda 4658/\lambda 4702$ is the most reliable diagnostic in our case. However, although there is no ambivalence at the expected densities, the predicted value for the [Fe III] $\lambda 4658/\lambda 4702$ intensity ratio varies little in a relatively wide range of densities. As a consequence, the deduced density from [Fe III] $\lambda 4658/\lambda 4702$ inherently will have large uncertainties, even with relatively low errors in the line fluxes.

We consider that the best way to determine the physical conditions based on the observed intensity ratios of [Fe III] lines is with a maximum-likelihood process. This method is based on a χ^2 minimization by testing a wide range of parameters. The value of χ^2 is defined in Eq. (2), as the sum of the quadratic differences between the abundance of ion X^i (in this case Fe^{2+}) determined with each emission line included in the procedure and the weighted average defined in Eq. (3).

$$\chi^2 = \sum_{\lambda} \frac{\left(n\left(\frac{X^i}{H^+}\right)_{\lambda} - \overline{n\left(\frac{X^i}{H^+}\right)} \right)^2}{\Delta n\left(\frac{X^i}{H^+}\right)_{\lambda}}, \quad (2)$$

$$\overline{n\left(\frac{X^i}{H^+}\right)} = \frac{\sum_{\lambda} \left(n\left(\frac{X^i}{H^+}\right)_{\lambda} / \Delta n\left(\frac{X^i}{H^+}\right)_{\lambda} \right)^2}{\sum_{\lambda} \left(1 / \Delta n\left(\frac{X^i}{H^+}\right)_{\lambda} \right)}. \quad (3)$$

This self-consistent procedure gives the physical parameters that minimize χ^2 with an associated uncertainty based on the resulting values within $\chi^2 - \chi^2_{\min} \leq 1$. This method requires a strict

Table 7. Physical conditions.

Diagnostic	Cut 1 Nebula	Cut 2 HH529II	Cut 2 Nebula	Cut 3 HH529III	Cut 3 Nebula	Cut 4 Nebula	Combined Cuts
[O II] $\lambda\lambda 3726/\lambda 3729$	5460 $^{+1000}_{-750}$	10570 $^{+3680}_{-2420}$	5220 $^{+960}_{-720}$	18020 $^{+17170}_{-800}$	5530 $^{+1000}_{-800}$	5070 $^{+880}_{-710}$	5530 $^{+990}_{-810}$
[S II] $\lambda\lambda 6731/\lambda 6716$	4230 $^{+1500}_{-980}$	9390 $^{+10170}_{-3950}$	4160 $^{+1570}_{-1040}$	13130 $^{+15820}_{-6550}$	4130 $^{+2020}_{-1150}$	4160 $^{+1400}_{-960}$	4510 $^{+2270}_{-1320}$
[Cl III] $\lambda\lambda 5538/\lambda 5518$	7020 $^{+900}_{-900}$	8170 $^{+1810}_{-1610}$	6670 $^{+860}_{-860}$	15040 $^{+4490}_{-4490}$	7370 $^{+1190}_{-1120}$	7000 $^{+960}_{-900}$	7420 $^{+1190}_{-1190}$
[Fe III] $\lambda\lambda 4658/\lambda 4702$	9260 $^{+3700}_{-2890}$	12390 $^{+5010}_{-3460}$	8990 $^{+2840}_{-2350}$	33800 $^{+33820}_{-10530}$	10490 $^{+4240}_{-3090}$	8340 $^{+3620}_{-2530}$	9510 $^{+3790}_{-2750}$
[Ar IV] $\lambda\lambda 4740/\lambda 4711$	4480 $^{+1700}_{-1640}$	6410 $^{+1900}_{-1880}$	5920 $^{+980}_{-940}$	15050 $^{+13300}_{-9240}$	6400 $^{+1690}_{-1660}$	5460 $^{+1000}_{-1050}$	6580 $^{+2000}_{-1870}$
O II*	4710 \pm 710	3490 \pm 340	4390 \pm 400	3600 \pm 850	4920 \pm 550	4350 \pm 610	5420 \pm 690
[Fe III]*	8530 \pm 1050	11880 \pm 1860	9430 \pm 1010	44090 \pm 7580	8530 \pm 1160	9020 \pm 1170	10360 \pm 1410
Adopted	5830 \pm 1210	11880 \pm 1860	5870 \pm 970	44090 \pm 7580	6180 \pm 1220	5650 \pm 1030	6290 \pm 1130
T_e (K)							
T(H I) _{Balmer}	-	-	-	-	-	-	7520 \pm 790
T(H I) _{Paschen}	-	-	-	-	-	-	7550 \pm 1160
T(He I)	8280 $^{+520}_{-570}$	7200 \pm 550	8060 $^{+540}_{-510}$	7340 \pm 710	8090 \pm 530	7390 $^{+470}_{-580}$	7690 $^{+500}_{-510}$
[N II] $\lambda\lambda 5755/\lambda 6584$	9910 \pm 250	10150 $^{+570}_{-510}$	9850 \pm 240	10020 $^{+740}_{-650}$	10060 $^{+260}_{-280}$	9860 $^{+250}_{-270}$	9990 $^{+250}_{-270}$
[O II] $\lambda\lambda 3726+29/\lambda\lambda 7319+20+30+31$	10340 $^{+1330}_{-940}$	-	-	-	-	11230 $^{+1330}_{-1110}$	10910 $^{+1320}_{-950}$
[S II] $\lambda\lambda 4069+76/\lambda\lambda 6716+31$	11430 $^{+3290}_{-1870}$	-	11070 $^{+2420}_{-1450}$	-	10550 $^{+2450}_{-1570}$	10790 $^{+2340}_{-1470}$	11000 $^{+2510}_{-1600}$
[O III] $\lambda\lambda 4363/\lambda\lambda 4959+5007$	8430 \pm 90	8240 \pm 80	8410 $^{+80}_{-90}$	8500 $^{+110}_{-120}$	8510 \pm 90	8320 \pm 90	8450 $^{+80}_{-90}$
[S III] $\lambda\lambda 6312/\lambda\lambda 19069+9531$	9220 $^{+290}_{-330}$	8670 \pm 310	8990 $^{+290}_{-330}$	8960 $^{+370}_{-500}$	8920 $^{+330}_{-300}$	8850 $^{+290}_{-320}$	8970 $^{+280}_{-290}$
[Ar III] $\lambda\lambda 5192/\lambda\lambda 7136+7751$	8280 $^{+280}_{-310}$	8620 $^{+500}_{-540}$	8390 $^{+220}_{-280}$	-	8250 $^{+260}_{-290}$	8280 $^{+380}_{-420}$	8270 $^{+280}_{-320}$
O II*	-	-	9350 \pm 1090	-	-	-	-
[Fe III]*	7800 \pm 800	8500 \pm 1050	8450 \pm 730	8440 \pm 2260	7600 \pm 710	7350 \pm 590	8440 \pm 710
T_e (low) Adopted	9930 \pm 140	10150$^{+570}_{-510}$	9860 \pm 240	10020$^{+740}_{-650}$	10070 \pm 270	9920 \pm 280	10040 \pm 210
T_e (high) Adopted	8470 \pm 200	8270 \pm 110	8440 \pm 140	8530 \pm 100	8510 \pm 120	8360 \pm 140	8480 \pm 150

* A maximum likelihood method was used.

control on the variables that affect the line fluxes, otherwise a spurious contribution appears, and can change the resulting parameters that minimize χ^2 . For example, undetected blends in the studied lines can result in incorrect density and/or temperature determinations.

We have considered several aspects to choose the set of [Fe III] lines that should be included in the maximum-likelihood process. We discard lines with evident line blending or contamination by telluric emission or ghosts. To test unnoticed line blends or inaccuracies in flux estimations, we use ratios of observed lines that should depend only on transition probabilities and not on physical conditions. The results are shown in Table 8. As it can be seen, there is a good agreement between the theoretical and observed values in the cases of [Fe III] $\lambda\lambda 4778/\lambda 4734, \lambda 4702/\lambda 4770$ and $\lambda 4658/\lambda 4755$ line ratios. Deviations between the theoretical and the observed values in the cases of [Fe III] $\lambda 4667/\lambda 4734, \lambda 4778/\lambda 4667, \lambda 4607/\lambda 4702$ and $\lambda 4607/\lambda 4770$ line ratios are explained by the contamination of [Fe III] $\lambda 4667$ by a ghost and by the blend of [Fe III] $\lambda 4607$ with N II $\lambda 4607.15$. The line ratio with the largest deviation is [Fe III] $\lambda 5011/\lambda 4085$. This could be mainly due to the low signal-to-noise ratio of the [Fe III] $\lambda 4085$ line. However, [Fe III] $\lambda 5011$ is located close to [O III] $\lambda 5007$ that present broad wings in its line profile that affects the shape of the continuum close to [Fe III] $\lambda 5011$ and perhaps the measurement of its line flux.

We select the following [Fe III] lines for the maximum-likelihood process: $\lambda\lambda 4658.17, 4701.64, 4734.00, 4881.07, 5270.57$ and 5412.06 . This selection includes the brightest [Fe III] lines that are free of blends or telluric emissions and/or absorptions. We exclude fainter lines coming from the same upper level since they should have the same dependence on physical conditions and their incorporation would only increase the noise level of the results. This selection includes lines in a relatively small spectral range and hence, uncertainties in the reddening correction would have a negligible effect. This allow us to restrict the parameter space to electron density and temperature to test χ^2 . Studies on the primordial he-

lium abundance have used similar maximum-likelihood procedures to calculate the He^+ abundance, noting that this procedure can lead to degeneracies in the fitted parameters and χ^2 (see Olive & Skillman 2004; Aver et al. 2011, and references therein). Because of this, it is important to have an overview of the behavior of χ^2 in the complete parameter space.

In Fig. 6 we present the convergence of χ^2 in the $n_e - T_e$ space for both high-velocity and nebular components of cut 2. As it can be seen, χ^2 falls into a single minimum in each case, corresponding to $T_e = 8500 \pm 1050$ K and $n_e = 11880 \pm 1860 \text{ cm}^{-3}$ for HH529II and $T_e = 8460 \pm 730$ K and $n_e = 9430 \pm 1010 \text{ cm}^{-3}$ for the nebular component. The T_e and n_e values obtained for the rest of cuts using this approach are presented in Table 7. The convergence to the resulting n_e is consistent with the diagnostic based on [Fe III] $\lambda 4658/\lambda 4702$ ratio but with a smaller uncertainty due to the application of the χ^2 maximum-likelihood procedure. It is remarkable that in all cases, [Fe III] lines give n_e values higher than the usual diagnostics based on CELs such as [S II] $\lambda 6731/\lambda 6716$ or [O II] $\lambda 3726/\lambda 3729$. The largest difference is found in the high-velocity components, reaching almost a factor 3 in HH529III. In the case of nebular components this is due to the low sensitivity of the used [Fe III] lines at smaller densities than $\sim 10^3 \text{ cm}^{-3}$, which gives more weight to the higher-density zones within the line of sight. On the other hand, in the high-velocity components, the larger differences suggest the presence of high densities in the range of $10^4 - 10^5 \text{ cm}^{-3}$, where the usual density diagnostics are uncertain, being well above the critical densities as it is shown in Table 6. In addition, the geometry of the HH529 flow and dust destruction (see Section 8.1.3) can contribute to that difference. We estimate an average flow angle of $\sim 58^\circ$ (see Section 10.1) with respect to the sky plane for HH529, partially flowing towards the observer. Since both bow shocks are fully photoionized (see Section 10.1), the volume of gas integrated in the high-velocity components may include not only the denser gas of the head of the shock but also some contribution of the jet beam gas behind. As we discuss in Section 8.1.3, the gaseous Fe abundance is

Table 8. Comparison of the observed [Fe III] intensity ratios and theoretical ones from Quinet (1996).

Ratio	Cut 1 Nebula	Cut 2 HH529II Nebula	Cut 3 HH529III Nebula	Cut 4 Nebula	Combined cuts	Quinet (1996)
4667/4734*	-	0.52 ± 0.04	0.42 ± 0.02	-	0.45 ± 0.03	0.43 ± 0.03
4778/4734	0.51 ± 0.04	0.70 ± 0.06	0.51 ± 0.03	0.34 ± 0.08	0.49 ± 0.03	0.43 ± 0.04
4778/4667*	-	1.35 ± 0.14	1.22 ± 0.06	-	1.09 ± 0.07	1.00 ± 0.09
4607/4702**	0.24 ± 0.01	0.22 ± 0.02	0.24 ± 0.01	0.24 ± 0.05	0.23 ± 0.02	0.24 ± 0.02
4607/4770**	0.72 ± 0.05	0.60 ± 0.06	0.64 ± 0.03	0.52 ± 0.11	0.64 ± 0.06	0.68 ± 0.05
4702/4770	2.96 ± 0.15	2.68 ± 0.16	2.73 ± 0.10	2.22 ± 0.27	2.74 ± 0.19	2.87 ± 0.14
4658/4755	5.50 ± 0.20	5.28 ± 0.24	5.26 ± 0.15	4.70 ± 0.51	5.32 ± 0.24	5.30 ± 0.19
5011/5085	3.19 ± 0.72	2.51 ± 0.93	5.00 ± 1.00	2.96 ± 1.22	3.61 ± 0.46	3.84 ± 0.94
						3.66 ± 0.96
						5.94

* $\lambda 4667$ affected by ghost.

** [Fe III] $\lambda 4607.12$ blended with N II $\lambda 4607.15$.

higher at the high-velocity components due to the dust destruction where the Fe is commonly depleted (Mesa-Delgado et al. 2009; Espírito et al. 2017), increasing the flux of [Fe III] lines relative to that of other CELs that are not usually found in dust grains. Therefore, the n_e determinations based on [Fe III] lines will be biased to the higher values of the density at the head of the shock.

The procedure indicates a higher affinity between T_e ([Fe III]) and T_e (high), contrary to what the ionization potential of Fe^{2+} would suggest, closer to N^+ than O^{2+} , which are ions representative of the low and high ionization zones, respectively. In the case of the nebular components, the fact that the [Fe III] density diagnostics weight more the high-density zones in the line of sight, as we mentioned previously, may condition the results to lower temperatures, which are not representative for all the Fe^{2+} . On the other hand, in the high-velocity components, this may indicate that on the shock front, where further dust destruction and incorporation of Fe into the gas phase is expected, the high-ionization gas dominates over the remaining low-ionization one, which may be flowing behind of the shock front. This suggests that the optimal temperature to calculate the Fe^{2+} abundance in the high-velocity components is T_e (high). Estimates of Fe^{2+} abundances based on both T_e (low) and T_e (high) will be discussed separately in Section 8.1.3.

4.3 Physical conditions based on RLs

4.3.1 Physical conditions based on O II RLs

To estimate physical conditions based on O II RLs, we use the effective recombination coefficients from Storey et al. (2017). These coefficients fully account the dependence on electron density and temperature of the distribution population among the ground levels of O II. We follow a similar maximum-likelihood procedure as described in Section 4.2. In this case, we chose the observed lines from multiplet 1 and $\lambda\lambda 4089.29, 4275.55$ from 3d-4f transitions, due to the following reasons: (1) lines from multiplet 1 are the brightest O II RLs and are comparatively less affected by line blending or instrumental reflections as it is illustrated in Fig. 7. (2) The density dependence of the line intensity ratios of multiplet 1 relies on variations in the density population of 3P_J levels and formally reach the equilibrium with the statistical weight of the levels until $n_{\text{crit}} \approx 10^5 \text{ cm}^{-3}$ (Storey et al. 2017). (3) O II $\lambda\lambda 4089.29, 4275.55$ RLs corresponding to 3d-4f transitions depend strongly on T_e . Nevertheless, these lines are relatively weak and we expect comparatively larger uncertainties in the T_e determinations than using diagnostics based on CELs.

Fig. 8 shows χ^2 -maps in the space of T_e and n_e for both components of cut 2. As it can be seen, HH529II has a temperature

degeneracy. This is not surprising, due to the fact that multiplet 1 is rather independent of T_e and the weak line $\lambda 4275.55$ is the only one that can break the degeneracy in this component since O II $\lambda 4089.29$ is blended with a ghost feature (see Section 4.3.2). However, it is clear that the density dependence is well limited within a range of $3000\text{--}3700 \text{ cm}^{-3}$. Fixing the temperature to the adopted one for the high ionization zone using CELs, we obtain $n_e = 3490 \pm 340 \text{ cm}^{-3}$ for HH529II. On the other hand, since we were able to use the O II $\lambda 4089.29$ together with $\lambda 4275.55$ in the nebular component of cut 2, we have a convergence within a more limited interval of values. The physical conditions that minimizes χ^2 in this case are $n_e = 4390 \pm 400 \text{ cm}^{-3}$ and $T_e = 9350 \pm 1090 \text{ K}$. This result is compatible with T_e ([O III]) within the uncertainties, indicating that the emission of CELs and RLs of O^{2+} comes basically from the same gas (see Section 8.3).

In Table 7, we can see that the density values obtained from O II lines are similar to those obtained from other diagnostics in the nebular components but lower in the high-velocity ones. This is because, although formally the population of the 3P_J levels from O^{2+} reach the statistical equilibrium until densities of $\sim 10^5 \text{ cm}^{-3}$, the density dependence becomes rather weak from values above $\sim 10^4 \text{ cm}^{-3}$, as it is shown in Fig. 4 from Storey et al. (2017). Therefore, the values obtained by this diagnostic may not be representative of the shock front, where the density is expected to be higher than 10^4 cm^{-3} .

4.3.2 The alleged observation of Si IV $\lambda 4088.86$ line

Several authors used the $I(\text{OII } \lambda 4649.13)/I(\text{OII } \lambda 4089.29)$ ratio to derive T_e based on its theoretical high dependence on T_e and low dependence on n_e (see e. g. García-Rojas & Esteban 2007; Fang & Liu 2013; McNabb et al. 2013; Wesson et al. 2018). The low dependence of this ratio on n_e is because both lines come from the 3P_J levels of highest J , depending the population of both levels on the population of the 3P_2 ground level (Storey et al. 2017). Nevertheless, Peimbert & Peimbert (2013) discourages its use, due (among other reasons) to the possible contamination of O II $\lambda 4089.29$ by the Si IV $\lambda 4088.86$ line, granting lower T_e values. The authors consider that Si IV $\lambda 4088.86$ has been detected in 2 H II regions observed with UVES echelle spectrograph at VLT telescope: the Orion Nebula (Esteban et al. 2004) and 30 Doradus (Peimbert 2003). Although it is a real possibility that a line like Si IV $\lambda 4088.86$ may be detected in an H II region, much of the flux attributed to this line is actually due to an observational artifact of UVES spectrum.

Fig. A2 shows the echelle orders extracted in an UVES blue

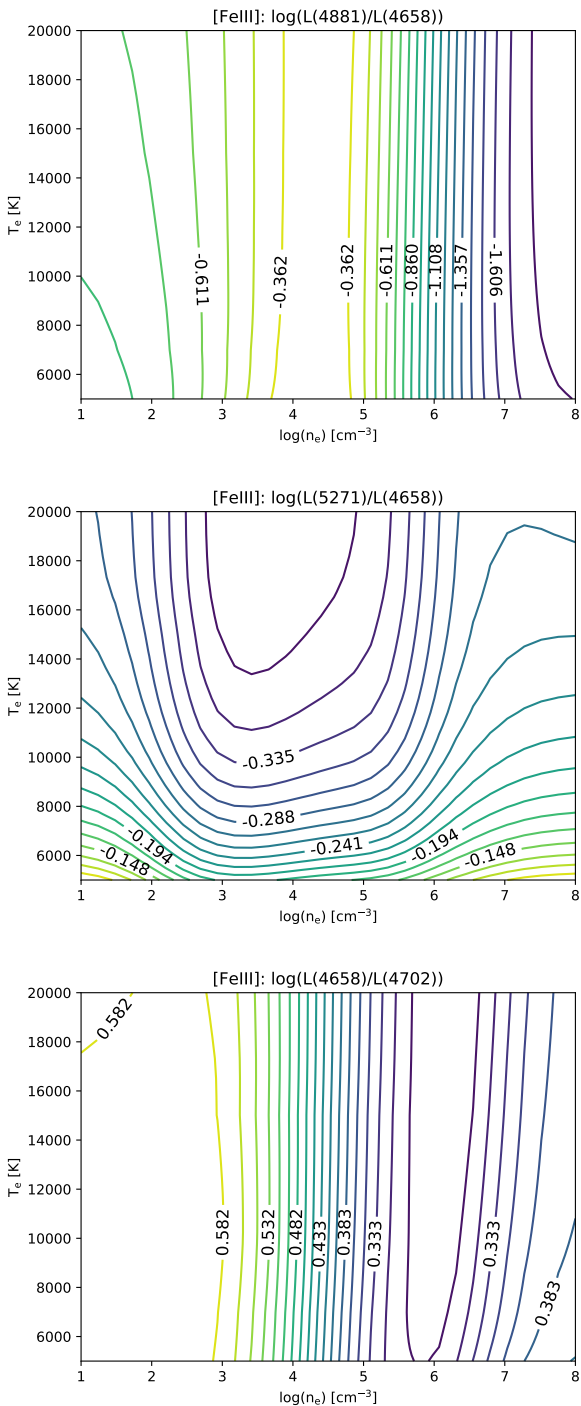


Figure 5. Predicted dependence of the [Fe III] $\lambda 4881/\lambda 4658$, $\lambda 5271/\lambda 4658$ and $\lambda 4658/\lambda 4702$ line intensity ratios with physical conditions.

arm spectrum using dichroic 2 ($\Delta\lambda = 3750 - 4995$). Optical reflections produced by the dichroic 2 in the blue arm can be noted as vertical lines crossing the echelle orders. These artifacts are negligible with the exception of those produced by the most intense lines: [O III] $\lambda 4959$, H β and [O III] $\lambda 5007$ that, despite it does not enter in any complete echelle order in this arm, it is partially observed at the edge of the CCD, as well as its associated high-velocity component. As consequence 4 main sources of “ghost lines” can be immedi-

ately noticed, the third of them (from left to right), affects exactly the $\lambda 4089.07$ position in the echelle order number 11 (bottom up) in our observations. Approximately at this wavelength we expect to have the high velocity component of O II $\lambda 4089.29$ in cuts 2 and 3, but it must be free of emission from HH529III in cut 4. Fig. 9 shows the emission around $\lambda 4089.29$ in the spectra of cut 4, a pretty similar image than the Fig. 2 from Peimbert & Peimbert (2013).

In our spectra, an hypothetical Si IV $\lambda 4088.86$ line should be observed at $\lambda 4089.08$, considering the kinematical structure of the nebular component and the high ionization potential of the line (see Section 9.1). This means that in case of being detected, the Si IV $\lambda 4088.86$ line would be indistinguishable from the ghost line at $\lambda 4089.07$. We have measured the intensity of ghost lines coming from the same source than $\lambda 4089.07$ along the echelle orders but excluding those ones which are blended with other nebular lines. Fig. A3 shows the decreasing trend of the intensity of ghost emission with respect to its source from higher to lower orders, as well as a least squares fit to predict ghost emission in order 11, where the emission feature at $\lambda 4089.07$ lies. The predicted ghost emission in $\lambda 4089.07$ is $\frac{F(\lambda)}{F(H\beta)} = 0.007$ while the rms of the noise associated with the continuum in cut 4 around $\lambda 4089.07$ represents a possible contribution of $\frac{F(\text{rms})}{F(H\beta)} = 0.004$. On the other hand, the measured flux of $\lambda 4089.07$ is $\frac{F(\lambda)}{F(H\beta)} = 0.012$. Thus, the emission observed at $\lambda 4089.07$ is consistent with purely ghost emission. This ghost emission affects in a similar way the spectra of the Orion Nebula and 30 Dor analyzed by Esteban et al. (2004) and Peimbert (2003), respectively.

The main drawback of the T_e diagnostic based on the $I(\text{O II } \lambda 4649.13)/I(\text{O II } \lambda 4089.29)$ ratio in H II regions is that $\lambda 4089.29$ is rather weak, providing uncertain T_e values. Therefore, this diagnostic will only be useful when the O II lines are well measured, or when the object shows significant difference between the T_e of the zone where the O II lines are formed and the rest of the nebula (Wesson et al. 2018). Finally, although Si IV lines are expected to be rather faint in normal H II regions, this may not be the case in high-ionization planetary nebulae (PNe) as NGC 3918 (García-Rojas et al. 2015).

4.3.3 Electron temperature from He I recombination line ratios

Following the procedure used by Zhang et al. (2005) for PNe, we have used the $I(\text{He I } \lambda 7281)/I(\text{He I } \lambda 6678)$ ratio for deriving T_e (He I). The use of those particular lines have several advantages. First, $\lambda 7281$ and $\lambda 6678$ are among the brightest He I RLs and their use minimizes observational errors. Second, they are produced in transitions between singlet levels, ensuring that they are free of significant self-absorption effects. We have explored the temperature dependence of other intensity ratios of He I $\lambda 7281$ with respect to other relevant singlet lines apart of $\lambda 6678$ as $\lambda\lambda 4388, 4922, 4438, 3614, 3965$ and 5016 using the recombination coefficients of Porter et al. (2012, 2013). Intensity ratios of transitions coming from 5^1D , 4^1D , 3^1D levels to 2^1P show the highest dependence on T_e (see Fig. A4). 2^1P is the same down level of the transition producing the He I $\lambda 7281$ line, which comes from the 3^1S level. On the other hand, comparatively, the $I(\text{He I } \lambda 7281)/I(\text{He I } \lambda 6678)$ ratio has the smallest n_e dependence, in agreement with the conclusion of Zhang et al. (2005), despite using different recombination coefficients.

Fig. A5 shows that the T_e dependence of $I(\text{He I } \lambda 7281)/I(\text{He I } \lambda 6678)$ ratio is practically linear in the interval $5000 \text{ K} \leq T_e(\text{K}) \leq 10000 \text{ K}$. The deviation between the determination of $T_e(\text{He I})$

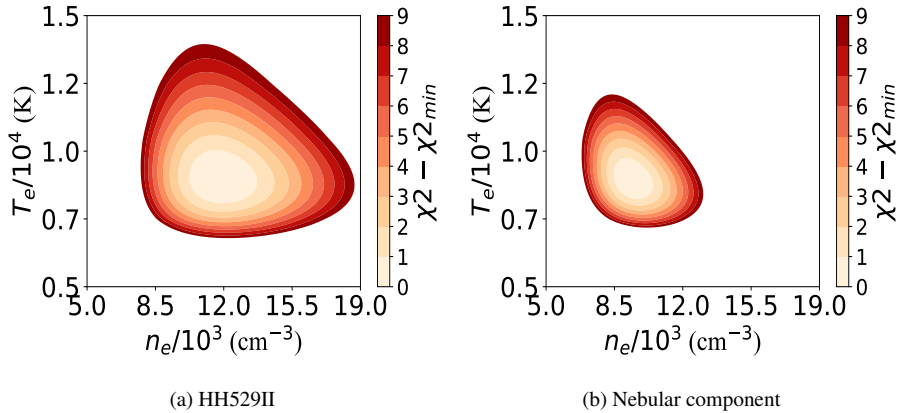


Figure 6. χ^2 in the space of T_e and n_e in the maximum-likelihood procedure for [Fe III] lines. Both in the case of HH529II (left panel) and the nebular component of cut 2 (right panel) there is a convergence to well defined physical conditions.

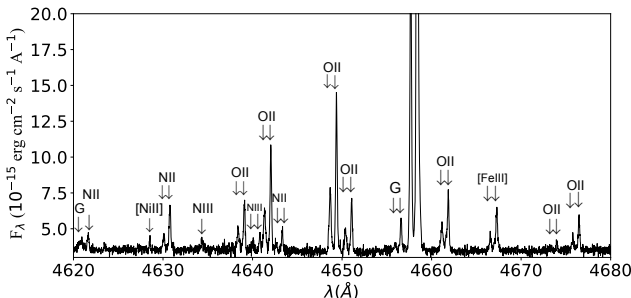


Figure 7. Section of the spectrum of the spatial cut 2 covering the spectral range 4620–4680 Å. Several couples of O II lines from multiplet 1 are present, showing the quality of the spectra of HH529II and the nebular component. Emissions marked with a G are ghosts (see § 4.3.2).

using a linear fit (as in Eq. (4)) and a more complex interpolation of the recombination coefficients of Porter et al. (2012, 2013) is always smaller than 35 K. At $T_e > 10000$ K, any linear fit will fail for almost all n_e values except for the lowest ones ($n_e \leq 100$ cm $^{-3}$). In these cases, a more complex treatment is necessary to estimate $T_e(\text{He I})$. The linear fit (slope and intercept) varies significantly in the lower density ranges, and tends to remain almost constant for densities $n_e \geq 10000$ cm $^{-3}$.

$$T_e(\text{He I}) (\text{K}) = \alpha \left[\frac{I(\lambda 7281)}{I(\lambda 6678)} \right] + \beta. \quad (4)$$

In Table A1, we present the slope and intercept values given by Eq. (4) for a density range representative for H II regions and some PNe. The resulting $T_e(\text{He I})$, using the average values obtained with $I(\lambda 7281)/I(\lambda 6678)$, $I(\lambda 7281)/I(\lambda 4922)$ and $I(\lambda 7281)/I(\lambda 4388)$ ratios, all consistent with each other, are included in Table 7 for all components.

4.4 Electron temperature determinations from nebular continuum.

Thanks to the high signal-to-noise ratio of our spectra, we can obtain a good determination of the Balmer and Paschen discontinuities of the nebular continuum in the spectrum obtained adding all the cuts (see Fig. 10). We used Eq. (5), taken from Liu et al. (2001) for $\text{He}^{2+}/\text{H}^+ = 0$ to estimate $T_e(\text{HI})_{\text{Balmer}}$. This formula

is based on theoretical continuum emission of HI, He I and He II calculated by Brown & Mathews (1970) and the theoretical line emission of HI $\lambda 3770.63$ (H11) from Storey & Hummer (1995). Analogously, we used Eq. (6), taken from Fang & Liu (2011) to estimate $T_e(\text{HI})_{\text{Paschen}}$ using the measured Paschen discontinuity and the intensity of HI $\lambda 8862.78$ (P11) line.

$$T_e(\text{HI})_{\text{Balmer}} (\text{K}) = 368 \times \left(1 + 0.259 \frac{\text{He}^+}{\text{H}^+} \right) \left(\frac{\text{BJ}}{\text{H11}} \right)^{-3/2}. \quad (5)$$

$$T_e(\text{HI})_{\text{Paschen}} (\text{K}) = 8.72 \times \left(1 + 0.52 \frac{\text{He}^+}{\text{H}^+} \right) \left(\frac{\text{PJ}}{\text{P11}} \right)^{-1.77}. \quad (6)$$

The estimation of the temperature requires a precise fit to the continuum emission at both sides of 3646 Å and 8204 Å, the approximate wavelengths of the Balmer and Paschen discontinuities, respectively, since both estimations are very sensitive to changes in the jump value. We do not determine $T_e(\text{HI})_{\text{Balmer}}$ and $T_e(\text{HI})_{\text{Paschen}}$ in the rest of the cuts because of the much larger noise level of the continuum in their spectra. However, using the spectrum of the combined cuts has the drawback of mixing the emission of the nebular and the high-velocity components in the continuum. In any case, as Bohigas (2015) suggests, the total $T_e(\text{HI})$ would be the weighted average of the individual values of the mixed components, where the weight would be the H^+ mass of each component. Thus, considering that the high-velocity component should contain a much smaller mass, we can assume that the contribution of the high-velocity component to the continuum should be negligible, not affecting the $T_e(\text{HI})$ determination in a substantial manner.

Fig. 10 shows the discontinuities and the fitted Balmer and Paschen continua in the normalized and reddening corrected spectrum. The best fit is achieved with $\text{BJ}/I_{H\beta} = 0.532 \pm 0.036$ and $\text{PJ}/I_{H\beta} = 0.031 \pm 0.002$.

5 CHEMICAL ABUNDANCES

5.1 Ionic abundances from CELs

We determine the ionic abundances based on the observed CELs using the PyNeb routines and the transition probabilities and collisional strengths given in Table 4. Abundances for O $^+$, N $^+$, S $^+$, Ni $^{2+}$ and Cl $^+$ were derived using the n_e and $T_e(\text{low})$ adopted for each

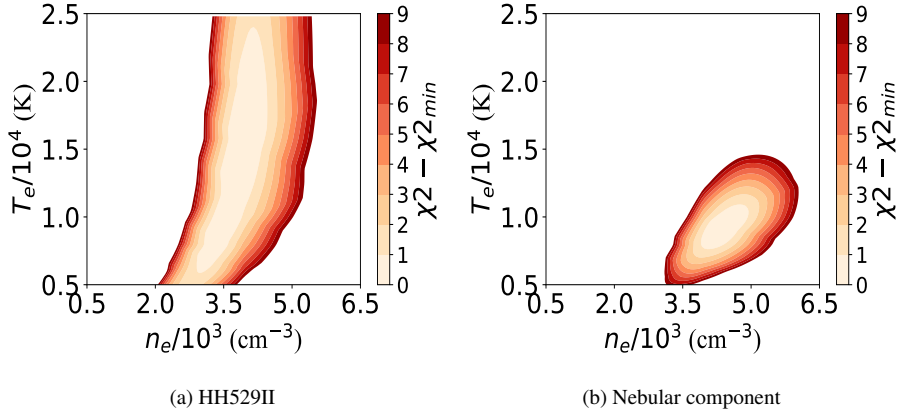


Figure 8. The same as in Fig. 6 but using O II lines. In this case, there is an evident T_e degeneration in HH529II (right panel) due to that the temperature-dependent O II RL $\lambda\lambda 4089.29$ cannot be measured in its spectrum. A clear convergence can be seen in the nebular component (right panel). The uncertainties are somewhat large owing to the relative weakness of the temperature-dependent O II lines ($\lambda\lambda 4089.23, 4275.55$).

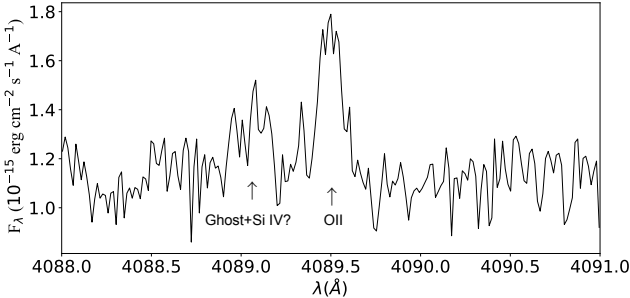


Figure 9. Emission spectrum of the spatial cut 4 around $\lambda 4089.29$. There are no high-velocity components in this spatial cut.

component of each cut, while abundances for O^{2+} , Ne^{2+} , Cl^{3+} , Fe^{3+} , Ar^{2+} and Ar^{3+} rely on the adopted $T_e(\text{high})$. S^{2+} and Cl^{2+} abundances were derived using $T_e([S\ III])$. In the case of Fe^{2+} , estimations of its abundance are presented using both $T_e(\text{high})$ and $T_e(\text{low})$ (see Table A2 and Table A3). This will be analyzed in Section 8.1.3. General results are presented in Table 10.

5.1.1 Cl^{2+} and Cl abundances

Domínguez-Guzmán et al. (2019) have proposed the use of $T_e([N\ II])$ to determine the Cl^{2+} abundance in a sample of 37 Galactic and extragalactic H II regions, including the Orion Nebula (using the data of Esteban et al. 2004). They argue that $T_e([N\ II])$ reduces the dispersion of the Cl/O ratio and remove trends in the Cl/O versus O/H relation. However, in a detailed study of each specific object, the optimal temperature to adopt can differ from what statistically would be the best choice. C: Considering the IP of 23.8 eV of Cl^+ , in between of those of N^+ (14.5 eV) and O^{2+} (35.1 eV), we expect that a T_e representative of an intermediate ionization zone as $T_e([S\ III])$ should be more appropriate for determining the Cl^{2+} abundance. In our spectra, we are able to calculate the total Cl abundance because we measure CELs of all the ionization species of Cl that are expected to be present in the Orion Nebula. We test the resulting Cl abundance considering three different temperatures: $T_e(\text{low})$, $T_e([S\ III])$ and $T_e(\text{high})$ for deriving the Cl^{2+}/H^+ ratio. In Table A4, we present the Cl^{2+} and Cl abundances as well as their corresponding Cl/O ratios using the three aforementioned temperatures.

Using $T_e(\text{low})$, we obtain a Cl/O ratio in HH529II about 0.1 dex lower with respect to the value found in HH529III and in the nebular components of the different cuts. This suggests that $T_e(\text{low})$ is slightly underestimating the Cl/H ratio, although within the uncertainties. Conversely, the Cl/O ratio becomes more consistent when using $T_e([S\ III])$ or $T_e(\text{high})$ to estimate the Cl^{2+} abundance. We obtain a mean Cl/O ratio of -3.63 ± 0.03 , -3.42 ± 0.03 and -3.50 ± 0.03 when adopting $T_e(\text{low})$, $T_e(\text{high})$ or $T_e([S\ III])$ to calculate the Cl^{2+} abundance, respectively. The Cl/O ratio obtained using $T_e([S\ III])$ is the one closest to the solar value of -3.50 ± 0.09 recommended by Lodders (2019). Therefore, we finally adopt $T_e([S\ III])$ to estimate the Cl^{2+} abundance.

5.1.2 Ni^{2+} abundance

The first estimation of the Ni abundance in an H II region was made by Osterbrock et al. (1992) for the Orion Nebula. They used estimates of the atomic data of Ni ions, considering $[Ni\ II]$ and $[Ni\ III]$ lines. Since then, the number of Ni abundance determinations in ionized nebulae is still very limited, both for PNe (Zhang & Liu 2006; García-Rojas et al. 2013; Delgado-Inglada et al. 2016) and H II regions (Mesa-Delgado et al. 2009; Delgado-Inglada et al. 2016). There is a considerable amount of $[Ni\ II]$ and $[Ni\ III]$ lines in our spectra. However, $[Ni\ II]$ lines are affected by fluorescence (Lucy 1995) and their use to calculate the abundance of Ni^+ is restricted to some particular cases as low-excitation nebulae (Zhang & Liu 2006). On the other hand, $[Ni\ III]$ lines are, in principle, not affected by fluorescence effects and can be used to derive Ni^{2+} abundances. From all the detected $[Ni\ III]$ lines, we chose $[Ni\ III]\ \lambda\lambda 6000, 6534, 6682, 6797, 6946$ and 7890 because they are not affected by blends or telluric absorption.

As we commented in Section 4, all tested diagnostics based on $[Ni\ III]$ lines fail to provide reliable values of physical conditions, indicating inaccuracies between the observed lines and the theoretical predictions. Delgado-Inglada et al. (2016) studied the Fe/Ni ratio in eight PNe and three H II regions, including the Orion Nebula. They used different datasets for these last objects, including the high spectral resolution ones from Esteban et al. (2004) and Mesa-Delgado et al. (2009) (which includes HH202), and some of their own observations covering approximately the same area as the Position 1 of Esteban et al. (1998) and the brightest part of the Orion Bar. We have compared our data with some observed flux ratios

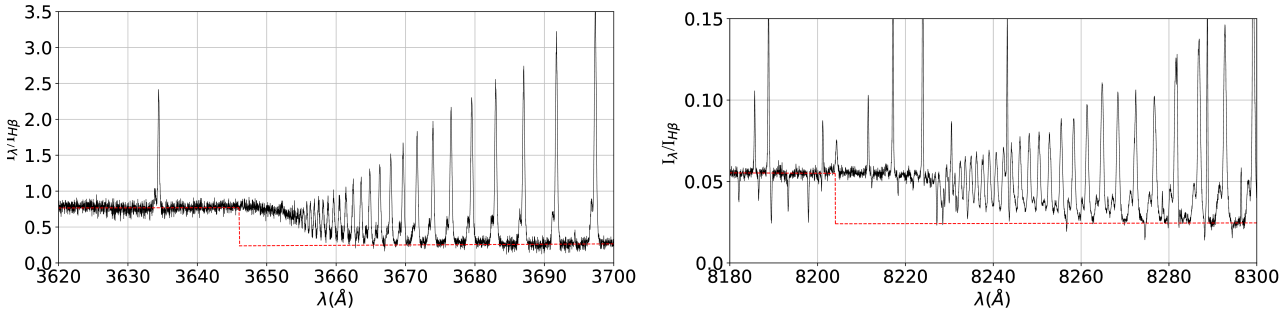


Figure 10. Reddening-corrected spectrum resulting after adding all cuts, showing the Balmer (left panel) and Paschen (right panel) discontinuities. Both jump estimations are shown in red.

compiled by [Delgado-Ingla et al. \(2016\)](#) looking for possible undetected line blends or observational inaccuracies. For convenience, we have compared the predicted and observed flux ratios of [Ni III] $\lambda\lambda 6000, 6534$ and 6946 lines that arise from the same atomic level and therefore we expect that their intensity ratios should be constant. In Table 9, we compare the observed flux ratios and the predicted ones using the atomic data of Ni²⁺ by [Bautista \(2001\)](#). As Table 9 shows, the [Ni III] $\lambda 6534/\lambda 6000$ and $\lambda 6946/\lambda 6000$ intensity ratios are rather inconsistent with the predicted ones, especially in the case of HH529II. **C: In addition, as can be seen in Table A5, we find an inconsistent pattern of Ni²⁺ abundances in all cuts and components for the six selected lines, with differences up to 0.8 dex.** We consider that the nowadays available atomic data of Ni²⁺ seems to be not accurate enough to derive confident values of its ionic abundances. Therefore, our Ni²⁺/H⁺ abundances must be taken with care, since they include unknown uncertainties.

5.2 Ionic abundances from RLs

5.2.1 He⁺ abundance

To estimate the He⁺ abundance, we use the flux of some of the most intense He I lines: $\lambda\lambda 3188, 3614, 3889, 3965, 4026, 4388, 4438, 4471, 4713, 4922, 5016, 5876, 6678, 7065, 7281$. He I $\lambda\lambda 4121, 5048$ lines were discarded because they are contaminated by ghost lines (see § 4.3.2). The 15 selected lines correspond to both singlet and triplet configurations, as it is shown in Fig. A4. The fluxes of triplet lines are affected by the meta-stability of the 2^3S level. The comparatively much longer lifetime of 2^3S , promotes re-excitations of bounded electrons by self-absorption of line photons, altering the flux ratios predicted by recombination theory for some He I lines. For example, self-absorption of He I $\lambda 3188$ photons can increase the flux of He I $\lambda\lambda 3889, 5876$ and 7065 lines at the expense of He I $\lambda 3188$, which flux decreases accordingly. On the other hand, self-absorption of the He I $\lambda 3889$ line is also important and increase of the flux of He I $\lambda 7065$ at the expense of He I $\lambda 3889$. The effects of self-absorption are stronger as optical depth of the triplet lines related to the 2^3S level increases. However, the sum of the fluxes of He I $\lambda\lambda 3188, 3889, 4713, 5876$, and 7065 lines should remain independent of the optical depth (parameterized by τ_{3889} or τ_{3188} , [Porter et al. 2007](#)).

In Table 11, we show the He⁺ abundances determined using the fluxes of He I $\lambda\lambda 3188, 3889, 4713, 5876$, and 7065 lines and the values of n_e and $T_e(\text{He I})$ corresponding to each component of each cut. In the same table, we also include the He⁺ abundance obtained from the sum of the fluxes of all the individual lines of the table and re-distributing it assuming $\tau_{3188} = \tau_{3889} = 0$. In Table 12 we show

the He⁺ abundances determined from singlet lines and those triplet ones that are expected to be less affected by self-absorption (see Table 2 from [Benjamin et al. 2002](#)). Tables 11 and 12 show a good agreement between the average values of He⁺/H⁺ ratios included in Table 12 (the last row) and those obtained summing the fluxes of lines included in Table 11. This last table also shows that the self-absorption effects are less important in the high velocity gas than in the nebular one. This is noticeable in the larger dispersion of the abundances obtained with each individual line without considering the effects of self-absorption and that obtained redistributing the fluxes as expected at $\tau = 0$ in the nebular components. As it is discussed in [Osterbrock & Ferland \(2006, see their figure 4.5\)](#) if the nebula has ionized zones with different velocities, the self-absorption effects can be reduced due to the Doppler shift between the emitting and absorbing zones. For example, the effect of the self-absorption in the intense He I $\lambda 5876$ line is remarkable in the nebular component, giving He⁺ abundances about 0.05 dex higher than the sum value. In this sense, the common procedure of using a flux-weighted average of He I $\lambda 5876$ and other bright optical He I lines (as $\lambda\lambda 4471$ and 6678) for obtaining the mean He⁺ abundance would provide rather an upper limit of it.

Another interesting fact that can be noted in Table 12 is that the He⁺ abundance determined from the He I $\lambda 5016$ line is lower than that obtained from other lines in the high velocity components. An abnormally low flux of this line was noted by [Esteban et al. \(2004\)](#), and this was attributed to self-absorption effects in the singlet configuration of He I. [Porter et al. \(2007\)](#) discussed this, proposing that the most likely explanation is a deviation from case B of the He I $\lambda\lambda 537.0$ and 522.0 lines, that go to the ground level, partially escaping before being reabsorbed. This is probably the case in the high velocity components where any kind of self-absorption of photons from the “static” nebular gas should be reduced.

5.2.2 O²⁺ abundance

We calculate the O²⁺ abundance using the RLs presented in Table 13, using the n_e determined from O II lines for the nebular components and the adopted density based on [Fe III] lines in the high velocity components, following the results described in § 4.3.1. In all components, the $T_e(\text{high})$ was adopted. The abundance calculation (as well as the n_e estimation) is based on the recombination coefficients calculated by [Storey et al. \(2017\)](#). These coefficients consider the distribution of population among the O²⁺ levels with some improvements over similar estimates from [Bastin & Storey \(2006\)](#). Previous works on recombination coefficients of O II as [Storey \(1994\)](#) assumed that the O²⁺ levels are populated according

Table 9. Comparison of the observed [Ni III] intensity ratios and theoretical ones from Bautista (2001).

Ratio	Esteban et al. (2004)	Mesa-Delgado et al. (2009)	Delgado-Inglada et al. (2016)	This work		
		HH202	Orion Bar	Nebular	HH529II	Predicted
6534/6000	2.09 ± 0.94	1.58 ± 0.38	1.46 ± 0.40	1.54 ± 0.39	3.35 ± 1.40	2.19
6946/6000	-	0.28 ± 0.09	-	0.31 ± 0.11	0.82 ± 0.52	0.39

Table 10. Chemical abundances based on CEL's without considering the temperature fluctuations scenario ($t^2 = 0$).

Ion	Cut 1		Cut 2		Cut 3		Cut 4	Combined cuts
	Nebula	HH529II	Nebula	HH529III	Nebula	Nebula		
O ⁺	7.88 ± 0.04	7.36 ^{+0.12} _{-0.09}	7.83 ^{+0.06} _{-0.05}	7.83 ^{+0.18} _{-0.12}	7.76 ^{+0.07} _{-0.06}	7.81 ^{+0.07} _{-0.06}	7.75 ± 0.05	
O ²⁺	8.32 ± 0.03	8.54 ^{+0.03} _{-0.02}	8.35 ± 0.03	8.51 ± 0.02	8.35 ^{+0.03} _{-0.02}	8.36 ± 0.03	8.37 ± 0.03	
N ⁺	7.00 ± 0.02	6.19 ^{+0.06} _{-0.05}	6.99 ± 0.03	6.61 ^{+0.10} _{-0.07}	6.91 ^{+0.04} _{-0.03}	6.98 ^{+0.04} _{-0.03}	6.89 ± 0.03	
Ne ²⁺	7.67 ± 0.04	7.91 ± 0.03	7.70 ^{+0.04} _{-0.03}	7.82 ^{+0.03} _{-0.02}	7.73 ± 0.03	7.75 ^{+0.04} _{-0.03}	7.73 ^{+0.04} _{-0.03}	
S ⁺	5.58 ± 0.05	4.88 ^{+0.08} _{-0.07}	5.57 ^{+0.05} _{-0.04}	5.41 ^{+0.11} _{-0.09}	5.53 ^{+0.06} _{-0.05}	5.59 ± 0.05	5.49 ± 0.05	
S ²⁺	6.79 ± 0.04	6.92 ^{+0.05} _{-0.04}	6.85 ^{+0.09} _{-0.07}	6.91 ± 0.05	6.86 ^{+0.05} _{-0.04}	6.82 ^{+0.05} _{-0.04}	6.85 ± 0.04	
Cl ⁺	3.72 ± 0.04	2.95 ^{+0.14} _{-0.13}	3.71 ± 0.04	<3.34	3.68 ± 0.04	3.75 ± 0.04	3.63 ± 0.04	
Cl ²⁺	4.88 ^{+0.06} _{-0.05}	5.01 ^{+0.06} _{-0.05}	4.93 ^{+0.06} _{-0.05}	5.09 ^{+0.08} _{-0.06}	4.96 ^{+0.06} _{-0.05}	4.95 ^{+0.06} _{-0.05}	4.94 ^{+0.05} _{-0.04}	
Cl ³⁺	3.28 ± 0.06	3.60 ± 0.05	3.28 ^{+0.04} _{-0.03}	3.41 ± 0.11	3.33 ± 0.04	3.45 ± 0.04	3.38 ± 0.05	
Ar ²⁺	6.31 ± 0.03	6.39 ± 0.02	6.31 ± 0.03	6.37 ± 0.03	6.33 ± 0.02	6.29 ± 0.03	6.32 ± 0.03	
Ar ³⁺	4.39 ^{+0.06} _{-0.05}	4.67 ^{+0.04} _{-0.03}	4.47 ^{+0.04} _{-0.03}	4.52 ± 0.07	4.50 ± 0.04	4.61 ^{+0.04} _{-0.03}	4.52 ^{+0.05} _{-0.04}	
*Fe ²⁺	5.77 ± 0.02	5.94 ± 0.05	5.82 ± 0.02	5.78 ± 0.05	5.78 ± 0.02	5.76 ± 0.03	5.80 ± 0.02	
**Fe ²⁺	5.52 ± 0.03	5.62 ± 0.07	5.57 ± 0.02	5.54 ± 0.06	5.52 ± 0.04	5.48 ± 0.03	5.53 ± 0.04	
Fe ³⁺	5.68 ^{+0.13} _{-0.11}	6.25 ^{+0.10} _{-0.09}	5.70 ^{+0.09} _{-0.08}	<6.58	5.73 ^{+0.11} _{-0.10}	5.73 ^{+0.13} _{-0.12}	5.75 ^{+0.11} _{-0.10}	
Ni ²⁺	4.37 ± 0.14	4.50 ± 0.08	4.33 ± 0.17	4.39 ^{+0.12} _{-0.10}	4.32 ± 0.16	4.36 ± 0.12	4.38 ± 0.10	

* indicates that T_e (high) was used.** indicates that T_e (low) was used.**Table 11.** He⁺/H⁺ abundances determined using He I triplet lines highly affected by self-absorption. The row of “sum” is the result of adding the measured intensity of the triplets presented and redistributing it assuming negligible self-absorption effects ($\tau = 0$).

λ_0 (Å)	Cut 1		Cut 2		Cut 3		Cut 4	Combined Cuts
	Nebula	HH529II	Nebula	HH529III	Nebula	Nebula		
3188	10.67 ± 0.02	10.92 ± 0.02	10.63 ± 0.02	10.97 ± 0.05	10.62 ± 0.02	10.68 ± 0.02	10.71 ± 0.02	
3889	10.60 ± 0.02	10.93 ± 0.02	10.52 ± 0.02	10.75 ± 0.02	10.42 ± 0.02	10.55 ± 0.02	10.61 ± 0.02	
4713	11.01 ± 0.03	11.10 ± 0.03	11.04 ± 0.03	11.02 ^{+0.03} _{-0.04}	11.07 ± 0.02	11.11 ± 0.02	11.07 ± 0.02	
5876	10.96 ± 0.01	10.95 ± 0.01	10.97 ± 0.01	10.92 ± 0.01	10.98 ± 0.01	10.96 ± 0.01	10.97 ± 0.01	
7065	11.34 ± 0.04	11.22 ^{+0.05} _{-0.04}	11.35 ± 0.04	11.18 ± 0.06	11.34 ± 0.04	11.37 ± 0.04	11.34 ± 0.04	
Sum	10.91 ± 0.02	10.97 ± 0.02	10.90 ± 0.02	10.93 ± 0.03	10.89 ± 0.02	10.90 ± 0.02	10.91 ± 0.02	

to their statistical weight, which is not suitable for densities below the critical one.

In Table 13, we present the weighted average abundance for each multiplet. In the last row of Table 13 we give the final O²⁺ abundance obtained averaging the values obtained for multiplets 1, 2, 10, 20 and 3d – 4f transitions. These multiplets and transitions give consistent values and were also considered by Esteban et al. (2004) for determining their mean values. However, we decided to consider only the abundance obtained from multiplet 1 as representative of the O²⁺ abundance. This is because, although it gives values consistent with the average of the other aforementioned multiplets and transitions, the inclusion of the results for several multiplets with fainter lines increases the formal uncertainties of the final mean O²⁺ abundance.

5.2.3 Determination of the abundance of other heavy elements based on RLs.

Due to the high quality of our deep spectra, we were able to determine abundances of other heavy element ions such as O⁺, C²⁺ and Ne²⁺ based on the fluxes of RLs and the recombination coefficients presented in Table 5.

O⁺ abundances were obtained from the lines of multiplet 1 of O I $\lambda\lambda 7771.94, 7774.17$ and 7775.39 together with the adopted density and temperature of the low ionization zone for each component of each cut. Due to the high spectral resolution of our data, these O I lines are not blended with telluric emission features as it is shown in Fig 11. We do not detect the lines of multiplet 1 of O I in the high velocity components. In these cases, we have estimated upper limits of their intensity and corresponding abundances considering an hypothetical line with a flux of 3σ of the rms of the adjacent

Table 12. He⁺/H⁺ abundances determined with He I singlet lines and triplet lines relatively free of self-absorption effects.

λ_0 (Å)	Cut 1		Cut 2		Cut 3		Cut 4		Combined Cuts
	Nebula	HH529II	Nebula	HH529III	Nebula	HH529III	Nebula	HH529III	
3614	10.93 ± 0.02	10.85 ± 0.04	10.89 ± 0.02	11.09 ± 0.05	10.86 ± 0.02	10.85 ± 0.02	10.89 ± 0.02	10.89 ± 0.02	
3965	10.88 ± 0.01	10.86 ± 0.02	10.89 ± 0.01	10.93 ± 0.02	10.87 ± 0.01	10.88 ± 0.01	10.89 ± 0.01	10.89 ± 0.01	
4026	10.89 ± 0.01	10.97 ± 0.01	10.90 ± 0.01	11.00 ± 0.01	10.93 ± 0.01	10.93 ± 0.01	10.93 ± 0.01	10.93 ± 0.01	
4388	10.90 ± 0.01	10.96 ± 0.01	10.92 ± 0.01	10.97 ± 0.01	10.91 ± 0.01	10.91 ± 0.01	10.91 ± 0.01	10.92 ± 0.01	
4438	10.95 ± 0.03	10.88 ± 0.04	10.92 ± 0.02	11.08 ± 0.07	10.92 ± 0.02	10.91 ± 0.03	10.94 ± 0.03	10.94 ± 0.03	
4471	10.87 ± 0.01	10.96 ± 0.01	10.90 ± 0.01	10.93 ± 0.01	10.91 ± 0.01	10.93 ± 0.01	10.91 ± 0.01	10.91 ± 0.01	
4922	10.90 ± 0.01	10.94 ± 0.01	10.92 ± 0.01	10.94 ± 0.01	10.92 ± 0.01	10.92 ± 0.01	10.92 ± 0.01	10.92 ± 0.01	
5016	10.87 ± 0.01	10.78 ± 0.02	10.88 ± 0.01	10.84 ± 0.02	10.88 ± 0.01	10.88 ± 0.01	10.87 ± 0.01	10.87 ± 0.01	
6678	10.90 ± 0.02	10.94 ± 0.02	10.91 ± 0.01	10.93 ± 0.02	10.92 ± 0.02	10.90 ± 0.01	10.92 ± 0.02	10.92 ± 0.02	
7281	10.90 ± 0.03	10.95 ± 0.03	10.92 ± 0.03	10.93 ± 0.04	10.92 ± 0.03	10.91 ± 0.03	10.93 ± 0.03	10.93 ± 0.03	
Average	10.89 ± 0.02	10.95 ± 0.03	10.90 ± 0.01	10.95 ± 0.03	10.90 ± 0.02	10.90 ± 0.02	10.91 ± 0.02	10.91 ± 0.02	

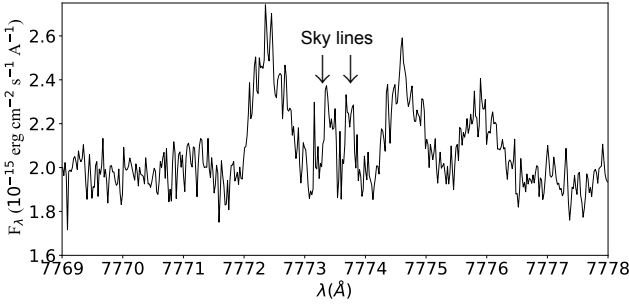


Figure 11. Lines of multiplet 1 of OI ($3s^5S^0$ - $3p^5P$) in the spatial cut 2. No emission from HH529II is observed, only the nebular component is noticeable. These lines are produced from transitions of quintet levels (Grandi 1975a) and arise purely by recombination. Due to high spectral resolution and the earth motion during the observations, these lines are free of blending with sky lines.

continuum. The resulting O⁺ abundances and the estimated upper limits for the high-velocity components are shown in Table 14.

For C²⁺ and Ne²⁺, we adopt the temperature of the high ionization zone for each component of each cut. C II RLs from different transitions were considered to derive C²⁺ abundances, as it is shown in Table 14. Multiplet 6 of C II present two lines at 4267.00 and 4267.18+4267.26 Å resolved at our spectral resolution, as shown in Fig. 12. In general, lines from all multiplets of C II considered give consistent values of C²⁺ abundances. RLs from multiplet 1 of Ne II were used to calculate the Ne²⁺ abundance. Although they are rather faint lines (see Fig. 13), the Ne²⁺ abundances derived from Ne II $\lambda\lambda$ 3694.21 and 3766.26 lines for each component of cut 2 are consistent with each other. In addition, the Ne²⁺ abundance we derive for the nebular component in cuts 2 and 3 is in good agreement with that obtained by Esteban et al. (2004) (see their Table 11).

6 TEMPERATURE FLUCTUATIONS

Following the procedure described by Peimbert (1967), we define the average temperature as it is shown in Eq. (7) and the mean square temperature fluctuation as in Eq. (8).

$$T_0 = \frac{\int T_e n_e n_i dV}{\int n_e n_i dV}, \quad (7)$$

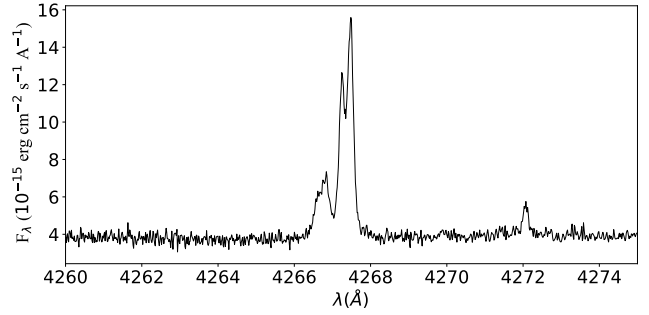


Figure 12. Lines of multiplet 6 of C II ($3d^2D$ - $4f^2F^0$) in the spatial cut 2. Due to our high spectral resolution, we can partially separate $\lambda 4267.00$ from $\lambda 4267.18 + \lambda 4267.26$ both in the component corresponding to HH529II and to the nebular one.

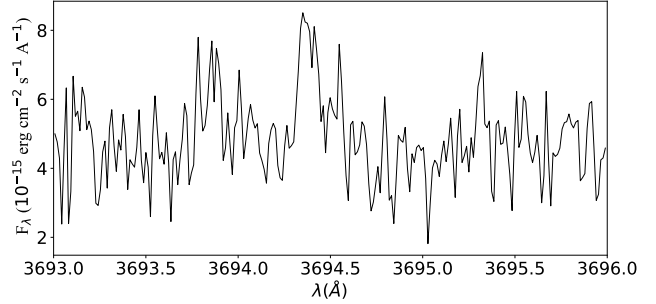


Figure 13. Lines of multiplet 1 of Ne II ($3s^4P$ - $3p^4P^0$) in the spatial cut 2.

$$t^2 = \frac{\int (T_e - T_0)^2 n_e n_i dV}{T_0 \int n_e n_i dV}. \quad (8)$$

In the case of a temperature derived from the ratio of two quantities that depend on two different powers of temperature, α and β respectively, as the case of the temperature derived from RLs or the ratio between the Balmer or Paschen discontinuities and the flux of any other H I line, the measured temperature $T_{\alpha/\beta}$ depends on t^2 and T_0 as follows:

$$T_{\alpha/\beta} = T_0 \left(1 - \frac{\alpha + \beta - 1}{2} t^2 \right). \quad (9)$$

Table 13: O²⁺ abundances based on RLs.

Mult.	Transition	λ_0	Cut 1	Cut 2	Cut 3	Cut 4	Combined Cuts		
			Nebula	HH529II	Nebula	HH529III			
1	$3s^4P-3p^4D^0$	4638.86	8.547 ± 0.038	8.938 ± 0.027	8.546 ± 0.019	$8.757^{+0.107}_{-0.109}$	8.566 ± 0.067	$8.519^{+0.031}_{-0.032}$	8.632 ± 0.044
		4641.81	$8.433^{+0.017}_{-0.018}$	$8.809^{+0.017}_{-0.018}$	$8.516^{+0.014}_{-0.013}$	$8.828^{+0.027}_{-0.025}$	$8.502^{+0.014}_{-0.013}$	$8.509^{+0.017}_{-0.018}$	$8.575^{+0.017}_{-0.018}$
		4649.13	$8.473^{+0.024}_{-0.022}$	8.793 ± 0.014	8.520 ± 0.011	$8.779^{+0.025}_{-0.026}$	8.536 ± 0.015	$8.534^{+0.018}_{-0.016}$	$8.589^{+0.016}_{-0.015}$
		4650.84	$8.469^{+0.032}_{-0.031}$	8.912 ± 0.027	8.509 ± 0.019	$9.022^{+0.042}_{-0.043}$	8.521 ± 0.023	$8.558^{+0.029}_{-0.028}$	8.602 ± 0.028
		4661.63	$8.534:$	$9.021^{+0.027}_{-0.026}$	$8.550:$	$8.981^{+0.031}_{-0.030}$	$8.602:$	$8.609:$	$8.672:$
		4673.73	$8.579^{+0.152}_{-0.149}$	9.041 ± 0.120	$8.478^{+0.070}_{-0.069}$	$8.965:$	$8.790^{+0.062}_{-0.060}$	$8.749^{+0.088}_{-0.087}$	$8.730^{+0.099}_{-0.095}$
		4676.23	$8.400^{+0.052}_{-0.053}$	$8.748^{+0.047}_{-0.049}$	8.475 ± 0.022	$8.936^{+0.069}_{-0.068}$	8.497 ± 0.026	$8.507^{+0.031}_{-0.030}$	$8.543^{+0.034}_{-0.035}$
		Average	8.465 ± 0.043	8.830 ± 0.073	8.515 ± 0.018	8.844 ± 0.088	8.517 ± 0.033	8.525 ± 0.026	8.584 ± 0.022
		4317.14	$8.498^{+0.052}_{-0.054}$	$9.099^{+0.030}_{-0.031}$	8.671 ± 0.022	-	$8.644^{+0.047}_{-0.048}$	8.656 ± 0.035	$8.723:$
		4345.56	8.582 ± 0.057	$9.194^{+0.043}_{-0.044}$	8.714 ± 0.026	9.147 ± 0.072	8.659 ± 0.031	8.726 ± 0.030	$8.829^{+0.043}_{-0.044}$
2	$3s^4P-3p^4P^0$	4349.43	8.659 ± 0.040	$9.015^{+0.022}_{-0.021}$	8.678 ± 0.013	$8.995^{+0.051}_{-0.052}$	$8.650^{+0.021}_{-0.022}$	$8.715^{+0.026}_{-0.025}$	8.767 ± 0.030
		4366.89	$8.631^{+0.041}_{-0.040}$	$9.237^{+0.026}_{-0.025}$	8.710 ± 0.022	9.208 ± 0.056	$8.672^{+0.030}_{-0.031}$	$8.724^{+0.031}_{-0.030}$	8.835 ± 0.030
		Average	8.595 ± 0.062	9.085 ± 0.091	8.686 ± 0.016	9.073 ± 0.097	8.656 ± 0.009	8.706 ± 0.027	8.802 ± 0.033
		4414.90	$8.807^{+0.053}_{-0.051}$	$8.939^{+0.046}_{-0.047}$	8.754 ± 0.025	-	$8.772^{+0.026}_{-0.027}$	$8.689^{+0.053}_{-0.052}$	$8.753^{+0.036}_{-0.035}$
5	$3s^2P-3p^2D^0$	4416.97	$8.622^{+0.069}_{-0.063}$	-	$8.769^{+0.031}_{-0.030}$	-	8.734 ± 0.039	$8.712^{+0.043}_{-0.044}$	$8.680^{+0.036}_{-0.034}$
		Average	8.710 ± 0.093	$8.939^{+0.046}_{-0.047}$	8.760 ± 0.007	-	8.759 ± 0.018	8.702 ± 0.011	8.712 ± 0.037
		4069.62	$8.459^{+0.064}_{-0.060}$	-	$8.246:$	-	$8.352:$	$8.657^{+0.071}_{-0.069}$	$8.299:$
10	$3p^4D^0-3d^4F$	4069.88	$8.352^{+0.050}_{-0.049}$	$8.431:$	$8.297:$	$8.348:$	$8.386:$	$8.412^{+0.096}_{-0.091}$	$8.353:$
		4072.15	8.449 ± 0.026	$8.608^{+0.035}_{-0.034}$	$8.421^{+0.017}_{-0.018}$	$8.761^{+0.066}_{-0.067}$	$8.423^{+0.021}_{-0.022}$	$8.372^{+0.027}_{-0.026}$	8.467 ± 0.026
		4075.86	$8.436:$	$8.757:$	-	-	-	$8.407^{+0.030}_{-0.029}$	-
		4078.84	$8.299^{+0.166}_{-0.159}$	$8.998^{+0.093}_{-0.092}$	$8.503^{+0.040}_{-0.039}$	-	$8.787:$	-	-
		4085.11	8.212 ± 0.150	$9.385:$	8.509 ± 0.035	$9.393:$	8.408 ± 0.065	$8.699^{+0.044}_{-0.043}$	$8.810:$
		4092.93	-	$8.550:$	$8.598^{+0.049}_{-0.047}$	$8.579:$	$8.453^{+0.073}_{-0.071}$	$8.627:$	$9.013:$
		Average	8.421 ± 0.048	8.623 ± 0.093	8.450 ± 0.052	$8.761^{+0.066}_{-0.067}$	8.423 ± 0.009	8.413 ± 0.099	8.467 ± 0.026
		4590.97	$8.414^{+0.062}_{-0.060}$	$8.595^{+0.062}_{-0.061}$	$8.385^{+0.034}_{-0.033}$	$8.674^{+0.073}_{-0.072}$	8.387 ± 0.031	8.415 ± 0.057	$8.433^{+0.045}_{-0.043}$
15	$3s^2D-3p^2F^0$	4121.46	$8.791:$	-	8.865 ± 0.030	-	$8.806:$	$8.862:$	$8.762:$
		4132.80	$8.451^{+0.069}_{-0.071}$	9.029 ± 0.056	$8.565^{+0.027}_{-0.026}$	$9.031^{+0.150}_{-0.147}$	8.512 ± 0.035	8.579 ± 0.044	$8.651^{+0.053}_{-0.051}$
		4153.30	$8.622^{+0.038}_{-0.037}$	9.059 ± 0.031	8.605 ± 0.019	$8.983^{+0.052}_{-0.051}$	$8.603^{+0.023}_{-0.024}$	8.623 ± 0.037	8.725 ± 0.032
20	$3p^4P^0-3d^4D$	Average	8.565 ± 0.079	9.051 ± 0.013	8.616 ± 0.093	8.988 ± 0.014	8.568 ± 0.044	8.603 ± 0.022	8.701 ± 0.034
		4104.99	-	$8.761:$	$8.363^{+0.126}_{-0.123}$	-	$8.458^{+0.102}_{-0.098}$	8.494 ± 0.097	-
36	$3p^2F^0-3d^2G$	4110.79	$8.811:$	$9.584:$	$8.805:$	$9.167:$	$8.766:$	$9.250:$	$9.030:$
		4119.22	$8.563^{+0.049}_{-0.048}$	$8.842^{+0.061}_{-0.059}$	$8.626^{+0.023}_{-0.022}$	-	$8.475^{+0.072}_{-0.074}$	$8.722^{+0.036}_{-0.034}$	$8.605^{+0.044}_{-0.043}$
		Average	$8.563^{+0.049}_{-0.048}$	$8.842^{+0.061}_{-0.059}$	8.626 ± 0.087	$9.167:$	8.469 ± 0.008	8.674 ± 0.087	$8.605^{+0.044}_{-0.043}$
		4185.44	$8.095^{+0.062}_{-0.061}$	8.034 ± 0.112	$7.971^{+0.045}_{-0.043}$	$8.437:$	$8.079^{+0.065}_{-0.066}$	$8.108^{+0.071}_{-0.070}$	$8.074^{+0.092}_{-0.088}$
		4189.79	$8.344^{+0.047}_{-0.044}$	8.638 ± 0.048	$8.307^{+0.031}_{-0.029}$	$8.810^{+0.122}_{-0.120}$	$8.329^{+0.071}_{-0.070}$	$8.380^{+0.055}_{-0.052}$	$8.418^{+0.062}_{-0.063}$
3d-4f	$3d^4F-4fG^2[3]^0$	Average	8.200 ± 0.128	8.279 ± 0.323	8.107 ± 0.172	$8.810^{+0.122}_{-0.120}$	8.146 ± 0.119	8.217 ± 0.138	8.211 ± 0.176
		4087.15	8.588 ± 0.092	$8.868^{+0.117}_{-0.119}$	$8.644^{+0.065}_{-0.067}$	$9.152^{+0.094}_{-0.095}$	$8.431^{+0.057}_{-0.056}$	$8.526^{+0.096}_{-0.095}$	8.651 ± 0.082
		4089.29	$8.451^{+0.058}_{-0.057}$	$8.939:$	$8.518^{+0.032}_{-0.030}$	$8.744:$	$8.422^{+0.028}_{-0.027}$	$8.412^{+0.051}_{-0.048}$	8.555 ± 0.036
		4095.64	-	8.824 ± 0.100	$8.499^{+0.054}_{-0.053}$	$9.396:$	$8.545:$	-	-
		$3d^4F-4fG^2[4]^0$	4097.26	$8.547^{+0.059}_{-0.056}$	$8.551^{+0.029}_{-0.028}$	-	8.577 ± 0.031	$8.592^{+0.039}_{-0.040}$	$8.497^{+0.036}_{-0.035}$
		$3d^4D-4fF^2[4]^0$	4275.55	$8.464^{+0.070}_{-0.068}$	$8.680^{+0.106}_{-0.110}$	$8.520^{+0.046}_{-0.047}$	-	$8.475^{+0.053}_{-0.052}$	$8.554^{+0.063}_{-0.060}$
		Average	8.494 ± 0.052	8.767 ± 0.082	8.534 ± 0.032	$9.152^{+0.094}_{-0.095}$	8.468 ± 0.067	8.507 ± 0.081	8.525 ± 0.041
Mult. 1, 2, 10, 20 and 3d-4f transitions		Average	8.465 ± 0.072	8.838 ± 0.143	8.539 ± 0.084	8.858 ± 0.117	8.512 ± 0.075	8.523 ± 0.108	8.541 ± 0.137

Table 14. O⁺, C²⁺ and Ne²⁺ abundances based on RLs.

Mult.	Transition	λ_0	Cut 1 Nebula	Cut 2 HH529II	O ⁺ Nebula	Cut 3 HH529III	Nebula	Cut 4 Nebula	Combined Cuts
1	3s ⁵ S ⁰ -3p ⁵ P	7771.94							
		7774.17	8.344 ± 0.100	<7.91	8.250 ± 0.064	<7.95	8.275 ± 0.073	8.274 ^{+0.068} _{-0.069}	8.187 ± 0.073
		7775.39							
6	3d ² D-4f ² F ⁰	4267.00							
		4267.18	8.349 ^{+0.030} _{-0.031}	8.457 ± 0.017	8.347 ± 0.017	8.557 ± 0.026	8.339 ± 0.013	8.328 ^{+0.021} _{-0.022}	8.371 ± 0.026
		4267.26							
16.04	4d ² D-6f ² F ⁰	6151.27							
		6151.53	-	9.054:	8.376:	-	8.441 ± 0.120	-	-
17.02	4f ² F ⁰ -5g ² G	9903.46							
		9903.89	8.326 ^{+0.043} _{-0.045}	8.465 ^{+0.066} _{-0.063}	8.363 ± 0.035	8.622 ^{+0.138} _{-0.136}	8.301 ^{+0.057} _{-0.056}	8.353 ^{+0.043} _{-0.042}	8.377 ^{+0.057} _{-0.056}
17.04	4f ² F ⁰ -6g ² G	6461.95							
		6462.13	8.354 ± 0.091	8.704:	8.298 ± 0.065	-	8.318 ± 0.060	8.351 ± 0.071	8.353 ^{+0.118} _{-0.116}
17.06	4f ² F ⁰ -7g ² G	5342.38							
		5342.50	8.619:	-	8.449 ^{+0.059} _{-0.060}	-	8.502 ^{+0.064} _{-0.065}	-	-
		Adopted	8.342 ± 0.030	8.458 ± 0.021	8.351 ± 0.025	8.560 ± 0.026	8.340 ± 0.029	8.334 ± 0.022	8.371 ± 0.026
1	3s ⁴ P-3p ⁴ P ⁰	3694.21	-	8.643 ^{+0.072} _{-0.073}	8.095 ^{+0.063} _{-0.065}	-	8.315:	-	-
		3766.26	-	8.515 ^{+0.137} _{-0.135}	8.034 ^{+0.089} _{-0.092}	-	8.036 ^{+0.153} _{-0.150}	-	-
		Adopted	-	8.603 ± 0.057	8.072 ± 0.029	-	8.036 ± 0.150	-	-

On the other hand, two quantities with an individual temperature dependence proportional to $\frac{e^{\frac{\Delta E}{kT}}}{T^{1/2}}$, as the intensity of CELs, will produce a line intensity ratio with a temperature dependence on $e^{\frac{\Delta E_2 - \Delta E_1}{kT\lambda_1/\lambda_2}}$. We can derive the temperature T_{λ_1/λ_2} :

$$T_{\lambda_1/\lambda_2} = T_0 \left[1 + \left(\frac{\Delta E_1 + \Delta E_2}{kT_0} - 3 \right) \frac{t^2}{2} \right] \quad (10)$$

When α and β in Eq. (9) are negative, the low-temperature zones within the line of sight will have a larger weight on $T_{\alpha/\beta}$, while in the cases where $\frac{\Delta E_1 + \Delta E_2}{kT_0}$ is larger than 3, the contribution of the high-temperature zones will be more important (Peimbert 1967).

On the basis of Eq. (9) and the estimations of the α and β coefficients given by Peimbert & Costero (1969) and Zhang et al. (2005), for the H I and He I temperature, respectively, we have Eq. (11) and Eq. (12).

$$T_e(\text{H I})_{\text{BJ-PJ}} = T_0 \left(1 - 1.67t^2 \right), \quad (11)$$

$$T_e(\text{He I})_{7281/6678} = T_0 \left(1 - 1.07t^2 \right). \quad (12)$$

On the other hand, for estimations of temperatures based on intensity ratios of CELs, we have Eq. (13), Eq. (14) and Eq. (15).

$$T_e(\text{[O III]})_{4363/4959+5007} = T_0 \left[1 + \left(\frac{91300}{T_0} - 3 \right) \frac{t^2}{2} \right], \quad (13)$$

$$T_e(\text{[S III]})_{6312/9069+9531} = T_0 \left[1 + \left(\frac{54000}{T_0} - 3 \right) \frac{t^2}{2} \right], \quad (14)$$

$$T_e(\text{[N II]})_{5755/6584} = T_0 \left[1 + \left(\frac{68950}{T_0} - 3 \right) \frac{t^2}{2} \right]. \quad (15)$$

We have applied the combination of Eq. (11) and Eq. (13) using $T_e(\text{H I})$ and $T_e(\text{[O III]})$ to estimate t^2 (Peimbert 2003; Esteban et al. 2004; García-Rojas et al. 2004, 2005, 2007). Implicitly, this assumes that $t^2(\text{H}^+) \approx t^2(\text{O}^{2+})$ and $T_0(\text{H}^+) \approx T_0(\text{O}^{2+})$. The same procedure has been used with Eq. (14) and Eq. (15) (Peimbert & Costero 1969; Esteban et al. 1998) in order to estimate representative values of t^2 for different ionization zones. In Table (15), we show the t^2 and T_0 values obtained for each combination of the temperature indicators in the spectrum of the combined cuts, the only one where all the different temperature indicators are available. We have to emphasize the excellent agreement between the results obtained by combining $T_e(\text{H I})$ and the T_e diagnostics based on CELs ratios with what it is obtained using $T_e(\text{He I})$.

However, the above procedure may not be entirely accurate. From equations (7) and (8), it is clear that the values of t^2 and T_0 depend on the integrated volume. Thus, since each ion X^{i+} will have its own Strömgren sphere, each one will have a representative $t^2(X^{i+})$ and $T_0(X^{i+})$. Considering another ion, Y^{i+} , the assumption $t^2(X^{i+}) \approx t^2(Y^{i+})$ will be only correct if X^{i+} and Y^{i+} occupy the same nebular volume. In the case of H^+ and O^{2+} , if there is an appreciable amount of O in other states apart of O^{2+} , the value of $t^2(\text{H}^+)$ may differ from $t^2(\text{O}^{2+})$. Based on a set of Cloudy photoionization models with different input parameters, Kingdon & Ferland (1995) derived t^2 in two manners: as t_{str}^2 from the formal definition of Eq. (8) and the t_{obs}^2 obtained from the comparison of equations (11) and (13). They found that generally $t_{\text{str}}^2 \neq t_{\text{obs}}^2$, with the difference increasing with the T_{eff} of the ionizing sources. However, for the T_{eff} typical of the ionizing stars of H II regions (between 30,000 and 50,000 k), the approximation $t_{\text{str}}^2 \approx t_{\text{obs}}^2$ seems to be valid. The main drawback one faces in determining t_{obs}^2 is its high intrinsic uncertainty. As we mentioned in § 4.4, the determination of temperature based on the Balmer or Paschen discontinuities is very sensitive to

Table 15. t^2 and T_0 derived from the different combinations of Eq. (11) and Eq. (12) with Eq. (13), Eq. (14) and Eq. (15) for the spectra of all cuts combined.

	$T_e(\text{[O III]})$		$T_e(\text{[S III]})$		$T_e(\text{[N II]})$	
	t^2	T_0	t^2	T_0	t^2	T_0
$T_e(\text{H I})_{\text{BJ}}$	0.020 ± 0.017	7770 ± 850	0.051 ± 0.030	8240 ± 980	0.068 ± 0.023	8510 ± 960
$T_e(\text{H I})_{\text{PJ}}$	0.019 ± 0.025	7800 ± 1260	0.050 ± 0.042	8250 ± 1420	0.068 ± 0.033	8530 ± 1430
$T_e(\text{He I})$	0.018 ± 0.012	7840 ± 520	0.054 ± 0.024	8160 ± 570	0.075 ± 0.018	8360 ± 570

the noise level of the nebular continuum around the position of the discontinuities. The sources of uncertainty in $T_e(\text{He I})$ are slightly smaller, but they are still important. Assuming the two ionization zones scheme for H II regions, a better approximation to t^2 can be obtained using equations (16) and (17), proposed by Peimbert et al. (2002).

$$\gamma = \frac{\int n_e(\text{O}^+) dV}{\int n_e n(\text{O}^+) dV + \int n_e n(\text{O}^{2+}) dV}, \quad (16)$$

$$T_0(\text{H}^+) = \gamma T_0(\text{O}^+) + (1 - \gamma) T_0(\text{O}^{2+}). \quad (17)$$

To use Eq. (17), we need to estimate the fraction of the total O in O^+ form. For the spectrum of the combined cuts, γ varies from 0.36 to 0.23 according to whether the abundances are determined from RLs or CELs, respectively. A reasonable approximation is to take the average value $\gamma \approx 0.3$. On the other hand, He^+ should be present in both, the O^+ and O^{2+} zones. Although there may be coexistence of He^0 and H^+ , the volume that He^0 occupies should be small at the ionization conditions of the Orion Nebula and it can be assumed that the volume containing H^+ and He^+ should be approximately the same. This assumption is reinforced by the fact that the parameter $\eta = (\text{O}^+/\text{O}^{2+})(\text{S}^{2+}/\text{S}^+)$ (Vilchez & Pagel 1988), which is a measure of the radiation hardness and is correlated with the T_{eff} of the ionizing source, has a value of $\log(\eta) = 0.74$ for the “combined cuts” spectrum. Pagel et al. (1992) showed that for $\log(\eta) < 0.9$, the amount of He^0 is negligible for a large variety of photoionization models. Therefore, we can assume $T_0(\text{H}^+) \approx T_0(\text{He}^+)$ and $t^2(\text{H}^+) \approx t^2(\text{He}^+)$. Based on the previous discussion, we use Eq. (11) and Eq. (12) for the “combined cuts” spectrum, obtaining $t^2(\text{H}^+) \approx 0.036$ and $T_0(\text{H}^+) \approx 8000$ K. Using these values in Eq. (17) and assuming that the volume occupied by O^+ and N^+ is the same, and that at first order, $\frac{T_e(\text{[O III]})}{T_e(\text{[N II]})} \approx \frac{T_0(\text{O}^{2+})}{T_0(\text{N}^+)} \approx 0.85$, we obtain $T_0(\text{O}^{2+}) \approx 7580$ and $T_0(\text{N}^+) \approx 8950$. Then, from Eq. (13) and Eq. (15), we estimate $t_{\text{high}}^2 = t^2(\text{O}^{2+}) \approx 0.025$ and $t_{\text{low}}^2 = t^2(\text{N}^+) \approx 0.050$.

The remarkably good agreement between the values obtained with Eq. (17) and those presented in Table 15 reinforces the suitability of the temperature fluctuations paradigm to describe the results in the “combined cuts” spectrum. Considering the numerical values obtained for the “combined cuts” spectrum, we adopt the average values $t_{\text{high}}^2 = 0.021 \pm 0.003$, $t_{\text{inter}}^2 = 0.051 \pm 0.009$ and $t_{\text{low}}^2 = 0.064 \pm 0.011$, where the uncertainties correspond to the standard deviation of the average. Unfortunately, $T_e(\text{H I})$ based on the Balmer and Paschen discontinuities can not be calculated for the individual components of the different cuts, and the estimations of t^2 must rely exclusively on the calculated $T_e(\text{He I})$. However, calculations following the same procedure as the previously described

to obtain the values presented in Table 15 for the individual components of each cut show similar results. These values are presented in Table A6, indicating that the values adopted for the “combined cuts” spectrum may be also representative for the other components of each cut.

Using Eq. (15), Eq. (14) and Eq. (13) with the adopted t^2 values for each ionization zone, T_0 is estimated in each case for all components. Following the same scheme described in § 5.1, we estimate the ionic abundances within the the paradigm of temperature inhomogeneities and results are shown in Table 16.

7 THE ABUNDANCE DISCREPANCY FACTOR

A major problem in the analysis of photoionized regions is the discrepancy between the chemical abundances derived from RLs and CELs, known as the Abundance Discrepancy (AD) problem. The relatively weak RLs, give systematically higher abundances than CELs. This difference is commonly quantified through the abundance discrepancy factor (ADF, Liu et al. 2000), defined here as:

$$\text{ADF}\left(X^i\right) = \log\left(\frac{n(X^i)_{\text{RLs}}}{n(X^i)_{\text{CEls}}}\right). \quad (18)$$

There is an extensive collection of works dedicated to this problem in the literature (see Torres-Peimbert et al. 1980; Liu et al. 2001; Stasińska et al. 2007; Tsamis et al. 2011; Nicholls et al. 2012, and references therein). Although there is no definitive solution, there are several hypotheses to explain the AD. For example, temperature fluctuations (see § 6), which would primarily affect abundances based on CELs, underestimating the real values; semi-ionized gas clumps, overestimating abundances based on RLs and underestimating those of CELs; chemical inhomogeneities with different physical conditions, affecting both estimates depending on each specific case and so on. It is even possible that the AD is the result of the sum of various phenomena affecting each nebula in a different degree. Using a set of deep spectra of Galactic H II regions, García-Rojas & Esteban (2007) found that the ADF is fairly constant around a factor 2, showing no trend with ionization degree, T_e or the effective temperature of the ionizing stars. They found that temperature fluctuations is the most likely explanation for the AD in H II regions.

In Table 17, we present the ADF obtained from O^+ , O^{2+} , Ne^{2+} and C^{2+} abundances determined from RLs and CELs for each component. The abundances based on CELs do not consider temperature fluctuations. In the case of C^{2+} , the value of the abundance from CELs have been taken from the UV observations reported by Walter et al. (1992). We have considered the mean value of their positions number 5 and 7, which are the nearest to our slit and give $12 + \log(\text{C}^{2+}/\text{H}^+) = 7.835$. We do not estimate the $\text{ADF}(\text{C}^{2+})$ for the high-velocity component since the UV CELs values can only

Table 16. Chemical abundances based on CEL's derived within the paradigm of temperature inhomogeneities ($t^2 > 0$).

Ion	Cut 1		Cut 2		Cut 3		Cut 4	Combined cuts
	Nebula	HH529II	Nebula	HH529III	Nebula	Nebula	Nebula	
O ⁺	8.18 ^{+0.10} _{-0.08}	7.65 ^{+0.20} _{-0.12}	8.14 ^{+0.12} _{-0.09}	8.14 ^{+0.29} _{-0.16}	8.05 ^{+0.13} _{-0.09}	8.12 ^{+0.13} _{-0.09}	8.05 ^{+0.11} _{-0.08}	
O ²⁺	8.48 ^{+0.06} _{-0.05}	8.72 ^{+0.04} _{-0.03}	8.50 ^{+0.05} _{-0.04}	8.67 ± 0.04	8.51 ± 0.04	8.52 ^{+0.05} _{-0.04}	8.53 ^{+0.05} _{-0.04}	
N ⁺	7.18 ^{+0.05} _{-0.04}	6.36 ^{+0.11} _{-0.08}	7.17 ^{+0.07} _{-0.05}	6.80 ^{+0.15} _{-0.10}	7.09 ^{+0.07} _{-0.05}	7.16 ^{+0.07} _{-0.06}	7.07 ^{+0.06} _{-0.05}	
Ne ²⁺	7.86 ^{+0.07} _{-0.06}	8.12 ± 0.04	7.89 ^{+0.06} _{-0.05}	8.02 ^{+0.05} _{-0.04}	7.91 ^{+0.05} _{-0.04}	7.94 ^{+0.06} _{-0.05}	7.93 ^{+0.06} _{-0.05}	
S ⁺	5.75 ^{+0.07} _{-0.06}	5.04 ^{+0.12} _{-0.08}	5.75 ^{+0.07} _{-0.06}	5.58 ^{+0.16} _{-0.11}	5.70 ^{+0.08} _{-0.07}	5.77 ^{+0.08} _{-0.06}	5.66 ^{+0.07} _{-0.06}	
S ²⁺	6.87 ^{+0.05} _{-0.04}	7.01 ^{+0.06} _{-0.05}	6.94 ^{+0.06} _{-0.05}	6.99 ^{+0.07} _{-0.06}	6.95 ^{+0.06} _{-0.05}	6.91 ± 0.05	6.94 ± 0.05	
Cl ⁺	3.87 ± 0.05	3.09 ^{+0.16} _{-0.14}	3.86 ^{+0.06} _{-0.05}	<3.49	3.81 ^{+0.06} _{-0.05}	3.90 ^{+0.07} _{-0.06}	3.76 ^{+0.06} _{-0.05}	
Cl ²⁺	5.00 ^{+0.07} _{-0.06}	5.15 ^{+0.09} _{-0.07}	5.06 ^{+0.08} _{-0.06}	5.22 ^{+0.10} _{-0.08}	5.09 ^{+0.08} _{-0.06}	5.08 ^{+0.08} _{-0.06}	5.07 ^{+0.07} _{-0.06}	
Cl ³⁺	3.30 ± 0.06	3.71 ± 0.05	3.38 ± 0.04	3.51 ^{+0.10} _{-0.11}	3.43 ± 0.04	3.55 ^{+0.05} _{-0.04}	3.48 ^{+0.06} _{-0.05}	
Ar ²⁺	6.42 ± 0.04	6.51 ± 0.03	6.42 ^{+0.04} _{-0.03}	6.48 ^{+0.04} _{-0.03}	6.43 ± 0.03	6.40 ^{+0.04} _{-0.03}	6.43 ^{+0.04} _{-0.03}	
Ar ³⁺	4.55 ^{+0.07} _{-0.06}	4.84 ^{+0.05} _{-0.04}	4.63 ^{+0.06} _{-0.05}	4.68 ^{+0.08} _{-0.07}	4.66 ^{+0.05} _{-0.04}	4.79 ^{+0.06} _{-0.05}	4.69 ^{+0.06} _{-0.05}	
Fe ^{2+*}	5.93 ± 0.02	6.11 ± 0.05	5.97 ± 0.02	5.94 ± 0.05	5.94 ± 0.02	5.92 ± 0.03	5.96 ± 0.01	
Fe ^{2+**}	5.75 ± 0.02	5.84 ± 0.06	5.81 ± 0.02	5.77 ± 0.06	5.75 ± 0.02	5.72 ± 0.03	5.76 ± 0.02	
Fe ³⁺	5.99 ^{+0.16} _{-0.12}	6.59 ^{+0.12} _{-0.10}	6.00 ^{+0.12} _{-0.09}	<6.68	6.23 ^{+0.18} _{-0.16}	6.05 ^{+0.16} _{-0.13}	6.16 ^{+0.18} _{-0.15}	
Ni ²⁺	4.52 ± 0.19	4.68 ± 0.09	4.51 ± 0.18	4.57 ^{+0.18} _{-0.12}	4.48 ± 0.16	4.51 ± 0.13	4.54 ± 0.11	

* indicates that T_e (high) was used.

** indicates that T_e (low) was used.

be compared with the nebular component. It is a common procedure to estimate t^2 by looking for a temperature T_0 that produces the agreement between the abundance determined from CELs and RLs. We remark that we do not use this procedure in this work. Our determinations of t^2 are exclusively those described in § 6. Therefore $t^2 > 0$, does not necessarily mean ADF = 0, unless the measured value of t^2 , based on different temperature diagnostics, is compatible with this.

From Table 17, is remarkable that the ADF is slightly different for each ion and higher in the high-velocity components. Using the value of t^2 adopted for each ionization zone of the nebular components, we obtain abundances based on CELs consistent with those determined from RLs (see Table 16) and, therefore, making the ADF consistent with zero within the uncertainties. This suggests that the temperature fluctuation paradigm is capable of explaining the difference between the ADF in O⁺ and O²⁺. On the other hand, the existence of an H-deficient clump has been proposed as the cause of the ADF in Planetary Nebulae (Péquignot et al. 2002). Since the heating of the gas is mainly due by photoionization of H and He and cooled by collisional excitation of metallic ions, this scenario implies lower temperatures up to an order of magnitude in this metallic clump (Péquignot et al. 2002). As we mentioned in § 4.3.1, the T_e (O II) determined for the nebular component of cut 2 (which must be representative of the other nebular components) is consistent with T_e ([O III]) within the uncertainties, discarding the aforementioned scenario in the nebular components analyzed in this work. **E: Although the indirect evidences of temperature inhomogeneities are capable of explain the ADF in the nebular components, we remark there may be other scenarios that are little explored and may also explain it.**

However, the situation is different for the high-velocity components. Considering the ionic abundances assuming $t^2 > 0$, the ADF decreases but is not zero. For example, in the case of HH529III, the ADF(O²⁺) goes from 0.33 to 0.17 when considering $t^2 = 0.021$. Since we do not find evidence of higher temperature fluctuations

in the high-velocity components by using the temperatures determined in § 4 and the t^2 -formalism described in § 6, this suggests the presence of another effect apart (or in addition) to the classic description of temperature inhomogeneities. A similar result was found by Mesa-Delgado et al. (2009) in the case of HH202S (see their Sec 5.5). For the high-velocity components, the presence of a H-deficient clump can not be discarded as we discuss in § 8.3. However, there may be other phenomena involved.

8 TOTAL ABUNDANCES

We have to use ionization correction factors (ICFs) to estimate the contribution of the unseen ions in the total abundance of some elements. Following the analysis of the different ICF schemes for C, N, Ne, S and Ar done by Arellano-Córdova et al. (2020), we adopt the ICFs shown in Table 18 for these elements. In the case of He, Fe and Ni, we use the ICFs from Kunth & Sargent (1983), Rodríguez & Rubin (2005) and Delgado-Ingla et al. (2016), respectively. Results of total abundances based on CELs are presented in Table 19 and in Table 20, for the case of $t^2 = 0$ and $t^2 > 0$. Total abundances based in RLs are presented in Table 21. In this case, we do not expect significant changes in the total abundances within the temperature fluctuation paradigm due to the low dependence on temperature of RLs. The ICFs are generally based on the degree of ionization measured with the ionic abundances of O. For consistency, in the case of abundances based on CELs, we use the degree of ionization determined also with CELs. Analogously in the case of RLs.

8.1 Total abundances with CELs

8.1.1 Oxygen, Chlorine and Ar

In the cases of O and Cl, all the present ionization states are observed and the calculation of their total abundance does not require ICF. In HH529III, we could only estimate an upper limit for Cl⁺.

Table 17. Abundance Discrepancy Factor (ADF) for different ions in the components of each cut.

Cut	Component	ADF(O ⁺)	ADF(O ²⁺)	ADF(Ne ²⁺)	ADF(C ²⁺) [*]
1	Nebular	0.46 ± 0.14	0.15 ± 0.07	-	0.51 ± 0.03
2	HH529II	<0.55	0.29 ± 0.10	0.79 ± 0.09	-
2	Nebular	0.42 ± 0.12	0.17 ± 0.05	0.37 ± 0.04	0.52 ± 0.03
3	HH529III	<0.12	0.33 ± 0.11	-	-
3	Nebular	0.52 ± 0.14	0.17 ± 0.06	0.31 ± 0.15	0.51 ± 0.03
4	Nebular	0.46 ± 0.14	0.17 ± 0.06	-	0.50 ± 0.02
Combined cuts		0.44 ± 0.12	0.21 ± 0.05	-	0.54 ± 0.03

* We adopt $12 + \log(C^{2+}/H^+) = 7.835$ from UV CELs considering the slit positions 5 and 7 of [Walter et al. \(1992\)](#).

Table 18. ICFs used to estimate the abundance of unseen ions.

Element	ICF Reference
He	Kunth & Sargent (1983)
C	Berg et al. (2019)
N	Peimbert & Costero (1969)
Ne	
S	Stasińska (1978)
Ar	Izotov et al. (2006)
Fe	Rodríguez & Rubin (2005)
Ni	Delgado-Ingla et al. (2016)

However, even if we assume this upper limit as the real value, the contribution of this ion to the total Cl abundance is negligible. In the case of Ar, the ICF model of [Izotov et al. \(2006\)](#) shows that the contribution of Ar^{+/H⁺ to the total abundance of Ar/H is negligible in all the analyzed components. Thus, Ar/H=Ar²⁺/H⁺+Ar³⁺/H⁺. As we mentioned in § 5.1.1, the Cl/O ratio is highly consistent with the solar value adopted by [Lodders \(2019\)](#) for the case of $t^2 = 0$. Using $t^2 > 0$, the average Cl/O value is also consistent with the solar one of -3.50 ± 0.09 . In the case of Ar, the average value of Ar/O is -2.16 ± 0.03 for $t^2 = 0$ and -2.23 ± 0.03 for $t^2 > 0$, both within the value -2.23 ± 0.12 adopted by [Lodders \(2019\)](#). There are no appreciable differences in the Ar/O and Cl/O ratios between the nebular components and the high-velocity ones.}

8.1.2 Nitrogen, Neon and Sulphur

The estimation of the total abundances of N, Ne and S strongly depends on the ICFs shown in Table 18. In the case of N, since the only observed ion is N⁺ and considering the high degree of ionization of the Orion Nebula and the high-velocity components, the calculation of total N may be somewhat uncertain. In a scheme of the form $N = ICF \times N^+/H^+$, the ICF reaches values between 4 and 16 for the nebular and the high-velocity components, respectively. Using $t^2 = 0$ in the nebular components, the average value of N/O is -0.86 ± 0.02 , in complete agreement with the suggested solar value of -0.88 ± 0.14 ([Lodders 2019](#)). However, in the case of $t^2 > 0$ for the nebular components, the value of the ratio N/O = -0.98 ± 0.02 suggests an underestimation of N. In the high-velocity components, both in the case of $t^2 = 0$ and $t^2 > 0$, the N/O ratios show that the central value of N may be underestimated. Ne/O values do not change appreciably between nebular components and high-velocity ones. The average values are -0.65 ± 0.03 and -0.61 ± 0.02 for case $t^2 = 0$ and $t^2 > 0$, respectively, somewhat smaller than the solar value of -0.58 ± 0.12 ([Lodders 2019](#)), but within the error range. S/O values also do not differ appreciably between high-velocity and nebular components. For $t^2 = 0$ the average value is S/O = -1.51 ± 0.05 and for $t^2 > 0$ S/O = -1.64 ± 0.05 , while the solar value from [Lodders \(2019\)](#) is -1.58 ± 0.08 .

8.1.3 Nickel and Iron

Ni/H abundances are estimated using the ICF scheme derived by [Delgado-Ingla et al. \(2016\)](#) and are presented in Table 19 and Table 20 for $t^2 = 0$ and $t^2 > 0$, respectively. The estimation of this abundance is rather uncertain as discussed in § 5.1.2.

In the case of Fe, considering the absence of He II lines in our spectra, we do not expect to have Fe⁴⁺ in the nebula and therefore $Fe/H = Fe^+/H^+ + Fe^{2+}/H^+ + Fe^{3+}/H^+$. We have determined the abundance of Fe²⁺ and Fe³⁺ for all the components of each cut with the exception of HH529III, where we could only estimate an upper limit to Fe^{3+}/H⁺. In the high-velocity components, the absence of usually relatively intense [Fe II] lines as $\lambda\lambda 4287, 5158$ and 5262, together with the high ionization degree of the gas, are indicative of a negligible contribution of Fe⁺ to the total abundance. Thus, in these cases $Fe/H = Fe^{2+}/H^+ + Fe^{3+}/H^+$. In the nebular components, although a large number of [Fe II] lines have been detected, their emission is mainly produced by fluorescence ([Rodríguez 1999; Verner et al. 2000](#)). Therefore, most of the observed lines will not provide reliable estimates of Fe⁺ abundance. Unfortunately, [Fe II] $\lambda 8617$, a line almost insensitive to fluorescence ([Lucy 1995; Baldwin et al. 1996](#)) can not be observed due to the physical gap of the CCDs in the Red Arm of UVES. However, previous studies with direct estimations of Fe⁺ in the Orion Nebula as [Rodríguez \(2002\)](#) or [Mesa-Delgado et al. \(2009\)](#), obtain Fe⁺/Fe²⁺ ratios between 0.05 and 0.27. Considering the approximation $Fe/H = Fe^{2+}/H^+ + Fe^{3+}/H^+$, the neglected Fe^{+/H⁺ ratio would contribute to Fe/H up to 0.06 dex in the worst case (calculating Fe^{2+}/H⁺ with T_e (high) and assuming $Fe^+/Fe^{+2} = 0.27$). This maximum increase is within the range of uncertainties associated with the sum of Fe²⁺ and Fe³⁺ abundances and therefore, it seems reasonable to consider $Fe/H \approx Fe^{2+}/H^+ + Fe^{3+}/H^+$ for the nebular component as well.}}}

[Rodríguez & Rubin \(2005\)](#) proposed two ICFs for Fe, one derived from photoionization models and the other from data with detection of [Fe III] and [Fe IV] lines. The values of Fe/H obtained using both ICFs are discrepant, perhaps due to errors in the atomic data of the ions involved and the true total Fe abundance is expected to be in between the values obtained from both ICFs ([Rodríguez & Rubin 2005; Delgado-Ingla et al. 2014](#)). We use the described ICFs only for HH529III and its Fe/H abundance is presented as a limited range, defined from the predictions of both ICFs as shown in Table 19 and Table 20.

In HH529II, the abundances of Fe/H and Fe/O are higher than in the nebular components independently of whether the temperature T_e (low) or T_e (high) is taken to derive Fe^{2+}/H⁺. The same behavior is observed in HH529III for $t^2 = 0$, although the uncertainty in Fe/H do not allow us to be conclusive in the case of $t^2 > 0$. However, as it is discussed in § 4.2, the representative temperature to derive Fe^{2+}/H⁺ in HH529II and HH529III is likely to be T_e (high) while in the nebular components is T_e (low).}}

Using the above, the average Fe/O ratio in the nebular components is -2.53 ± 0.02 while for HH529II is -2.14 ± 0.08 with $t^2 = 0$. This represents an increase in the total abundance of gaseous Fe by a factor of 2.45. The same increase is observed in the case of $t^2 > 0$. For HH529III the increase is in a range of between a factor 1.30 and 2.40. Taking the solar value of Fe/O = -1.28 ± 0.08 recommended by Loddors (2019), we find that only 6% of the total Fe is in gaseous phase in the nebular component, while this fraction amounts to 14% for HH529II and between 8% and 14% for HH529III. In the case of HH202S, Mesa-Delgado et al. (2009) found that this proportion is around 44%. These results are consistent with theoretical studies predicting that fast shocks are effective destroying dust grains (see Jones et al. 1994; Mouri & Taniguchi 2000, and references therein). However, this also indicate that most of the Fe is still depleted into dust grains in the shocks associated with these HH objects. Another evidence of surviving dust is the detection of thermal dust mid-IR emission at $11.7 \mu\text{m}$ coincident with both HH529II and III as well as HH202S (Smith et al. 2005). A key factor is determining observationally the relationship between the level of depletion of Fe and some particular characteristic of each HH, such as its velocity. The 3D velocity of HH202S is $\sim 89 \text{ km s}^{-1}$ (see Sec 5.4 of Mesa-Delgado et al. (2009)) while for HH529 is $\sim 65 \text{ km s}^{-1}$ (see § 10.1), indicating that the fraction of gaseous Fe in the shock front grows with the velocity of the HH. However, we need more objects to establish a clear relationship. This will be done with the inclusion of other photoionized Herbig-Haro objects.

8.2 Total abundances with RLs

8.2.1 Oxygen

The total O abundances based on RLs are determined directly from $\text{O/H} = \text{O}^+/\text{H}^+ + \text{O}^{2+}/\text{H}^+$. In the high-velocity components, the absence of O I RLs indicate an small contribution of O^+/H^+ in the total O/H abundance. In § 5.2.3 we estimate an upper limit to this ionic abundance in HH529II and HH529III, which can contribute up to 0.05 dex to the total O/H value. Thus, for these high-velocity components the total O/H abundance is determined from the O^{2+}/H^+ value considering the possible O^+/H^+ contribution within the error range.

8.2.2 Helium

Considering both the absence of an ionization front and the emission of lines of neutral elements together with a hardness radiation of $\log(\eta) < 0.9$ (see § 6), it is likely that the fraction He^0/H^+ in the high velocity components is negligible. For these cases we take $\text{He/H} = \text{He}^+/\text{H}^+$. In the nebular components, we estimate the fraction of neutral helium within the ionized zone with the ICF scheme of Kunth & Sargent (1983), obtaining that the He^0/H^+ fraction is approximately 10%. This value is consistent with the other ICF schemes tested in Méndez-Delgado et al. (2020) for the Orion Nebula. The prediction of the ICF makes the abundances of He/H consistent in all components of all cults, as it is shown in Table 21. However, the dependence of the total amount of He^0 with the T_{eff} of the ionizing star is not considered in the usual ICF schemes for He and may introduce errors as it is discussed by Delgado-Ingla et al. (2014) for Planetary Nebulae. Despite this, in the Orion Nebula, we expect to have a small contribution of He^0/H^+ , where the radiation softness parameter gives values of $\log(\eta) < 0.9$ also for the nebular components.

8.2.3 Carbon and Neon

In the case of the high-velocity components, due to the high degree of ionization estimated from the ionic O abundances based on RLs, we expect to have a negligible contribution of C^+/H^+ in the total C/H abundance. We expect the same in the case of Ne^+/H^+ for HH529II. In these cases we take ICF=1. For the nebular components, we use the ICF from Peimbert & Costero (1969) for Ne, as in § 8.1.2 but using the ionic abundances of O based on RLs. The resulting Ne/O ratio for RLs is -0.44 ± 0.03 and -0.23 ± 0.10 for the nebular components and HH529II respectively. This indicates that the relative abundance of Ne over O is higher using RLs than CELs (See § 8.1.2). In the nebular components, Ne/O values both based on RLs and CELs are in agreement with the solar value of -0.58 ± 0.12 (Loddors 2019), given the wide range of uncertainties of this quantity. However, for HH529II, the Ne/O is out from the solar value and may indicate an overestimation of $\text{Ne}^{2+}/\text{H}^+$.

To estimate the contribution of C^+/H^+ to the total C/H abundance for the nebular components, we use the ICF presented by Berg et al. (2019). It is important to note that this ICF may not be completely adequate to our case since it has been optimized for low-metallicity objects (up to O/H=8.0). Despite this, the results obtained with this scheme are more consistent with the expected solar values, compared to other ICFs published in the literature, as is discussed by Arellano-Córdova et al. (2020). For comparison, we present the C/H derived with the ICF of Amayo et al. (in prep) (private communication), whose scheme is optimized for a wider range of metallicity. Table 21 shows that the results with both ICFs are consistent, although there is a slight difference, probably due to an overestimation of C/H by the ICF of Berg et al. (2019). The average C/O value for the nebular components is -0.20 ± 0.02 using the ICF of Berg et al. (2019) and -0.26 ± 0.02 using the scheme of Amayo et al. (in prep). This last value is the most consistent one with the recommended solar value of -0.26 ± 0.09 . The C/O value for HH529II is -0.37 ± 0.08 while for HH529III is -0.28 ± 0.12 .

8.3 An slight overmetallicity in the high-velocity components?

A notable aspect among the total abundances calculated and commented previously, is the fact that the metallic abundances are higher in HH529II and HH529III than in the nebular components. The abundance of O/H in the high-velocity components is higher between 0.10 and 0.14 dex with respect to the nebular values, both in the case of abundances based on CELs and RLs. This difference is in agreement with the 0.12 ± 0.03 dex of O which may be depleted into dust grains in the Orion Nebula (Mesa-Delgado et al. 2009). Nevertheless, the abundance of elements like Ar, Ne, S and Cl grows proportionally to that of O, so the Ar/O, Ne/O, S/O and Cl/O ratios do not change appreciably between the nebular components and the high-velocity ones. Since Ar and Ne are noble elements, it is not expected to have them depleted into dust grains. Thus, this indicate that the increase of the O/H abundance in HH529II and HH529III is not entirely due to the destruction of dust grains. In addition to this, if we consider that the dust-phase O is trapped in olivine $(\text{Mg}, \text{Fe})_2\text{SiO}_4$, pyroxene $(\text{Mg}, \text{Fe})\text{SiO}_3$ or oxides like Fe_2O_3 , then the gaseous O must grow in proportion to the release of elements like Fe. As we mention in § 8.1.3, the proportion of gaseous Fe present in HH202S is higher than in HH529II and HH529III. This implies that the increase of O/H due to dust destruction must be much less than 0.06 dex, a value that could be attributed to this phenomenon in HH202S (Mesa-Delgado et al. 2009).

Table 19. Total abundances based on CELs with $t^2 = 0$.

Element	Cut 1		Cut 2		Cut 3		Cut 4	Combined cuts
	Nebula	HH529II	Nebula	HH529III	Nebula	Nebula	Nebula	
O	8.45 ± 0.02	8.57 ± 0.03	8.46 ± 0.03	8.59 ± 0.04	8.45 ± 0.03	8.47 ± 0.03	8.46 ± 0.03	
N	7.57 ± 0.04	7.40 ^{+0.16} _{-0.10}	7.62 ^{+0.07} _{-0.05}	7.37 ^{+0.26} _{-0.14}	7.60 ^{+0.08} _{-0.07}	7.64 ^{+0.08} _{-0.06}	7.60 ^{+0.06} _{-0.05}	
Ne	7.81 ± 0.04	7.94 ± 0.03	7.82 ± 0.04	7.90 ± 0.04	7.83 ± 0.03	7.86 ± 0.04	7.82 ± 0.04	
S	6.89 ± 0.04	7.18 ^{+0.07} _{-0.06}	6.96 ^{+0.08} _{-0.09}	7.05 ^{+0.08} _{-0.06}	6.98 ± 0.05	6.94 ± 0.05	6.98 ± 0.04	
Cl	4.92 ± 0.06	5.03 ± 0.05	4.97 ± 0.06	5.11 ± 0.06	4.99 ± 0.06	4.99 ± 0.06	4.97 ± 0.05	
Ar	6.32 ± 0.03	6.40 ± 0.02	6.32 ± 0.03	6.38 ± 0.03	6.34 ± 0.02	6.30 ± 0.03	6.33 ± 0.03	
Fe*	6.03 ± 0.06	6.42 ± 0.07	6.07 ± 0.04	6.19<Fe<6.44	6.06 ± 0.05	6.05 ± 0.06	6.08 ± 0.05	
Fe**	5.91 ± 0.07	6.34 ± 0.08	5.94 ± 0.05	5.97<Fe<6.20	5.94 ± 0.07	5.92 ± 0.08	5.95 ± 0.07	
Ni	4.59 ± 0.14	5.12 ^{+0.15} _{-0.10}	4.58 ^{+0.18} _{-0.17}	4.71 ^{+0.18} _{-0.12}	4.60 ^{+0.17} _{-0.16}	4.62 ^{+0.13} _{-0.12}	4.67 ^{+0.11} _{-0.10}	

* indicates that T_e (high) was used.** indicates that T_e (low) was used.**Table 20.** Total abundances based on CELs with $t^2 > 0$.

Element	Cut 1		Cut 2		Cut 3		Cut 4	Combined cuts
	Nebula	HH529II	Nebula	HH529III	Nebula	Nebula	Nebula	
O	8.66 ± 0.05	8.76 ± 0.04	8.66 ± 0.05	8.78 ± 0.07	8.64 ± 0.04	8.67 ± 0.05	8.65 ± 0.05	
N	7.66 ^{+0.11} _{-0.08}	7.45 ^{+0.35} _{-0.16}	7.69 ^{+0.14} _{-0.10}	7.41 ^{+0.44} _{-0.21}	7.68 ^{+0.16} _{-0.10}	7.71 ^{+0.15} _{-0.10}	7.68 ^{+0.13} _{-0.09}	
Ne	8.04 ± 0.08	8.16 ± 0.04	8.05 ± 0.07	8.13 ^{+0.09} _{-0.08}	8.04 ± 0.06	8.08 ^{+0.08} _{-0.07}	8.05 ^{+0.07} _{-0.06}	
S	6.95 ± 0.05	7.24 ^{+0.10} _{-0.07}	7.03 ± 0.06	7.10 ^{+0.11} _{-0.08}	7.05 ^{+0.07} _{-0.06}	7.01 ^{+0.06} _{-0.05}	7.05 ^{+0.06} _{-0.05}	
Cl	5.04 ± 0.06	5.17 ± 0.09	5.10 ± 0.07	5.24 ± 0.10	5.12 ± 0.07	5.12 ± 0.07	5.10 ± 0.07	
Ar	6.44 ± 0.04	6.52 ± 0.03	6.43 ± 0.04	6.49 ± 0.04	6.44 ± 0.03	6.42 ± 0.04	6.44 ± 0.04	
Fe*	6.26 ± 0.09	6.71 ± 0.09	6.29 ± 0.06	6.32<Fe/H<6.48	6.41 ± 0.12	6.29 ± 0.09	6.37 ± 0.11	
Fe**	6.19 ± 0.10	6.66 ± 0.10	6.22 ± 0.07	6.15<Fe/H<6.31	6.35 ± 0.14	6.22 ± 0.11	6.31 ± 0.13	
Ni	4.70 ± 0.19	5.22 ^{+0.26} _{-0.13}	4.71 ^{+0.19} _{-0.18}	4.81 ^{+0.27} _{-0.23}	4.71 ^{+0.18} _{-0.16}	4.72 ^{+0.15} _{-0.13}	4.78 ^{+0.13} _{-0.12}	

* indicates that T_e (high) was used.** indicates that T_e (low) was used.**Table 21.** Total abundances based on RLs.

Element	Cut 1		Cut 2		Cut 3		Cut 4	Combined cuts
	Nebula	HH529II	Nebula	HH529III	Nebula	Nebula	Nebula	
O	8.71 ± 0.03	8.83 ± 0.07	8.70 ± 0.03	8.84 ± 0.09	8.71 ± 0.03	8.72 ± 0.03	8.73 ± 0.03	
He	10.94 ± 0.02	10.95 ± 0.03	10.94 ± 0.01	10.95 ± 0.03	10.94 ± 0.02	10.95 ± 0.02	10.94 ± 0.02	
C*	8.56 ± 0.04		8.52 ± 0.03		8.52 ± 0.04		8.51 ^{+0.04} _{-0.03}	8.51 ^{+0.04} _{-0.03}
C**	8.48 ^{+0.08} _{-0.07}	8.46 ± 0.02	8.45 ± 0.05	8.56 ± 0.03	8.45 ^{+0.07} _{-0.06}	8.44 ± 0.06	8.45 ^{+0.06} _{-0.05}	
Ne	-	8.60 ± 0.06	8.26 ± 0.04	-	8.23 ± 0.15	-	-	-

* Total abundances of the nebular components derived with the ICF of Berg et al. (2019).

** Total abundances of the nebular components derived with the ICF of Amayo et al. (in prep.).

The increase in the metallic abundances determined with CELs in the high-velocity components can not be explained by smaller temperature inhomogeneities (t^2) than in the nebular ones, since in that case we would expect smaller values of the ADF, contrary to what we get in Table 17. The fact that the increase of the O/H abundance is also observed in the determinations based on RLs rules out the possibility that it can be due to an inadequate estimation of the temperature used to calculate the ionic abundances based on CELs within the classic Direct-Method. In addition to this, the same behaviour was observed by BMB06, using different data with which they studied separately the high-velocity emission that includes part of HH529II and HH529III. The data from BMB06 were reanalyzed by Simón-Díaz & Stasińska (2011) finding again a higher O/H

abundance in the HH object than in the nebular component. Due to all the considerations commented above, observational errors or in the procedure to estimate the chemical abundances are unlikely.

One possibility is that the source of origin of the Herbig-Haro object has expelled a knot of H-deficient material within the main flow of gas. As we mentioned in § 7 in this scenario, we would expect a lower temperature in the metallic knot, up to an order of magnitude. However, since the main coolants are the IR fine-structure CELs as [O III] 52, 88μm (Yuan et al. 2011), the temperature diagnostics based on optical CELs would show mainly the physical conditions of the “normal” metallicity gas flowing in the HH. The origin of this hypothetical knot may be in the evaporation of protoplanetary discs

around newly formed stars (Yuan et al. 2011), a probable scenario in the origin of HH529.

About the above, it is well known that HH529 is a source of IR emission in the Orion Nebula (Robberto et al. 2005; Smith et al. 2005), strongly emitting at $10\mu\text{m}$ and $11.7\mu\text{m}$. Smith et al. (2005) show that the $11.7\mu\text{m}$ radiation arises from thermal dust emission and its visible both behind the leading bow shock and within the jet body of HH529 (see their Fig. 7). After analyzing different scenarios, Smith et al. (2005) conclude that the dust may be entrained at the origin of the jet, which implies that at least part of the ejected material comes from a radius larger than the sublimation radius in the accretion disc of the HH source. Some of this material may be made up of H-deficient solids. However, this scenario requires a deeper analysis of solid body destruction in new formed stars, an idea further explored in planetary nebulae (Henney & Stasińska 2010). Unfortunately, the contamination of the line O II $\lambda 4089.29$ with a ghost feature makes impossible to have a reliable estimate of $T_c(\text{O II})$, which should reflect lower temperatures in the case of the existence of the mentioned clump. Subsequent analysis of new photoionized Herbig-Haro objects, whose analysis we have in preparation can give additional information and shed light on this issue.

9 KINEMATICAL ANALYSIS FROM UVES DATA

We calculate the radial velocity of each line in the heliocentric framework by comparing its observed wavelength (after applying the radial velocity correction) with its theoretical wavelength in air. All the theoretical values have been taken from the Atomic Line List v2.05b21 (Van Hoof 2018). Wavelengths from this compilation list are mainly calculated from the theoretical energy difference between the levels connected by the transition. The exception are the hydrogenic lines, which include a weighted average of all the fine structure components.

We detect some evident inaccuracies in the theoretical wavelengths of [Cl III], [Cl IV] and [Ne III] in the Atomic Line List v2.05b21. This conclusion is based on the discrepant velocities that those lines show with respect to the rest of lines in the high-velocity components, that show fairly similar velocities independently of the ionization state of the ions and the elements (see § 9.1). For example, in the case of [Ne III] $\lambda 3869$, 3967, the Atomic Line List v2.05b21 gives $\lambda 3869.07 \pm 0.09$ and 3967.79 ± 0.10 based on the works of Persson et al. (1991) and Feuchtgruber et al. (1997). These wavelengths give velocities about -20 km s^{-1} displaced with respect to the mean velocity obtained for the rest of the lines. In this case, we decided to adopt the wavelengths $\lambda 3868.75$ and 3967.46 obtained by Bowen (1955) from high-resolution spectroscopy of nebulae. The [Cl III] and [Cl IV] lines show a similar problem; in this case, we adopt the reference wavelengths used by Esteban et al. (2004) that give consistent velocities. The wavelengths adopted for [S III] lines deserve special attention. The values given by the Atomic Line List v2.05b21 are $\lambda 6312.1 \pm 0.36$, 8829.4 ± 0.49 , 9068.6 ± 0.52 and 9530.6 ± 0.57 , taken from the work by Kaufman & Martin (1993). There is a small (but noticeable at our spectral resolution) discrepancy in the velocity obtained for [S III] $\lambda 6312$ and the rest of the lines of about 10 km s^{-1} . Assuming the velocities measured for the HI lines of HH529II, our best estimation of the rest wavelengths of the observed [S III] lines are $\lambda 6312.07 \pm 0.01$, 8829.70 ± 0.01 , 9068.93 ± 0.04 and 9530.98 ± 0.01 .

9.1 Radial velocity structure

In Table A7, we present the average velocity and full width at half maximum (FWHM) of each ion observed in the nebular component of cut 2 and in HH529II-III. The behaviour of the nebular component of cut 2 is representative of what is observed in the nebular components of the other cuts. In each column, we include in parentheses the number of lines of each kind whose values have been averaged. In this analysis, we discard lines with known blends and those affected by ghosts or by telluric emissions/absorptions. For O I, O II, C II and Ne II lines, we include only the lines used in § 5.2 for abundance determinations, ensuring that they are pure recombination lines and not affected by fluorescence. In the special case of [S III] lines we consider only the $\lambda 6312$ line, due to the aforementioned evident inaccuracies in the theoretical wavelengths of the rest of the [S III] lines. Fig. 14, shows the heliocentric velocity as a function of ionization potential relation for the data collected in Table A7.

From Fig. 14, it is clear that the nebular component presents a pattern consistent with the ‘‘blister’’ model for the Huygens Region of the Orion Nebula (O’Dell 2001; Ferland 2001; O’Dell et al. 2020, and references therein). The basic idea is that a layer of gas of the Orion Molecular Cloud (OMC) facing the direction towards the Sun is ionized by θ^1 Ori C, which is located in the foreground of OMC. As the gas gets ionized, it is accelerated towards the observer. Velocities of [O I], [C I], and [N I] are similar to the average velocity of the molecules in the OMC ($\sim 28\text{ km s}^{-1}$ Goudis 1982; O’Dell 2018, and references therein), then a rapid drop in the observed velocity (which means an increase in velocity compared to the OMC’s systemic velocity) of the ions whose ionization potential are between 6.77 and 13.6 eV is observed as well as a constant velocity after 13.6 eV . This behaviour has been observed in previous works (Kaler 1967; Fehrenbach 1977; O’Dell & Wen 1992; Esteban & Peimbert 1999). In this paper, we were able to eliminate most of the dispersion by using the observed constant radial velocity of HH529II.

In the upper right panel of Fig. 14, we present the difference between the radial velocity pattern of the nebular component and HH529II (which presents a constant radial velocity, independent of the ionization potential) rescaled by using the average radial velocity of 51 hydrogen lines in HH529II, whose rest-frame reference wavelengths λ_0 are the best established among all the ions. This panel proves that the dispersion seen in the upper left panel (which presents the radial velocity structure of the nebular component when using the difference between the observed wavelength position and λ_0) is not due to errors in the measurement of the spectral position of the lines or to a complex velocity structure but due to inaccuracies in the rest-frame reference wavelengths. By eliminating the aforementioned dispersion, we demonstrate that the acceleration of the gas in the Orion Nebula is constant with the ionization potential between 6.77 and 13.6 eV , and that is zero after this, reaching a constant velocity of $16.4 \pm 0.8\text{ km s}^{-1}$.

In the high-velocity components, there is a difference of $5.18 \pm 1.25\text{ km s}^{-1}$ between them. This is due to the presence of unresolved lower velocity components in HH529III, as its shown in Fig. 15, which also increase the real dispersion in the radial velocity structure of this component.

In the nebular component, whose radial velocity structure is not constant in all ions, the radial velocities of the selected O I, O II and Ne II lines are practically the same as those of [O III], [O III] and [Ne III] CELs. This reinforces the assumption that they are produced by pure recombination. For example, lets consider the O I

RLs from multiplet 1. If they were not arising from recombination processes, they would be mainly emitted in neutral and partially ionized zones of the nebula and then they should show a radial velocity similar to the systematic one of the OMC. In fact, OI lines from transitions between triplet levels (such as multiplet 4 $\lambda\lambda 8446.25, 8446.36, 8446.76$) are displaced around $\sim 10 \text{ km s}^{-1}$ than the velocity of the aforementioned multiplet 1, which shows the different nature of its origin, being the lines of multiplet 4 originated by starlight excitation (Grandi 1975b).

As shown, there is a significant dispersion in the rest-frame reference wavelengths λ_0 , which can be troublesome for kinematic studies with high spectral resolution. From the lines observed in HH529II and the velocity of -29.08 ± 0.36 , derived from the average of 51 hydrogen lines, we deduce a list of rest-frame wavelengths in air that eliminate the observed dispersion and are more suitable. It should be noted, that these wavelengths are entirely deduced from our observations and assuming that the rest-frame wavelengths of hydrogen are the best studied. The results are appended in an online table.

9.2 Electron temperature from thermal broadening of the line profiles

The observed line widths are the result of several physical processes. Apart from the instrumental width, σ_{ins} , the main contributors are the thermal width, σ_{th} , the fine structure broadening, σ_{fs} and the non-thermal contribution, σ_{nt} , which includes effects as turbulence and any other additional broadening process. Following García-Díaz et al. (2008, their equation 2), we use Eq. (19) to express the relationship commented above.

$$\sigma_{\text{obs}}^2 = \sigma_{\text{th}}^2 + \sigma_{\text{fs}}^2 + \sigma_{\text{ins}}^2 + \sigma_{\text{nt}}^2. \quad (19)$$

The thermal contribution of Eq. (19) is the Doppler broadening and depends linearly on the temperature, $\sigma_{\text{th}}^2 = 82.5 T_4 / A (\text{km/s})^2$, where A is the atomic weight of the emitting ion and $T_4 = T_e / 10^4$ (García-Díaz et al. 2008).

In principle, using Eq. (19) we can estimate T_e from the subtraction of the observed widths of H I and [O III] lines. The instrumental width affects the same for both kinds of lines and should be cancelled in the subtraction. García-Díaz et al. (2008) (hereinafter GHLD08) estimated $\sigma_{\text{fs}}^2 (\text{H I}) = 10.233 (\text{km/s})^2$, finding that $\sigma_{\text{fs}}^2 (\text{[O III]})$ is negligible. On the other hand, $\sigma_{\text{nt}}^2 (\text{H I})$ is not strictly equal to $\sigma_{\text{nt}}^2 (\text{[O III]})$, since the nebular volume occupied by both ions is different. GHLD08 define f as the fraction of the volume of H^+ occupied by O^{2+} and $(1-f)$ the fraction filled by O^+ and other ions with lower degree of ionization, as N^+ . We assume the average value $\langle f \rangle = 0.76$ estimated by GHLD08 for the Orion Nebula. Using equations 7 to 10 from GHLD08, we obtain $T_e = 8340 \pm 410 \text{ K}$ for the nebular component. In the case of the high-velocity components, we assume $f = 1.0$, obtaining $T_e = 8670 \pm 50 \text{ K}$ and $T_e = 10474 \pm 790 \text{ K}$ for HH529II and HH529III, respectively.

The resulting T_e values in the nebular component of cut 2 and HH529II are in remarkably good agreement with $T_e(\text{[O III]})$ from CELs as shown in Table 7. In the case of HH529III, the large difference between the values obtained from both methods is due to the contamination by several unresolved velocity components, as it is shown in Fig. 15 and discussed in § 10, that broadens the lines and provides wrong higher temperatures.

10 PROPER MOTIONS OF HH 529 II AND III

The plane-of-sky motions of the bow shocks in HH 529 have been previously reported in Table 3 of O'Dell & Henney (2008) and in sec 3.3.1.3 of O'Dell et al. (2015). However, the reported tangential velocities are very disparate, so we have re-measured the proper motions, using HST imaging over 20 years as it is described in § 2. The 1995 and 2015 images were aligned to the 2005 ACS image using Astrodrizzle⁵ and rebinned to the ACS pixel scale of 0.05 arcsec. The 2005 image itself has been aligned to the absolute astrometric reference of 2MASS, as painstakingly described in sec 3.3 of Robberto et al. (2013). Proper motions are estimated for the two intervals, 1995–2005 and 2005–2015, using the Fourier Local Correlation Tracking (FLCT) method (Welsch et al. 2004; Fisher & Welsch 2008)⁶ with a kernel width of 10 pixels (0.5 arcsec). For an assumed distance of 417 pc, a shift of 1 pixel in 10 years corresponds to approximately 10 km s^{-1} . A potential disadvantage of using the ACS data in this study is that the F658N ACS filter is relatively broad and includes both $\text{H}\alpha \lambda 6563$ and $[\text{N II}] \lambda 6583$, whereas the WFPC2 and WFC3 F656N filters are narrower and more effectively isolate $\lambda 6563$. Ionization gradients in the nebula can therefore contribute to differences in the images obtained, which would obscure the signal due to the gas motions. However, the degree of ionization in HH 529 III and II is so high that this turns out not to be an issue in this object. Results are presented in Table 22 and Figure 15.

We find that HH 529 III consists of at least two distinct moving structures. The large outer curved bow, which we call III a, is relatively smooth, spanning about 7 arcsec in its brightest part, but with fainter wings (best visible on the ratio image) that extend farther. We cover the bright part of the bow with 5 sample ellipses: a1 to a5, where a3 seems to be the apex of the bow but a2 is the one that falls in the UVES slit. Roughly 0.7 arcsec to the east of III a is a smaller, knottier bow, which we call III b and cover with 3 sample ellipses: b1, b2 and b3. The brightest knot is b2, but it is the b1 sample that falls in the UVES slit. HH 529 II is found to consist of three distinct bows with separations of order 1 arcsec, which we call II a, II b, and II c, with II a and II b falling in the UVES slit.

10.1 Physical aspects of the high velocity components

From a dynamical point of view, Dyson (1984) shown that the interaction of the outflows from low-mass protostars is isothermal. Moreover, this is the appropriate situation for a shock immersed in a fully ionized medium, where the temperature is defined by the thermal equilibrium of an ionized gas. In this case, the compression of the gas is not limited as in the adiabatic case. Using the total or 3D velocity (v_{tot}) of the high-velocity components within the reference framework of the shock, and the sound speed in an ionized gas c_0 , we can estimate the Mach number M , using Eq. (20) and Eq. (21).

$$M = \frac{|v_{\text{tot}}|}{c_0}, \quad (20)$$

$$c_0 = \sqrt{\frac{\gamma k T}{\mu_0 m_H}}, \quad (21)$$

⁵ <https://drizzlepac.readthedocs.io>

⁶ We used version 1.07 of FLCT, obtained from <http://cgem.ssl.berkeley.edu/cgi-bin/cgem/FLCT/home>, together with version 1.04 of the Python wrapper pyflct, obtained from <https://github.com/PyDL/pyflct>.

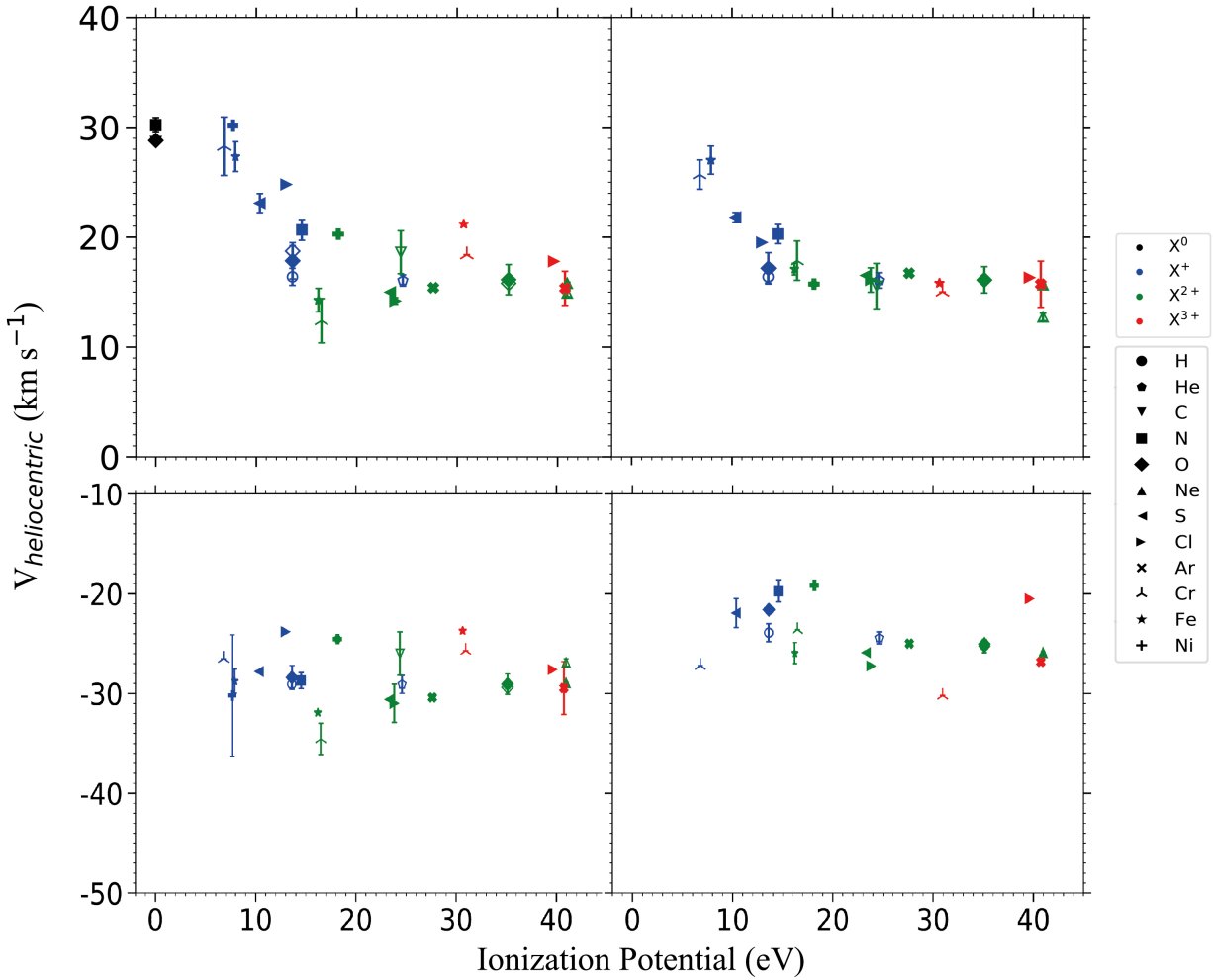


Figure 14. Observed radial velocity of the ions as function of the ionization potential. The upper left, bottom left and bottom right panels correspond to the radial velocities derived by considering the rest-frame reference wavelength λ_0 and the observed one λ in the heliocentric frame of reference for the nebular component of the cut 2, HH529II and HH529III, respectively. The upper right panel is defined with the difference of velocities between the nebular component and HH529II (which velocity structure is constant with the ionization potential) and rescaled using the velocity determined for H I lines, whose rest-frame wavelengths λ_0 are the best established.

where k is the Boltzmann constant, T the temperature, μ_0 the mean mass per particle, m_H the hydrogen mass and γ the adiabatic index. In § 9.1, the heliocentric velocities of the different ions were presented for both shocks. Considering the OMC reference framework ($\sim 28 \text{ km s}^{-1}$, Goudis 1982) and the average tangential motion of $35 \pm 2 \text{ km s}^{-1}$ estimated in § 10 for HH529, we obtain total velocities of $-62.60 \pm 1.34 \text{ km s}^{-1}$ and $-66.95 \pm 1.09 \text{ km s}^{-1}$ for HH529III and HH529II, respectively. Considering $T_e = 8400 \pm 150 \text{ K}$ for the nebular component and $\gamma = 1$ (isothermal process), we obtain $c_0 = 11.80 \pm 0.10 \text{ km s}^{-1}$. Thus, assuming that both are external working surfaces, we derive a Mach number of $M = 5.31 \pm 0.12$ and $M = 5.68 \pm 0.10$ for HH529III and HH529II, respectively.

In the case of an isothermal shock, the ratio between the gas densities before (n_{pre}) and after (n_{post}) the shock follows Eq. (22).

$$\frac{n_{\text{post}}}{n_{\text{pre}}} = M^2 \quad (22)$$

Using this value presented in Table 7, we obtain a pre-shock density $n_{\text{pre}} = 1560 \pm 280 \text{ cm}^{-3}$ for HH529III. This value is con-

sistent with densities determined in photoionized areas of the Orion Nebula outside the Huygens region, where the density decreases radially (Mesa-Delgado et al. 2008). This would place HH529III in the foreground of the main ionization front. On the other hand, considering also HH529II as an external working surface, we would obtain a pre-shock density $n_{\text{pre}} = 370 \pm 60 \text{ cm}^{-3}$, indicating that HH529II is impacting the ambient gas in a zone more external from where HH529III does. Thus, HH529II would be located well ahead towards the observer. This scenario seems unlikely, considering the similar ionization state of the gas in both HH objects. In addition to this, the multiple velocity components included in HH529III that increase the real dispersion of the velocity with respect to what is observed in HH529II and the fact that HH529III is denser than HH529II almost a factor 4 (see § 4), evidence that HH529II can correspond to an internal working surface (Masciadri & Raga 2001) of the jet beam. This internal shock may have its origin in a somewhat later ejection of material from the common origin of HH529 (located at the star COUP 666 by O'Dell et al. 2015), flowing along the jet beam opened by the main shock front (HH529III). This scenario

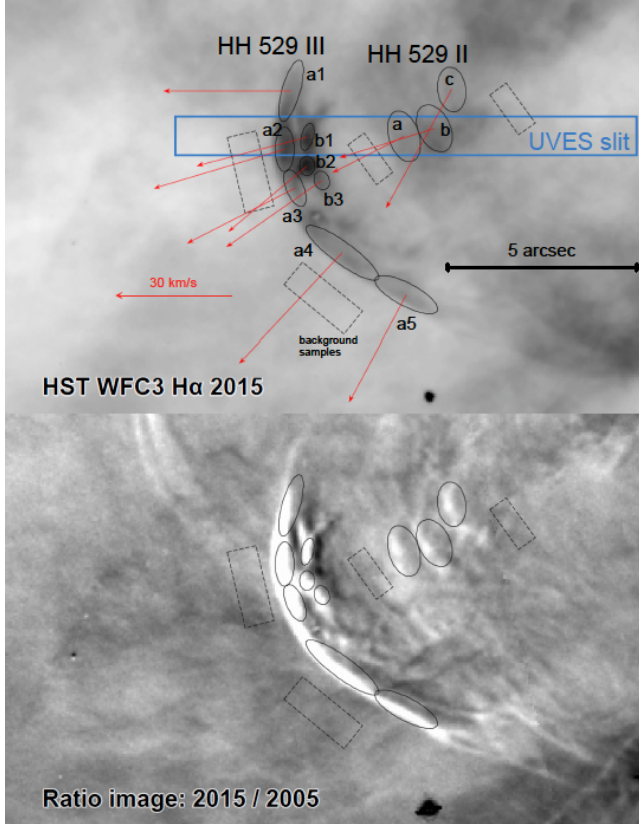


Figure 15. Tangential velocities of shock features in HH 529 II and III derived from 3 epochs of HST imaging. Upper panel shows various discrete features identified in the bow shocks (black ellipses with arrows indicating the average proper motion of each feature). Small dashed rectangles indicate regions where the nebular background brightness was measured and the large rectangle shows the position of the spectrograph slit. The background negative grayscale shows an *HST* WFC3 image in the F656N filter from 2015. Lower panel shows the ratio between the 2015 image and an *HST* ACS image in the F658N filter from 2005 (white means brighter in 2015). This highlights the changes in the nebula over that 10-year period, which are principally due to motions of the shocked gas.

has been studied in detail by Raga & Reipurth (2004) for HH jets emerging from a neutral cloud into an H II region.

In both high-velocity components, it is noticeable the absence of [OI] (see Fig. 2) and the weakness of lines of low ionization potential ions. This proves that HH529II and HH529III are objects fully photoionized and do not contain a trapped ionization front (Masciadri & Raga 2001), contrary to what was found by Mesa-Delgado et al. (2009) for HH20S. Due to the fact that HH529 is fully photoionized, we can assure that the entire jet beam inside the HII region is observable in optical emission lines, contrary to partially ionized or neutral Herbig-Haro objects, where only limited regions can be observed (Raga et al. 2000a,b).

Considering the arctangent of the ratio between the average tangential velocity ($\sim 35 \pm 2 \text{ km s}^{-1}$) and the radial velocity of HH529II, with less dispersion than HH529III ($-57.07 \pm 0.36 \text{ km s}^{-1}$), we get a flow angle with respect the sky plane of $58.47 \pm 1.50^\circ$, in agreement with the result of O'Dell & Henney (2008) ($\sim 54^\circ$) but discrepant with the results of O'Dell et al. (2015) ($\sim 83^\circ$). The flow angle found implies that the observed spectra of the high-velocity components should integrate the emission along an

Table 22. Proper motions of shock features

Feature	UVES cut	V_t km s $^{-1}$	PA deg	Contrast $S(\text{H}\alpha)/S(\text{H}\alpha, \text{BG})$
(1)	(2)	(3)	(4)	(5)
HH 529 III a1		33 ± 3	90 ± 3	0.46 ± 0.14
HH 529 III a2	3	36 ± 1	107 ± 7	0.82 ± 0.11
HH 529 III a3		32 ± 1	117 ± 3	0.52 ± 0.14
HH 529 III a4		39 ± 2	137 ± 5	0.41 ± 0.07
HH 529 III a5		32 ± 1	152 ± 10	0.27 ± 0.07
HH 529 III b1	3	30 ± 2	105 ± 3	0.95 ± 0.09
HH 529 III b2		27 ± 1	130 ± 1	1.14 ± 0.10
HH 529 III b3		30 ± 2	125 ± 4	0.64 ± 0.07
HH 529 II a	2	21 ± 9	117 ± 58	0.25 ± 0.03
HH 529 II b	2	26 ± 5	107 ± 4	0.35 ± 0.08
HH 529 II c		35 ± 9	151 ± 87	0.22 ± 0.03

COLUMNS: (1) Name of shock feature (see Fig. 15 for positions). (2) Spatial cut of the UVES spectrum where this feature appears, if any. (3) Mean tangential velocity for each feature, weighted by background-subtracted surface brightness, $S(\text{H}\alpha)$, of each pixel. (4) Mean position angle of proper motion, weighted in the same way. (5) Mean relative H α brightness with respect to nebular background. For columns 3, 4, and 5, the \pm uncertainties correspond to the root-mean-square variation over each sample region and do not include systematic uncertainties, which are of order 2 km s^{-1}

important fraction of the ionized jet beam, including the compressed gas in the leading working surface and the gas of the jet beam behind.

11 SUMMARY AND CONCLUSIONS

We have observed the bowshocks HH529II and HH529III from the photoionized Herbig-Haro HH529 under photometric conditions with the echelle spectrograph UVES at VLT. Our observations have an effective spectral resolution of $\sim 6.5 \text{ km s}^{-1}$ covering a spectral range of 3100–10420Å. We defined 4 spatial cuts in the slit of 10 arcsecs of our observations to separate HH529II from HH529III. Our spectral resolution permitted us to study the blueshifted high-velocity components separately from the nebular emission of the Orion Nebula. Thus, we got 6 resulting spectra: 4 of the nebular emission and one for each bowshock. We measured up to 633 emission lines in the Orion Nebula and 376 and 245 in the case of HH529II and HH529III, respectively. We defined another spectrum labeled as “combined cuts” with the sum of all components, with the porpoise of analyze the impact of the bowshocks in a single low-spectral resolution longslit observation. We also take advantage of the 20 years of archival HST imaging to analyze proper motions of HH529 and their physical impact.

Considering the absence of emission lines of neutral elements such as [OI] and the rather faint emission from low ionization ions such as [OII] in HH529II and HH529III, we conclude that they are fully photoionized and present a high ionization degree. We analyzed 5 density diagnostics based on CEL ratios. In the nebular components, we found consistent densities between all the diagnostics, getting a value of $n_e \approx 6000 \pm 1000 \text{ cm}^{-3}$ (for each specific cut, see Table 7). For HH529II and HH529III, the density diagnostics indicate higher densities than in the nebular components, reaching values above the critical densities of the atomic levels involved in some diagnostics such as [OII] $\lambda\lambda 3726/\lambda 3729$ or [SII] $\lambda\lambda 6731/\lambda 6716$. We analyzed the density obtained from [FeIII] lines through a maximum-likelihood procedure. We conclude that at values of 10^4 – 10^6 cm^{-3} , the density diagnostics based on [FeIII] lines

are more suitable than the usual ones. Thus, we adopted a density of $n_e = 11880 \pm 1860 \text{ cm}^{-3}$ and $n_e = 44090 \pm 7580 \text{ cm}^{-3}$ for HH529II and HH529III, respectively. We determined the density of each component using the O II RLs from multiplet 1 also through a maximum-likelihood procedure. The good agreement of the results of this diagnostic and the adopted density in the nebular components indicate that the density of the gas emitting RLs do not differ from the one emitting CELs. In the case of HH529II and HH529III, the results based on O II RLs are inconsistent with other diagnostics. This may be a consequence of the weak density-dependence of the O II multiplet 1 for density values above $\sim 10^4 \text{ cm}^{-3}$.

Using CEL ratios, we study 6 T_e -diagnostics. Using the adopted density for each component, we found consistent temperatures between the different diagnostics of the high and low ionization zones. In the nebular components, we derive $T_e(\text{low}) \approx 10000 \pm 200 \text{ K}$ and $T_e(\text{high}) \approx 8500 \pm 150 \text{ K}$ (for each specific cut, see Table 7). In HH529II we obtain $T_e(\text{low}) = 10150^{+570}_{-510} \text{ K}$ and $T_e(\text{high}) = 8270 \pm 110 \text{ K}$. For HH529III, we derive $T_e(\text{low}) = 10020^{+740}_{-650} \text{ K}$ and $T_e(\text{high}) = 8530 \pm 100 \text{ K}$. These results indicate that the temperature does not change between the nebular and the high-velocity components. In the maximum-likelihood procedure followed to derive n_e based on [Fe III] CELs, we have a convergence to a value of T_e consistent with $T_e(\text{high})$, both in the nebular and the high-velocity components. In the nebular components this is due to the low density-sensitivity of the used [Fe III] lines at smaller values than $\sim 10^3 \text{ cm}^{-3}$, biasing the results to the denser areas within the line of sight and then obtaining lower temperatures. In the high-velocity components, denser than 10^4 cm^{-3} , this indicates that the high-ionization gas dominates over the remaining low-ionization one. Using O II RLs we were able to estimate $T_e(\text{O II})$ in the nebular component of cut 2, which has the highest signal to noise. We find that $T_e(\text{O II}) = 9350 \pm 1090$ is in good agreement with $T_e(\text{[O III]})$ within the uncertainties. Since we found that $T_e(\text{O II})$ and $n_e(\text{O II})$ are in good agreement with the physical conditions obtained with CELs in the nebular components, we conclude that the emission of CELs and RLs of O²⁺ comes basically from the same gas. For all components, we derive $T_e(\text{He I})$ while in the “combined cuts” spectra we were able to derive $T_e(\text{H I})$ using both the Balmer and the Paschen Jump. In all the derived physical conditions, we found no significant deviation between the results of the “combined cuts” spectrum and the nebular ones. We conclude that the influence that HH529II and HH529III can exert on the global physical conditions of the Orion Nebula are limited to a small area and its effect is no longer appreciated in the volume of nebular gas integrated in 10 arcsecs.

We derive ionic abundances of O⁺, N⁺, S⁺, Cl⁺, Ni²⁺, O²⁺, Ne²⁺,

ACKNOWLEDGEMENTS

We acknowledge support from the State Research Agency (AEI) of the Spanish Ministry of Science, Innovation and Universities (MCIU) and the European Regional Development Fund (FEDER) under grants AYA2015-65205-P and AYA2017-83383-P. JGR acknowledges support from an Advanced Fellowship from the Severo Ochoa excellence program (SEV-2015-0548). KZA-C acknowledges support from Mexican CONACYT posdoctoral grant 364239. The authors acknowledge support under grant P/308614 financed by funds transferred from the Spanish Ministry of Science, Innovation and Universities, charged to the General State Budgets and

with funds transferred from the General Budgets of the Autonomous Community of the Canary Islands by the MCIU.

REFERENCES

- Arellano-Córdova K. Z., Esteban C., García-Rojas J., Méndez-Delgado J. E., 2020, *MNRAS*, **496**, 1051
 Astropy Collaboration et al., 2013, *A&A*, **558**, A33
 Aver E., Olive K. A., Skillman E. D., 2011, *J. Cosmology Astropart. Phys.*, **2011**, 043
 Baldwin J. A., et al., 1996, *ApJ*, **468**, L115
 Ballester P., Modigliani A., Boitquin O., Cristiani S., Hanuschik R., Kaufer A., Wolf S., 2000, *The Messenger*, **101**, 31
 Bally J., Reipurth B., 2001, *ApJ*, **546**, 299
 Bally J., Reipurth B., 2018, *Research Notes of the American Astronomical Society*, **2**, 46
 Bally J., Sutherland R. S., Devine D., Johnstone D., 1998, *AJ*, **116**, 293
 Bally J., O’Dell C. R., McCaughrean M. J., 2000, *AJ*, **119**, 2919
 Bastin R. J., Storey P. J., 2006, in Barlow M. J., Méndez R. H., eds, IAU Symposium Vol. 234, Planetary Nebulae in our Galaxy and Beyond. pp 369–370, doi:10.1017/S1743921306003280
 Bautista M. A., 2001, *A&A*, **365**, 268
 Benjamin R. A., Skillman E. D., Smits D. P., 2002, *ApJ*, **569**, 288
 Berg D. A., Erb D. K., Henry R. B. C., Skillman E. D., McQuinn K. B. W., 2019, *ApJ*, **874**, 93
 Blagrave K. P. M., Martin P. G., Baldwin J. A., 2006, *ApJ*, **644**, 1006
 Blagrave K. P. M., Martin P. G., Rubin R. H., Dufour R. J., Baldwin J. A., Hester J. J., Walter D. K., 2007, *ApJ*, **655**, 299
 Bohigas J., 2015, *MNRAS*, **453**, 1281
 Bowen I. S., 1955, *ApJ*, **121**, 306
 Brown R. L., Mathews W. G., 1970, *ApJ*, **160**, 939
 Butler K., Zeippen C. J., 1989, *A&A*, **208**, 337
 D’Odorico S., Cristiani S., Dekker H., Hill V., Kaufer A., Kim T., Primas F., 2000, Performance of UVES, the echelle spectrograph for the ESO VLT and highlights of the first observations of stars and quasars. pp 121–130, doi:10.1111/12.390133
 Davey A. R., Storey P. J., Kisielius R., 2000, *A&AS*, **142**, 85
 Delgado-Inglada G., Morisset C., Stasińska G., 2014, *MNRAS*, **440**, 536
 Delgado-Inglada G., Mesa-Delgado A., García-Rojas J., Rodríguez M., Esteban C., 2016, *MNRAS*, **456**, 3855
 Domínguez-Guzmán G., Rodríguez M., Esteban C., García-Rojas J., 2019, arXiv e-prints, p. arXiv:1906.02102
 Dyson J. E., 1984, *Ap&SS*, **106**, 181
 Ellis D. G., Martinson I., 1984, *Phys. Scr.*, **30**, 255
 Espíritu J. N., Peimbert A., Delgado-Inglada G., Ruiz M. T., 2017, *Rev. Mex. Astron. Astrofis.*, **53**, 95
 Esteban C., Peimbert M., 1999, *A&A*, **349**, 276
 Esteban C., Peimbert M., Torres-Peimbert S., Escalante V., 1998, *MNRAS*, **295**, 401
 Esteban C., Peimbert M., García-Rojas J., Ruiz M. T., Peimbert A., Rodríguez M., 2004, *MNRAS*, **355**, 229
 Fang X., Liu X. W., 2011, *MNRAS*, **415**, 181
 Fang X., Liu X. W., 2013, *MNRAS*, **429**, 2791
 Fehrenbach C., 1977, *A&AS*, **29**, 71
 Ferland G. J., 2001, *PASP*, **113**, 41
 Ferland G. J., Henney W. J., O’Dell C. R., Porter R. L., van Hoof P. A. M., Williams R. J. R., 2012, *ApJ*, **757**, 79
 Feuchtgruber H., et al., 1997, *ApJ*, **487**, 962
 Fisher G. H., Welsch B. T., 2008, in Howe R., Komm R. W., Balasubramanian K. S., Petrie G. J. D., eds, Astronomical Society of the Pacific Conference Series Vol. 383, Subsurface and Atmospheric Influences on Solar Activity. p. 373 (arXiv:0712.4289)
 Fritzsche S., Fricke B., Geschke D., Heitmann A., Sienkiewicz J. E., 1999, *ApJ*, **518**, 994
 Froese Fischer C., Tachiev G., 2004, *Atomic Data and Nuclear Data Tables*, **87**, 1
 Froese Fischer C., Rubin R. H., Rodríguez M., 2008, *MNRAS*, **391**, 1828

- Galavis M. E., Mendoza C., Zeippen C. J., 1995, A&AS, **111**, 347
- García-Díaz M. T., Henney W. J., López J. A., Doi T., 2008, Rev. Mex. Astron. Astrofis., **44**, 181
- García-Rojas J., Esteban C., 2007, ApJ, **670**, 457
- García-Rojas J., Esteban C., Peimbert M., Rodríguez M., Ruiz M. T., Peimbert A., 2004, ApJS, **153**, 501
- García-Rojas J., Esteban C., Peimbert A., Peimbert M., Rodríguez M., Ruiz M. T., 2005, MNRAS, **362**, 301
- García-Rojas J., Esteban C., Peimbert A., Rodríguez M., Peimbert M., Ruiz M. T., 2007, Rev. Mex. Astron. Astrofis., **43**, 3
- García-Rojas J., Peña M., Morisset C., Delgado-Ingla G., Mesa-Delgado A., Ruiz M. T., 2013, A&A, **558**, A122
- García-Rojas J., Madonna S., Luridiana V., Sterling N. C., Morisset C., Delgado-Ingla G., Toribio San Cipriano L., 2015, MNRAS, **452**, 2606
- Goudis C., 1982, The Orion complex: A case study of interstellar matter. Vol. 90, doi:10.1007/978-94-009-7712-9,
- Grandi S. A., 1975a, ApJ, **196**, 465
- Grandi S. A., 1975b, ApJ, **199**, L43
- Grieve M. F. R., Ramsbottom C. A., Hudson C. E., Keenan F. P., 2014, ApJ, **780**, 110
- Haro G., 1952, ApJ, **115**, 572
- Haro G., 1953, ApJ, **117**, 73
- Henney W. J., Stasińska G., 2010, ApJ, **711**, 881
- Herbig G. H., 1950, ApJ, **111**, 11
- Herbig G. H., 1951, ApJ, **113**, 697
- Herbig G. H., 1952, J. R. Astron. Soc. Canada, **46**, 222
- Izotov Y. I., Stasińska G., Meynet G., Guseva N. G., Thuan T. X., 2006, A&A, **448**, 955
- Johansson S., Zethson T., Hartman H., Ekberg J. O., Ishibashi K., Davidson K., Gull T., 2000, A&A, **361**, 977
- Jones A. P., Tielens A. G. G. M., Hollenbach D. J., McKee C. F., 1994, ApJ, **433**, 797
- Kaler J. B., 1967, ApJ, **148**, 925
- Kaufman V., Martin W. C., 1993, Journal of Physical and Chemical Reference Data, **22**, 279
- Kaufman V., Sugar J., 1986, Journal of Physical and Chemical Reference Data, **15**, 321
- Kingdon J. B., Ferland G. J., 1995, ApJ, **450**, 691
- Kisielius R., Storey P. J., Davey A. R., Neale L. T., 1998, A&AS, **133**, 257
- Kisielius R., Storey P. J., Ferland G. J., Keenan F. P., 2009, MNRAS, **397**, 903
- Kunth D., Sargent W. L. W., 1983, ApJ, **273**, 81
- Liu X. W., Storey P. J., Barlow M. J., Danziger I. J., Cohen M., Bryce M., 2000, MNRAS, **312**, 585
- Liu X. W., Luo S. G., Barlow M. J., Danziger I. J., Storey P. J., 2001, MNRAS, **327**, 141
- Lodders K., 2019, arXiv e-prints, p. arXiv:1912.00844
- Lucy L. B., 1995, A&A, **294**, 555
- Luridiana V., Morisset C., Shaw R. A., 2015, A&A, **573**, A42
- Masciadri E., Raga A. C., 2001, A&A, **376**, 1073
- McLaughlin B. M., Lee T.-G., Ludlow J. A., Land i E., Loch S. D., Pindzola M. S., Ballance C. P., 2011, Journal of Physics B Atomic Molecular Physics, **44**, 175206
- McNabb I. A., Fang X., Liu X. W., Bastin R. J., Storey P. J., 2013, MNRAS, **428**, 3443
- Méndez-Delgado J. E., Esteban C., García-Rojas J., Arellano-Córdova K. Z., Valerdi M., 2020, MNRAS, **496**, 2726
- Mendoza C., 1983, in Aller L. H., ed., IAU Symposium Vol. 103, Planetary Nebulae. pp 143–172
- Mendoza C., Zeippen C. J., 1982a, MNRAS, **198**, 127
- Mendoza C., Zeippen C. J., 1982b, MNRAS, **199**, 1025
- Mendoza C., Zeippen C. J., 1983, MNRAS, **202**, 981
- Mesa-Delgado A., Esteban C., García-Rojas J., 2008, ApJ, **675**, 389
- Mesa-Delgado A., Esteban C., García-Rojas J., Luridiana V., Bautista M., Rodríguez M., López-Martín L., Peimbert M., 2009, MNRAS, **395**, 855
- Moehler S., Dreizler S., LeBlanc F., Khalack V., Michaud G., Richer J., Sweigart A. V., Grundahl F., 2014a, A&A, **565**, A100
- Moehler S., et al., 2014b, A&A, **568**, A9
- Mouri H., Taniguchi Y., 2000, ApJ, **534**, L63
- Nicholls D. C., Dopita M. A., Sutherland R. S., 2012, ApJ, **752**, 148
- O'Dell C. R., 2001, ARA&A, **39**, 99
- O'Dell C. R., 2018, MNRAS, **478**, 1017
- O'Dell C. R., Henney W. J., 2008, AJ, **136**, 1566
- O'Dell C. R., Wen Z., 1992, ApJ, **387**, 229
- O'Dell C. R., Ferland G. J., Henney W. J., Peimbert M., García-Díaz M. T., Rubin R. H., 2015, AJ, **150**, 108
- O'Dell C. R., Abel N. P., Ferland G. J., 2020, ApJ, **891**, 46
- Olive K. A., Skillman E. D., 2004, ApJ, **617**, 29
- Osterbrock D. E., Ferland G. J., 2006, Astrophysics of gaseous nebulae and active galactic nuclei
- Osterbrock D. E., Tran H. D., Veilleux S., 1992, ApJ, **389**, 305
- Pagel B. E. J., Simonson E. A., Terlevich R. J., Edmunds M. G., 1992, MNRAS, **255**, 325
- Peimbert M., 1967, ApJ, **150**, 825
- Peimbert A., 2003, ApJ, **584**, 735
- Peimbert M., Costero R., 1969, Boletín de los Observatorios Tonantzintla y Tacubaya, **5**, 3
- Peimbert A., Peimbert M., 2013, ApJ, **778**, 89
- Peimbert A., Peimbert M., Luridiana V., 2002, ApJ, **565**, 668
- Pequignot D., Petitjean P., Boisson C., 1991, A&A, **251**, 680
- Pequignot D., Amara M., Liu X. W., Barlow M. J., Storey P. J., Morisset C., Torres-Peimbert S., Peimbert M., 2002, in Henney W. J., Franco J., Martos M., eds, Revista Mexicana de Astronomía y Astrofísica Conference Series Vol. 12, Revista Mexicana de Astronomía y Astrofísica Conference Series. pp 142–143
- Persson W., Wahlström C.-G., Jönsson L., Di Rocco H. O., 1991, Phys. Rev. A, **43**, 4791
- Podobedova L. I., Kelleher D. E., Wiese W. L., 2009, Journal of Physical and Chemical Reference Data, **38**, 171
- Porter R. L., Ferland G. J., MacAdam K. B., 2007, ApJ, **657**, 327
- Porter R. L., Ferland G. J., Storey P. J., Detisch M. J., 2012, MNRAS, **425**, L28
- Porter R. L., Ferland G. J., Storey P. J., Detisch M. J., 2013, MNRAS, **433**, L89
- Price-Whelan A. M., et al., 2018, AJ, **156**, 123
- Quinet P., 1996, A&AS, **116**, 573
- Raga A. C., Reipurth B., 2004, Rev. Mex. Astron. Astrofis., **40**, 15
- Raga A. C., López-Martín J., López J. A., Meaburn J., 2000a, in Arthur S. J., Brickhouse N. S., Franco J., eds, Revista Mexicana de Astronomía y Astrofísica Conference Series Vol. 9, Revista Mexicana de Astronomía y Astrofísica Conference Series. pp 191–193
- Raga A., et al., 2000b, MNRAS, **314**, 681
- Ramsbottom C. A., Bell K. L., 1997, Atomic Data and Nuclear Data Tables, **66**, 65
- Reipurth B., Bally J., 2001, ARA&A, **39**, 403
- Roberto M., et al., 2005, AJ, **129**, 1534
- Roberto M., et al., 2013, ApJS, **207**, 10
- Rodríguez M., 1999, A&A, **348**, 222
- Rodríguez M., 2002, A&A, **389**, 556
- Rodríguez M., 2020, MNRAS, **495**, 1016
- Rodríguez M., Rubin R. H., 2005, ApJ, **626**, 900
- Schwartz R. D., 1983, ARA&A, **21**, 209
- Simón-Díaz S., Stasińska G., 2011, A&A, **526**, A48
- Smith N., Bally J., Shuping R. Y., Morris M., Kassis M., 2005, AJ, **130**, 1763
- Stasińska G., 1978, A&A, **66**, 257
- Stasińska G., Tenorio-Tagle G., Rodríguez M., Henney W. J., 2007, A&A, **471**, 193
- Storey P. J., 1994, A&A, **282**, 999
- Storey P. J., Hummer D. G., 1995, MNRAS, **272**, 41
- Storey P. J., Zeippen C. J., 2000, MNRAS, **312**, 813
- Storey P. J., Sochi T., Badnell N. R., 2014, MNRAS, **441**, 3028
- Storey P. J., Sochi T., Bastin R., 2017, MNRAS, **470**, 379
- Tayal S. S., 2004, A&A, **418**, 363
- Tayal S. S., 2011, ApJS, **195**, 12

- Tayal S. S., Zatsarinny O., 2010, *ApJS*, **188**, 32
 Tody D., 1993, IRAF in the Nineties. p. 173
 Torres-Peimbert S., Peimbert M., Daltabuit E., 1980, *ApJ*, **238**, 133
 Tsamis Y. G., Walsh J. R., Vílchez J. M., Péquignot D., 2011, *MNRAS*, **412**, 1367
 Van Hoof P. A. M., 2018, *Galaxies*, 6
 Verner E. M., Verner D. A., Baldwin J. A., Ferland G. J., Martin P. G., 2000, *ApJ*, **543**, 831
 Vilchez J. M., Pagel B. E. J., 1988, *MNRAS*, **231**, 257
 Walter D. K., Dufour R. J., Hester J. J., 1992, *ApJ*, **397**, 196
 Welsch B. T., Fisher G. H., Abbott W. P., Regnier S., 2004, *ApJ*, **610**, 1148
 Wesson R., Jones D., García-Rojas J., Boffin H. M. J., Corradi R. L. M., 2018, *MNRAS*, **480**, 4589
 Wiese W. L., Fuhr J. R., Deters T. M., 1996, Journal of Physical and Chemical Reference Data, Monograph 7, **403**
 Yuan H. B., Liu X. W., Péquignot D., Rubin R. H., Ercolano B., Zhang Y., 2011, *MNRAS*, **411**, 1035
 Zhang Y., Liu X. W., 2006, in Barlow M. J., Méndez R. H., eds, IAU Symposium Vol. 234, Planetary Nebulae in our Galaxy and Beyond. pp 547–548 ([arXiv:astro-ph/0605180](https://arxiv.org/abs/astro-ph/0605180)), doi:10.1017/S1743921306004170
 Zhang H. L., Pradhan A. K., 1997, *A&AS*, **126**, 373
 Zhang, Hong Lin 1996, *Astron. Astrophys. Suppl. Ser.*, **119**, 523
 Zhang Y., Liu X. W., Liu Y., Rubin R. H., 2005, *MNRAS*, **358**, 457

Table A1. Slope and intercept for Eq. 4 for a range of densities.

n_e (cm $^{-3}$)	α	β
100	92984	-7455
500	81830	-6031
1000	77896	-5527
2000	69126	-4378
3000	65040	-3851
4000	62517	-3529
5000	60744	-3305
6000	59402	-3137
7000	58334	-3004
8000	57456	-2895
9000	56715	-2804
10000	56077	-2726
12000	55637	-2676
15000	55087	-2611
20000	54364	-2523
25000	53796	-2452
30000	53329	-2392
40000	52591	-2297
45000	52289	-2257
50000	52019	-2222

APPENDIX A: SOME EXTRA MATERIAL

J: In this appendix we show some of the Tables and Figures of the paper. Bla bla bla

This paper has been typeset from a $\text{\TeX}/\text{\LaTeX}$ file prepared by the author.

Table A2. Fe²⁺ abundances based on T_e (low).

λ	Cut 1		Cut 2		Cut 3		Cut 4		Combined cuts
	Nebula	HH529II	Nebula	HH529III	Nebula	Nebula	Nebula	Nebula	
4658	5.51 ± 0.02	5.59 ^{+0.08} _{-0.06}	5.56 ^{+0.04} _{-0.03}	5.49 ^{+0.11} _{-0.08}	5.51 ± 0.04	5.47 ^{+0.05} _{-0.04}	5.52 ± 0.03	5.52 ± 0.03	
4702	5.51 ± 0.02	5.59 ^{+0.08} _{-0.06}	5.56 ^{+0.04} _{-0.03}	5.50 ^{+0.12} _{-0.08}	5.52 ± 0.04	5.47 ^{+0.05} _{-0.04}	5.52 ^{+0.04} _{-0.03}	5.52 ± 0.04	
4734	5.48 ± 0.03	5.58 ^{+0.09} _{-0.07}	5.56 ± 0.04	5.61 ^{+0.13} _{-0.09}	5.50 ^{+0.05} _{-0.04}	5.47 ^{+0.05} _{-0.04}	5.52 ± 0.04	5.52 ± 0.04	
4755	5.51 ^{+0.03} _{-0.02}	5.61 ^{+0.09} _{-0.07}	5.58 ^{+0.04} _{-0.03}	5.56 ^{+0.12} _{-0.09}	5.52 ^{+0.05} _{-0.04}	5.49 ^{+0.05} _{-0.04}	5.54 ^{+0.04} _{-0.03}	5.54 ± 0.04	
4770	5.51 ± 0.03	5.63 ^{+0.09} _{-0.07}	5.59 ± 0.04	5.62 ^{+0.12} _{-0.09}	5.55 ^{+0.05} _{-0.04}	5.48 ^{+0.05} _{-0.04}	5.56 ^{+0.04} _{-0.03}	5.56 ± 0.04	
4778	5.51 ± 0.04	5.75 ^{+0.09} _{-0.07}	5.59 ± 0.04	5.46 ^{+0.16} _{-0.11}	5.51 ^{+0.05} _{-0.04}	5.42 ^{+0.06} _{-0.05}	5.55 ± 0.04	5.55 ± 0.04	
4881	5.53 ± 0.02	5.61 ^{+0.09} _{-0.06}	5.58 ^{+0.04} _{-0.03}	5.55 ^{+0.12} _{-0.09}	5.53 ± 0.04	5.49 ^{+0.05} _{-0.04}	5.54 ± 0.03	5.54 ± 0.03	
5011	5.52 ± 0.04	5.78 ^{+0.08} _{-0.07}	5.56 ± 0.04	5.66 ^{+0.12} _{-0.09}	5.51 ^{+0.05} _{-0.04}	5.51 ^{+0.06} _{-0.05}	5.57 ± 0.04	5.57 ± 0.04	
5271	5.55 ± 0.02	5.61 ^{+0.08} _{-0.06}	5.58 ^{+0.04} _{-0.03}	5.53 ^{+0.11} _{-0.08}	5.55 ± 0.04	5.52 ± 0.04	5.55 ± 0.03	5.55 ± 0.03	
5412	5.57 ^{+0.06} _{-0.05}	5.68 ^{+0.10} _{-0.08}	5.60 ^{+0.05} _{-0.04}	-	5.57 ^{+0.05} _{-0.04}	5.58 ^{+0.07} _{-0.06}	5.56 ± 0.05	5.56 ± 0.05	
8838	5.37 ^{+0.11} _{-0.10}	5.41 ^{+0.19} _{-0.15}	5.48 ^{+0.08} _{-0.07}	-	5.34 ^{+0.09} _{-0.08}	5.47 ^{+0.11} _{-0.09}	5.34 ^{+0.09} _{-0.08}	5.34 ^{+0.09} _{-0.08}	
Weighted Average	5.52 ± 0.03	5.62 ± 0.07	5.57 ± 0.02	5.54 ± 0.06	5.52 ± 0.04	5.48 ± 0.03	5.53 ± 0.04		

Table A3. Fe²⁺ abundances based on T_e (high).

λ	Cut 1		Cut 2		Cut 3		Cut 4		Combined cuts
	Nebula	HH529II	Nebula	HH529III	Nebula	Nebula	Nebula	Nebula	
4658	5.77 ^{+0.05} _{-0.04}	5.92 ^{+0.03} _{-0.02}	5.81 ± 0.03	5.75 ± 0.02	5.78 ± 0.03	5.75 ± 0.03	5.79 ± 0.03	5.79 ± 0.03	
4702	5.76 ^{+0.05} _{-0.04}	5.92 ± 0.03	5.80 ± 0.03	5.75 ^{+0.04} _{-0.03}	5.78 ± 0.03	5.74 ± 0.03	5.79 ^{+0.04} _{-0.03}	5.79 ± 0.04	
4734	5.74 ^{+0.05} _{-0.04}	5.91 ^{+0.04} _{-0.03}	5.81 ^{+0.04} _{-0.03}	5.87 ^{+0.06} _{-0.05}	5.77 ^{+0.04} _{-0.03}	5.75 ^{+0.04} _{-0.03}	5.79 ± 0.04	5.79 ± 0.04	
4755	5.76 ^{+0.05} _{-0.04}	5.94 ± 0.03	5.83 ± 0.03	5.82 ± 0.05	5.79 ± 0.03	5.76 ± 0.03	5.81 ± 0.03	5.81 ± 0.03	
4770	5.76 ^{+0.05} _{-0.04}	5.96 ± 0.03	5.84 ± 0.03	5.87 ± 0.05	5.81 ^{+0.04} _{-0.03}	5.75 ^{+0.04} _{-0.03}	5.82 ^{+0.04} _{-0.03}	5.82 ± 0.04	
4778	5.76 ^{+0.06} _{-0.05}	6.08 ± 0.04	5.84 ^{+0.04} _{-0.03}	5.72 ± 0.09	5.78 ^{+0.04} _{-0.03}	5.70 ^{+0.05} _{-0.04}	5.82 ± 0.04	5.82 ± 0.04	
4881	5.79 ± 0.04	5.94 ± 0.03	5.83 ± 0.03	5.80 ± 0.04	5.79 ± 0.03	5.76 ± 0.03	5.80 ± 0.03	5.80 ± 0.03	
5011	5.76 ^{+0.06} _{-0.05}	6.09 ± 0.04	5.79 ± 0.03	5.90 ^{+0.07} _{-0.06}	5.76 ± 0.03	5.77 ^{+0.05} _{-0.04}	5.82 ± 0.04	5.82 ± 0.04	
5271	5.77 ± 0.04	5.91 ± 0.03	5.81 ± 0.03	5.76 ^{+0.04} _{-0.03}	5.79 ± 0.03	5.77 ± 0.03	5.79 ± 0.03	5.79 ± 0.03	
5412	5.80 ^{+0.07} _{-0.06}	5.97 ^{+0.07} _{-0.06}	5.83 ± 0.04	-	5.81 ± 0.04	5.83 ± 0.06	5.80 ± 0.05	5.80 ± 0.05	
8838	5.73 ^{+0.12} _{-0.11}	5.87 ± 0.13	5.83 ^{+0.07} _{-0.06}	-	5.72 ^{+0.08} _{-0.07}	5.86 ± 0.09	5.72 ^{+0.09} _{-0.08}	5.72 ± 0.09	
Weighted Average	5.77 ± 0.02	5.94 ± 0.05	5.82 ± 0.02	5.78 ± 0.05	5.78 ± 0.02	5.76 ± 0.03	5.80 ± 0.02		

Table A4. Cl²⁺ and Cl abundances and Cl/O ratio using T_e (low), T_e ([S III]) and T_e (high).

Cut	Component	O ²⁺ /O	Cl ²⁺ /H ⁺	T_e (low)		T_e ([S III])		T_e (high)			
				Cl/H	Cl/O	Cl/H	Cl/O	Cl/H	Cl/O		
1	Nebular	0.73 ± 0.04	4.78 ± 0.02	4.83 ± 0.02	-3.63 ± 0.03	4.88 ^{+0.06} _{-0.05}	4.92 ± 0.06	-3.53 ± 0.07	5.01 ± 0.03	5.04 ± 0.03	-3.42 ± 0.05
2	HH529II	0.94 ± 0.04	4.80 ^{+0.08} _{-0.06}	4.83 ± 0.07	-3.74 ± 0.07	5.01 ^{+0.05} _{-0.05}	5.03 ± 0.05	-3.54 ± 0.05	5.08 ± 0.03	5.10 ± 0.03	-3.47 ± 0.04
2	Nebular	0.77 ± 0.05	4.81 ^{+0.04} _{-0.03}	4.86 ± 0.04	-3.61 ± 0.06	4.93 ^{+0.06} _{-0.05}	4.97 ± 0.06	-3.49 ± 0.07	5.03 ± 0.03	5.06 ± 0.03	-3.41 ± 0.05
3	HH529III	0.83 ± 0.05	4.94 ^{+0.10} _{-0.08}	4.96 ± 0.08	-3.63 ± 0.09	5.09 ^{+0.06} _{-0.06}	5.11 ± 0.06	-3.48 ± 0.07	5.16 ± 0.04	5.17 ± 0.04	-3.42 ± 0.05
3	Low velocity shock+nebula	0.79 ± 0.05	4.80 ^{+0.04} _{-0.03}	4.85 ± 0.04	-3.60 ± 0.06	4.96 ^{+0.06} _{-0.05}	4.99 ± 0.06	-3.46 ± 0.07	5.03 ^{+0.03} _{-0.02}	5.06 ± 0.03	-3.39 ± 0.05
4	Nebular	0.78 ± 0.05	4.79 ± 0.04	4.85 ± 0.04	-3.62 ± 0.06	4.95 ^{+0.05} _{-0.05}	4.99 ± 0.06	-3.48 ± 0.07	5.03 ± 0.03	5.06 ± 0.03	-3.41 ± 0.05
-	Combined cuts	0.81 ± 0.05	4.79 ± 0.03	4.84 ± 0.03	-3.62 ± 0.05	4.94 ^{+0.05} _{-0.04}	4.97 ± 0.05	-3.50 ± 0.06	5.02 ± 0.03	5.05 ± 0.03	-3.41 ± 0.05

Table A5. Ni²⁺ abundances per line.

λ	Cut 1		Cut 2		Cut 3		Cut 4		Combined cuts
	Nebula	HH529II	Nebula	HH529III	Nebula	Nebula	Nebula	Nebula	
6000	4.52 ± 0.08	4.42 ^{+0.13} _{-0.11}	4.34 ^{+0.07} _{-0.06}	-	4.40 ± 0.07	4.42 ^{+0.10} _{-0.09}	4.35 ± 0.08		
6534	4.22 ^{+0.10} _{-0.11}	4.61:	4.19 ± 0.06	4.44:	4.16 ± 0.07	4.18 ± 0.11	4.26 ± 0.07		
6682	4.76 ^{+0.14} _{-0.13}	-	4.70 ^{+0.14} _{-0.13}	-	4.44 ^{+0.14} _{-0.13}	-	-		
6797	4.50 ^{+0.23} _{-0.22}	4.94:	4.79 ± 0.08	-	4.77 ± 0.10	4.81:	4.77 ± 0.14		
6946	3.94 ^{+0.26} _{-0.23}	4.75 ^{+0.19} _{-0.17}	4.23 ± 0.11	4.50:	4.21 ± 0.11	4.23 ^{+0.15} _{-0.14}	4.31:		
7890	4.42 ± 0.04	4.52 ^{+0.08} _{-0.06}	4.49 ± 0.04	4.39 ^{+0.12} _{-0.10}	4.45 ^{+0.05} _{-0.04}	4.45 ^{+0.05} _{-0.04}	4.46 ± 0.04		
Weighted Average	4.37 ± 0.14	4.50 ± 0.08	4.33 ± 0.17	4.39^{+0.12}_{-0.10}	4.32 ± 0.16	4.36 ± 0.12	4.38 ± 0.10		

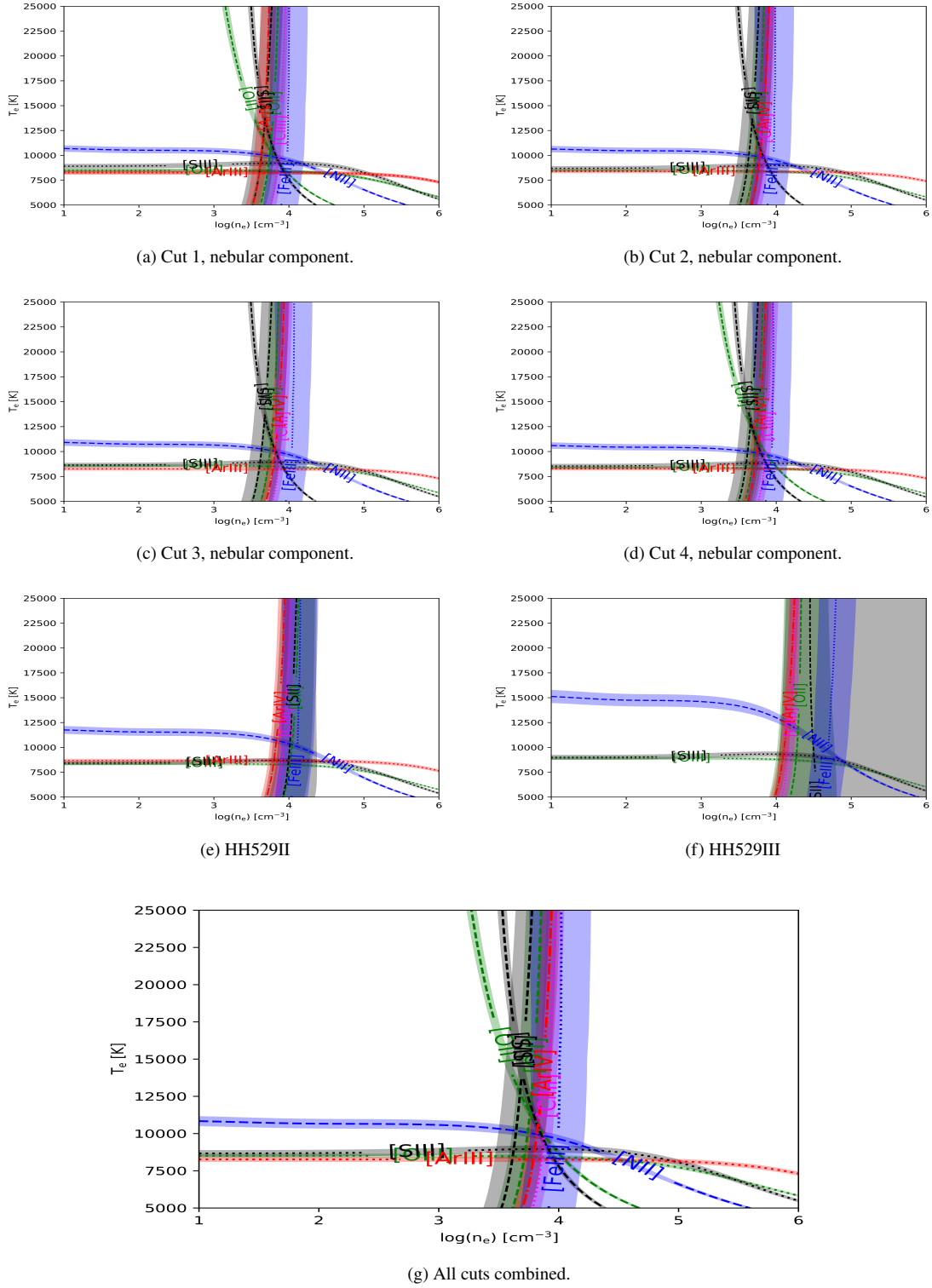


Figure A1. Plasma diagnostic plots for each of the 7 components analyzed in this work. The labeled diagnostics correspond to those discussed in § 4.1, whose results are presented in Table 7.

Table A6. Values of t^2 estimated for each component, based on the combination of Eq.(12) with Eq.(13), Eq.(14) and Eq.(15).

Cut	Component	$t^2(\text{O}^{2+})$	$t^2(\text{S}^{2+})$	$t^2(\text{N}^+)$
1	Nebular	0.004 ± 0.012	0.040 ± 0.026	0.053 ± 0.018
2	HH529II	0.025 ± 0.013	0.062 ± 0.026	0.095 ± 0.024
2	Nebular	0.008 ± 0.012	0.039 ± 0.025	0.058 ± 0.018
3	HH529III	0.027 ± 0.017	0.068 ± 0.033	0.087 ± 0.033
3	Low velocity shock+nebula	0.010 ± 0.013	0.036 ± 0.026	0.064 ± 0.019
4	Nebular	0.022 ± 0.014	0.062 ± 0.027	0.079 ± 0.020

Table A7. Average velocities and FWHM for the observed ions for selected cuts and components.

Ion	I.P. (eV)	Nebular Cut 2		HH529II		HH529III	
		$\langle V \rangle$ (Km s $^{-1}$)	$\langle \text{FWHM} \rangle$ (Km s $^{-1}$)	$\langle V \rangle$ (Km s $^{-1}$)	$\langle \text{FWHM} \rangle$ (Km s $^{-1}$)	$\langle V \rangle$ (Km s $^{-1}$)	$\langle \text{FWHM} \rangle$ (Km s $^{-1}$)
[O I]	0.00	28.80 ± 0.03 (2)	11.80 ± 0.02 (2)	-	-	-	-
[C I]	0.00	28.70 ± 0.03 (3)	9.49 ± 0.10 (3)	-	-	-	-
[N I]	0.00	30.25 ± 0.64 (3)	9.51 ± 0.60 (3)	-	-	-	-
[Cr II]	6.77	28.28 ± 2.66 (5)	9.71 ± 1.19 (5)	-26.50 ± 1.00 (1)	25.60 ± 1.00 (1)	-27.20 ± 1.00 (1)	39.40 ± 1.00 (1)
[Ni II]	7.64	30.20 ± 0.08 (10)	11.75 ± 0.63 (10)	-30.20 ± 6.09 (3)	15.81 ± 2.83 (3)	-	-
[Fe II]	7.90	27.33 ± 1.36 (34)	11.84 ± 2.29 (34)	-28.76 ± 1.21 (2)	13.66 ± 0.97 (2)	-	-
[S II]	10.36	23.10 ± 0.86 (4)	21.52 ± 0.90 (4)	-27.80 ± 0.03 (4)	16.29 ± 0.45 (4)	-21.94 ± 1.46 (6)	22.92 ± 1.00 (6)
[Cl III]	12.97	24.80 ± 1.00 (1)	20.40 ± 1.00 (1)	-23.80 ± 1.00 (1)	18.90 ± 1.00 (1)	-	-
H I	13.60	16.39 ± 0.78 (51)	24.95 ± 0.16 (51)	-29.08 ± 0.36 (51)	27.20 ± 0.01 (51)	-23.90 ± 0.89 (45)	33.12 ± 0.44 (45)
[O II]	13.62	17.85 ± 1.65 (2)	18.69 ± 0.69 (2)	-28.40 ± 1.20 (2)	20.04 ± 1.10 (2)	-21.60 ± 0.03 (2)	25.27 ± 0.53 (2)
O I	13.62	18.73 ± 0.50 (3)	23.29 ± 0.86 (3)	-	-	-	-
[N II]	14.53	20.67 ± 0.95 (4)	19.45 ± 0.05 (4)	-28.70 ± 0.80 (4)	18.13 ± 0.45 (4)	-19.75 ± 1.05 (3)	25.98 ± 0.19 (3)
[Fe III]	16.19	13.83 ± 1.09 (21)	12.10 ± 0.32 (21)	-31.90 ± 0.02 (17)	13.56 ± 0.34 (17)	-26.43 ± 1.07 (13)	25.11 ± 2.47 (13)
[Cr III]	16.49	12.40 ± 2.02 (4)	16.98 ± 4.86 (4)	-34.54 ± 1.56 (3)	20.24 ± 1.56 (3)	-23.60 ± 1.00 (1)	10.80 ± 1.00 (1)
[Ni III]	18.17	20.28 ± 0.15 (2)	15.36 ± 0.87 (2)	-24.54 ± 0.24 (2)	12.80 ± 1.57 (2)	-19.20 ± 1.00 (1)	25.70 ± 1.00 (1)
[S III]	23.34	15.00 ± 1.00 (1)	12.70 ± 1.00 (1)	-30.60 ± 1.00 (1)	15.10 ± 1.00 (1)	-25.90 ± 1.00 (1)	25.10 ± 1.00 (1)
[Cl III]	23.81	14.20 ± 0.30 (4)	12.44 ± 0.29 (4)	-30.98 ± 1.91 (3)	16.16 ± 1.06 (3)	-27.24 ± 0.08 (2)	25.81 ± 1.08 (2)
C II	24.38	18.63 ± 1.95 (6)	13.71 ± 0.69 (6)	-26.00 ± 2.18 (5)	21.61 ± 1.82 (5)	-23.39 ± 1.93 (2)	46.05 ± 4.30 (2)
He I	24.59	15.87 ± 0.53 (75)	15.81 ± 0.33 (75)	-29.08 ± 0.90 (66)	21.52 ± 1.23 (66)	-24.42 ± 0.60 (42)	26.51 ± 0.63 (42)
[Ar III]	27.63	15.40 ± 0.04 (2)	11.10 ± 0.04 (2)	-30.40 ± 0.04 (2)	16.10 ± 0.04 (2)	-25.00 ± 1.00 (1)	25.10 ± 1.00 (1)
[Fe IV]	30.65	21.20 ± 1.00 (1)	12.30 ± 1.00 (1)	-23.70 ± 1.00 (1)	19.40 ± 1.00 (1)	-	-
[Cr IV]	30.96	18.40 ± 1.00 (1)	12.10 ± 1.00 (1)	-25.70 ± 1.00 (1)	21.90 ± 1.00 (1)	-30.20 ± 1.00 (1)	39.40 ± 1.00 (1)
[O III]	35.12	16.13 ± 1.37 (3)	11.75 ± 0.45 (3)	-29.07 ± 1.03 (3)	17.60 ± 0.01 (3)	-25.03 ± 0.42 (3)	25.02 ± 0.70 (3)
O II	35.12	15.80 ± 0.03 (6)	12.64 ± 0.44 (6)	-29.38 ± 0.12 (6)	18.89 ± 0.43 (6)	-25.23 ± 0.68 (6)	31.78 ± 3.46 (6)
[Cl IV]	39.61	17.80 ± 1.00 (1)	10.50 ± 1.00 (1)	-27.60 ± 1.00 (1)	21.90 ± 1.00 (1)	-20.50 ± 1.00 (1)	33.10 ± 1.00 (1)
[Ar IV]	40.74	15.35 ± 1.55 (2)	11.69 ± 0.69 (2)	-29.45 ± 2.65 (2)	21.20 ± 2.20 (2)	-26.83 ± 0.07 (2)	27.88 ± 2.92 (2)
[Ne III]	40.96	15.80 ± 0.10 (2)	12.35 ± 0.05 (2)	-28.95 ± 0.05 (2)	16.22 ± 0.04 (2)	-25.90 ± 0.03 (2)	25.50 ± 0.03 (2)
Ne II	40.96	14.92 ± 0.33 (2)	14.44 ± 1.49 (2)	-26.89 ± 0.37 (2)	22.28 ± 0.14 (2)	-	-
N I	14.53	29.82 ± 0.25 (16)	9.47 ± 0.20 (16)	-29.80 ± 1.00 (1)	36.00 ± 1.00 (1)	-25.40 ± 1.00 (1)	29.40 ± 1.00 (1)
Si II	16.35	19.25 ± 2.45 (10)	19.42 ± 1.35 (10)	-29.18 ± 1.06 (8)	17.35 ± 1.78 (8)	-26.90 ± 1.16 (7)	23.89 ± 2.25 (7)
Si III	33.49	12.91 ± 1.00 (1)	13.23 ± 2.79 (1)	-31.80 ± 1.00 (1)	10.80 ± 1.00 (1)	-	-
Ne I	21.57	16.66 ± 2.38 (6)	15.66 ± 0.65 (6)	-31.78 ± 5.50 (3)	23.81 ± 2.20 (3)	-	-
S II	23.34	16.50 ± 0.69 (5)	16.69 ± 4.21 (5)	-26.88 ± 0.44 (3)	25.49 ± 3.34 (3)	-34.90 ± 1.00 (1)	33.10 ± 1.00 (1)
N II	29.60	15.07 ± 2.57 (25)	13.65 ± 1.94 (25)	-29.93 ± 1.10 (10)	18.33 ± 2.29 (10)	-25.31 ± 3.86 (7)	24.49 ± 7.94 (7)
S III	34.79	16.06 ± 0.80 (4)	13.83 ± 2.61 (4)	-29.04 ± 1.87 (4)	25.21 ± 3.48 (4)	-38.86 ± 4.34 (3)	15.85 ± 4.12 (3)
N III	47.45	11.52 ± 0.81 (2)	11.94 ± 0.16 (2)	-36.50 ± 1.00 (1)	22.70 ± 1.00 (1)	-	-

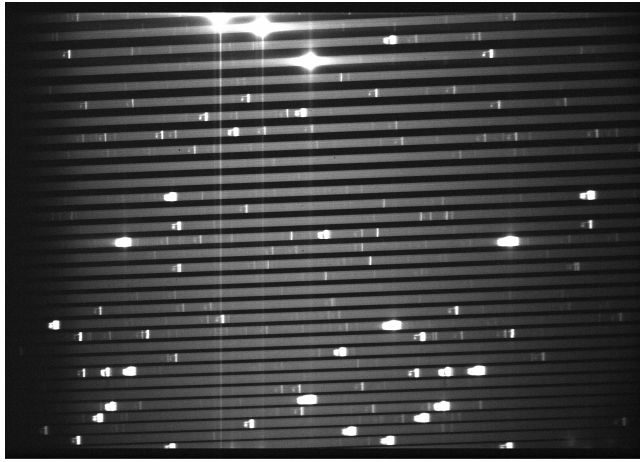


Figure A2. Image of part of the echelle orders extracted in the UVES blue arm using dichroic #2 setting ($\Delta\lambda = 3750\text{--}4995 \text{\AA}$). The contrast highlights reflections in the optical system of the spectrograph that can affect some lines. We have established that order 1 is the order at the bottom and 31 at the top.

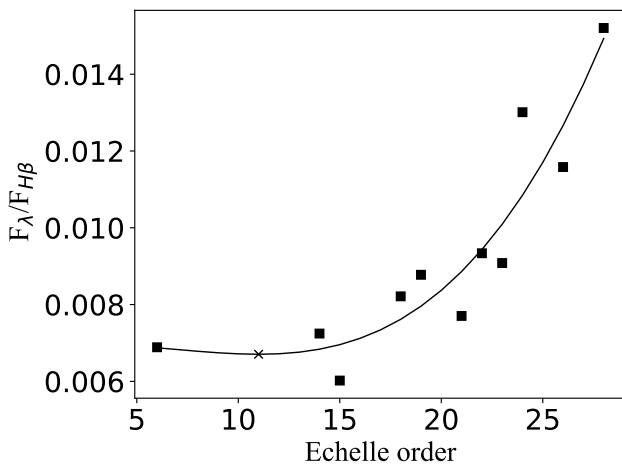


Figure A3. Least Squares fit of the flux emission for the third source of “ghost lines” in the echelle orders. The prediction for the ghost line at $\lambda = 4089.07$ (in the order 11) is marked with a cross.

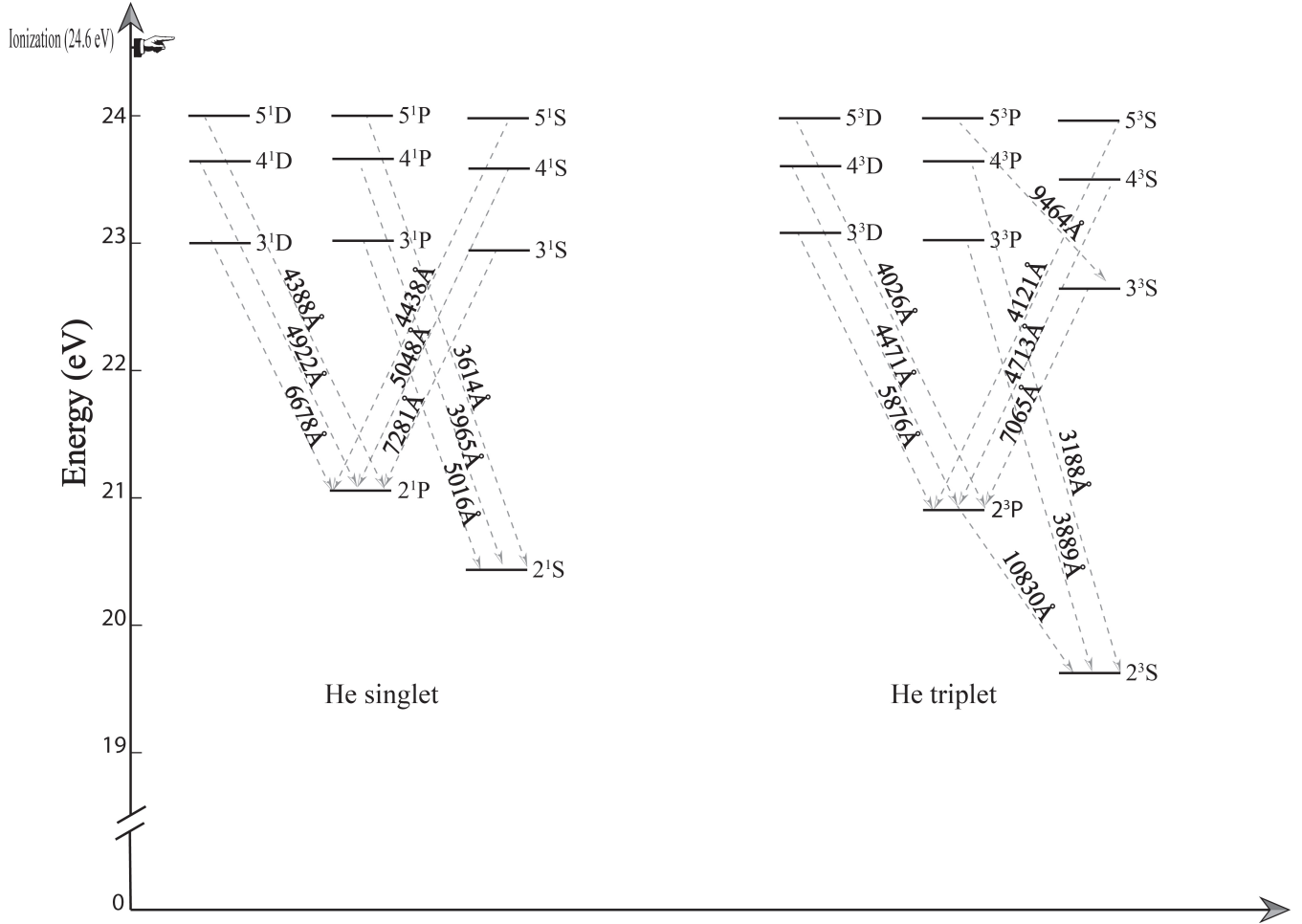
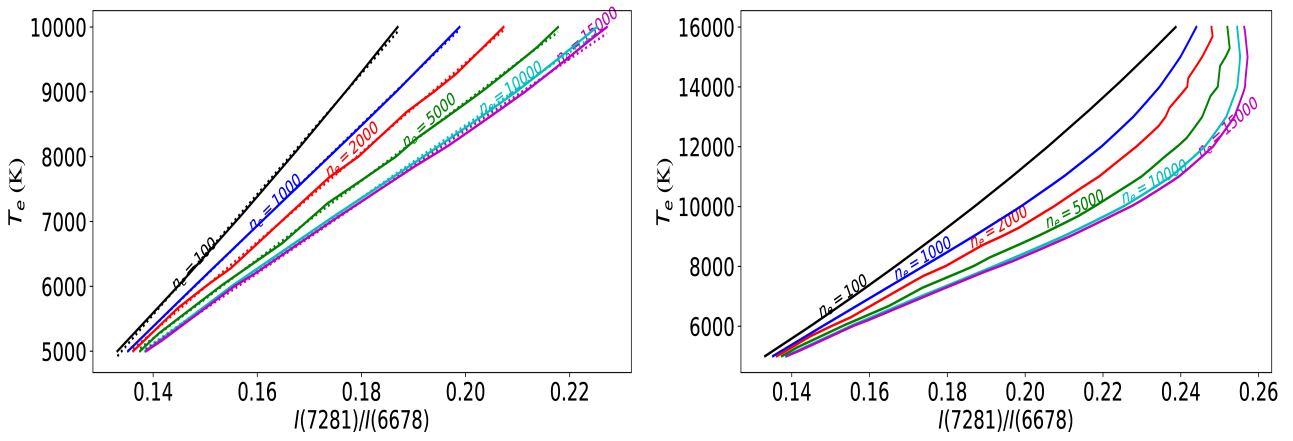


Figure A4. Grotrian diagram of He I for both configurations: triplet and singlet.



(a) A linear fit is accurate for $T_e \leq 10000$ K.

(b) A linear fit is not accurate for $T_e > 10000$ K.

Figure A5. Dependence of $I(\text{He I } \lambda 7281)/I(\text{He I } \lambda 6678)$ on the physical conditions.